European GDR

Centre National
de la Recherche
Scientifique

European Research Network

Ninth meeting

Wave propagation in complex media
for quantitative and Non-Destructive Evaluation

Aussois, Savoie, France

7th to 11th December 2015

EPSRC
Engineering and Physical Sciences
Research Council

RCNDE
**UK Research Centre in
Nondestructive Evaluation**

Ninth Meeting of the GDR in Aussois

December 7th to 11th 2015

" Wave Propagation in complex media for quantitative and non destructive evaluation "

Abstracts

Clark M., *Keynote lecture : Imaging with sub-optical wavelength ultrasound*.

Colombi A., Colquitt D., Roux P., Craster R. and Guenneau S., *Analysis of a locally resonant metamaterial for flexural waves in plates and Rayleigh waves in solids*..

Baronian V., Bonnet-Ben Dhia A.S., Fliss S. and Tonnoir A., *Coupling plane wave representations and finite elements for the simulation of time-harmonic scattering in anisotropic media*.

Chapman J., A class of reduced-order models for elastic waves in a layer .

Treyssède F., *Veering of dispersion curves and prestress effects in multi-wire helical waveguides*.

Darmon M., Dorval V., Kamta Djakou A., Fradkin L. and Chatillon S., *A generic GTD-Kirchhoff scattering model for ultrasonic NDTof planar defects* .

Er-Raoudi M., Diany M. and Mabrouki M., *Bearings defects prediction using Empirical Wavelet Transform*.

Kergomard J., *Keynote lecture : Junctions of acoustic waveguides with rigid walls at low frequencies; application to periodic media*.

Chouiyakh H., **Azrar L., Alnefaie K. and Akourri O. ,** *Huang Hilbert Transform based procedure for multi-crack identification of beams under a moving excitation*.

Shi F., Lowe M., Skelton E. and Craster R., *Analytical solution for the diffuse scattered field of elastic waves at randomly rough surfaces*.

Tant K. and Mulholland A., *Objective defect characterisation using ultrasonic phased array data* .

Al-Lashi R.S. and Challis R., *Ultrasonic particle sizing in non-dilute suspensions* .

Haslinger S., Craster R., Movchan A., Movchan N. and Jones I., *Interfacial waves and neutrality for semi-infinite platonic crystals*.

Lan B., Lowe M. and Dunne F.P.E., Texture determination from ultrasonic wave speeds for HCP and cubic materials .

Real G., Habault D., Cristol X., Fattacioli D. and Sessarego J.P., *An ultrasonic test bench for reproducing oceanic sound fluctuations*.

Baronian V., Bonnet-Ben Dhia A.S., Fliss S. and Tonnoir A., *Domain Decomposition Method for scattering problem in 3D elastic waveguides* .

Lopez Villaverde E., Robert S. and Prada C., *Noise reduction in ultrasonic array imaging by the DORT method*.

Saidoun A., Meziane A., Renier M., Bacon C., Fan Z. and Walaszek H., *Experimental and numerical studies of the nonlinear interaction between a longitudinal wave and contact interface*.

Mulholland A., *Keynote lecture : Mathematical Modelling in the Centre for Ultrasonic Engineering*.

Destuynder P. and Fabre C., *On crack detection in NDT using Love waves* .

Baronian V., Bourgeois L. and Recoquillay A., *Imaging defects in an acoustic waveguide using timedependent*
surfacic data .

Siryabe E., Renier M., Meziane A., Galy J. and Castaings M., Apparent anistropy of an adhesive layer induced by imperfect interfaces and evaluation of interfaces stiffness's. .

Rowley W., Parnell W.J., Abrahams I.D. and Voisey R., *Design of acoustic beam shifters and related experiments*.

Favraud G. and Pagneux V., *A conformal mapping method for the scattering by rough surface*.

Joyce D., Abrahams I.D. and Parnell W.J., *Effective dynamic properties of complex non-linear composites*.

Bellis C., Bonnet M. and Cakoni F., *Acoustic inverse scattering using topological derivatives*.

Chabassier J. and Imperiale S., *Fourth order energy-preserving locally implicit discretization for linear wave equations*.

Junca S. and Legrand M., *Prestressed Nonlinear modes of a N degree-of-freedom system undergoing a purely elastic impact law* .

Lombard B., Favrie N. and Payan C., *Wave propagation in nonlinear elastic solids with slow dynamics*.

Devaux T., Tournat V., Richoux O. and Pagneux V., *Asymmetric acoustic propagation of wave packets via the self-demodulation effect*.

Massacret N., Ploix M.A. and Jeannot J.P., *Ultrasound propagation through Kelvin-Helmholtz instabilities*.

Hernando Quintanilla F., Fan Z., Lowe M. and Craster R., *2D and 3D Dispersion Loci of GuidedWaves in Viscoelastic Composites of General Anisotropy* .

Davey R., Assier R. and Hewitt R., *Guided Wave Vibration Techniques Applied to Hidden Tamper Detection*.

Theocharis G., *Energy transport in one-dimensional disordered granular solids*.

Le Thi H., Junca S. and Legrand M., *Periodic solutions with one sticking phase per period*.

Lynott G. and Hewitt R., *Ultrasonic Particle Separation*.

Van Pamel A., Huthwaite P., Brett C. and Lowe M., *Finite Element simulation of wave propagation in highly scattering materials.*.

Cell imaging with sub-optical wavelength ultrasound

Matt Clark, Rafael Fuentes, Leonel Marques, Emilia Moradi, Fernando Pérez-Cota, Richard J. Smith, and Kevin F. Webb
Applied Optics Group, University of Nottingham, University Park, Nottingham, UK
matt.clark@nottingham.ac.uk

1. Introduction

Ultrasound is the most widely used medical imaging technique, valued for its non-destructive nature and ability to image where there is no optical resolution. Optical microscopy is the most widely used cell imaging technique and light is used because it has a small wavelength and can achieve high spatial resolution.

Light is increasing being used in medical imaging (despite bodies being "opaque") because of its interesting contrast mechanisms (eg in optical tomography or photoacoustics) and ultrasound is beginning to offer possibilities for microscopy because, at high frequencies, ultrasound has the potential to surpass the resolution and contrast limits of light.

2. Photons for microscopy

In many ways photons are a poor choice for imaging live biological specimens: the wavelength of (visible) light restricts the resolution of microscopy systems below the limit where many significant biological processes occurs, many biological specimens exhibit little intrinsic optical contrast and the high photon energy can cause chemical reactions in the sample and leads to the dominance of photon shot noise in imaging.

Despite these shortcomings there are still many advantages of using light to image cells and tissue. Paradoxically many of these are the *same* as the disadvantages outlined above: the short wavelength gives high resolution, the lack of contrast means stains, labels and markers (contrast agents) can be used and are often required to see many structures, the high photon energy permits the use of fluorescent markers which leads to superresolution techniques such as STED and STORM which can extend defeat the Rayleigh limit. However, the resolution limit, the lack of intrinsic contrast and photon damage remain limitations for optical microscopy.

3. Phonons for microscopy

Ultrasonics offers an intriguing route to high resolution imaging: the speed of sound is typically five orders of magnitude lower than the speed of light and, at optical wavelengths, ultrasonic frequencies are in the GHz range (as opposed to 500THz for light) which are directly accessible using RF and pump-probe techniques. At GHz frequencies and above, ultrasound has the potential to provide higher resolution imaging than optical microscopy.

Many small-scale biological objects, such as cells, exhibit very little intrinsic optical contrast and without staining look like little more than transparent bags of water in a pool of water. For ultrasonic imaging the strongly varying mechanical properties of cellular structures may produce useful contrast [1–4]. Imaging of this mechanical contrast could aid the study of complex cell processes such as mitosis, division, differentiation, migration, force production, mechano-sensitivity and dynamic events.

The energy carried by a single phonon is very small compared with the energy of a photon of the same wavelength and the sound fields generated are relatively low amplitude so the ultrasound is not damaging in itself (however generating and detecting the ultrasound is problematic).

The potential for a new ultrasonic imaging technique with sub-optical resolution has inspired much research in GHz ultrasonics, for example, the scanning acoustic microscope (SAM) has been used for the acoustic imaging of biological cells [5]. It showed promise as a high resolution method of performing acoustic imaging and mechanical characterisation with minimal impact on cultured cells [1, 6, 7]. This implementation is practically difficult and is typically restricted to greater than optical wavelengths unless cryogenic couplants, such as liquid helium [8], are used (but these obviously can dramatically affect the acoustic properties and health of the sample).

The principle barrier to using high frequency ultrasound as an imaging tool is the extremely high attenuation at high frequencies which limits the distance that sound travels in biological samples to a few μm at GHz frequencies. It is for this reason that piezo-based technologies failed to work without cryogenic couplants. The use of laser ultrasound techniques means that the sound can be generated and detected at very high frequencies, very close to, or within the sample itself, and this (partially) overcomes the attenuation problem (figure 1 middle).

4. Cell imaging with picosecond laser ultrasonics

Picosecond laser ultrasound techniques have been used to generate and detect ultrasound with sub-optical wavelengths mainly in inanimate materials [9–12] and recently to measure the mechanical properties of biological cells [13–15]. We have been able to demonstrate ultrasonic imaging on fixed and live cells using picosecond laser ultrasonics with an acoustic wavelength of $\sim$270nm (figure 2) [16].

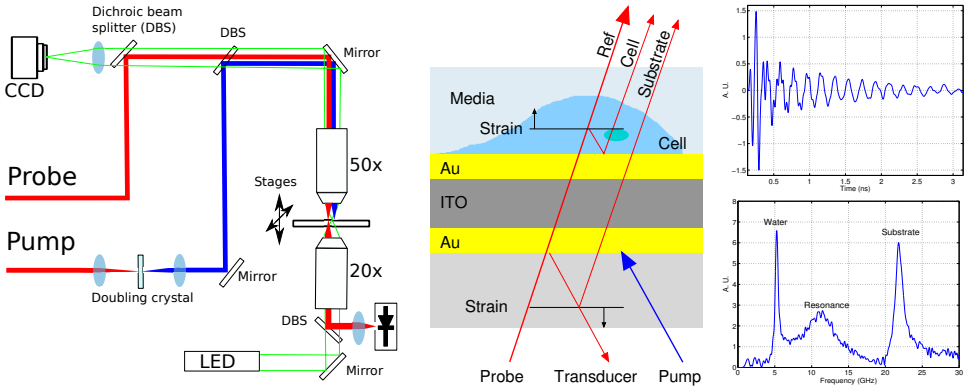

Fig. 1. PS measurement system. (left) schematic of optics, (middle) planar transducer system (not too scale), (right) typical signals

Our system consists of two lasers locked together in an ASOPs pump-probe configuration delivered to the sample through a phase-contrast fluorescence microscope (figure 1). For cell imaging we typically use three layer zero-order Fabry-Perot transducer and backside illumination for both pump and probe beams. The transducer protects the cell from excess light and help to reduce heat load and enhance the signal-to-noise ratio (SNR). We design the transducer, exploiting the optical resonances, to have high absorption at the (blue) pump wavelength, to resonantly split the (red) probe light and to separate the different signal components in frequency to aid analysis (figure 1 right).

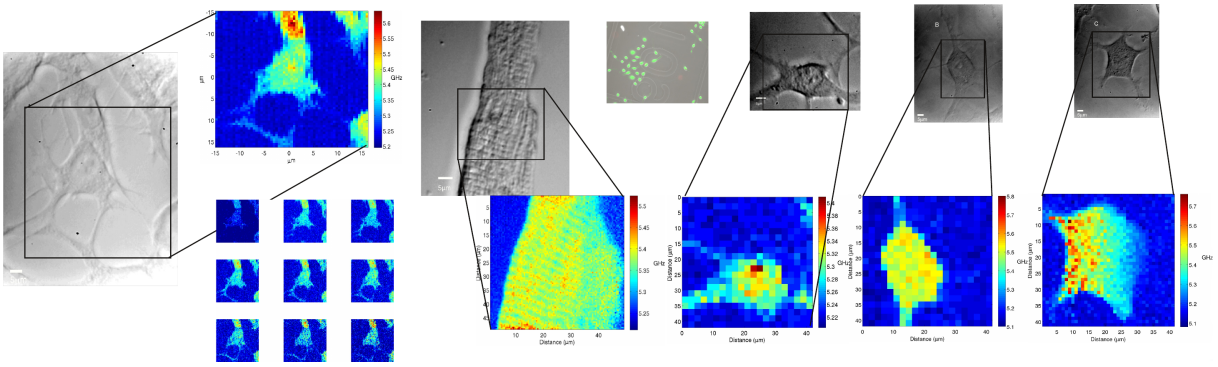

Fig. 2. Ultrasonic images of cells taken with sub-optical wavelength (270nm) ultrasound (greyscale optical, colour Brillouin frequency). Left to right: fixed 3T3 cells with 200nm sections, fixed cardiac myocyte showing sarcomeres, right live 3T3 fibroblasts.

Using this system we have been able to image and section a variety of fixed and living cells that were transferred and cultured on the transducer equipped substrates. Figure 2 shows Brillouin frequency maps which are sensitive to a combination of refractive index and sound velocity. However the refractive index contrast is thought to be weak and the majority of the contrast arises from the changes in sound velocity. In addition, the Brillouin time traces can be sectioned in time to section the sample in the axial direction and the transducer response can be imaged to reveal mass loading and adhesion [17].

5. Discussion

Imaging with ultrasound at optical resolutions or beyond is technically very difficult and, despite recent technical advances, formidable technical challenges remain before imaging with phonons can rival optical microscopy. Up to the present the principal problem has been the low SNR of the measurement in the non-destructive regime and this is particularly challenging for live cells as they have many vulnerabilities, their damage threshold is very low and the speed of imaging is very important to prevent movement and aging artifacts. However, it is now possible to measure with sufficient speed and SNR to image live cells.

While the difficulty compared with using fixed cells is considerable the importance of working with live cells cannot be over stated. Fixed cells are widely used in optical microscopy but the fixation doesn't significantly change the optical properties and preserves the cell. Fixation denatures and cross links proteins and is widely considered

to increase the mechanical strength and stability of specimens which clearly has the potential to change the elastic properties observed in ultrasonic microscopy.

Beyond increasing the imaging speed [18] and reducing the damage there is the significant problem of resolution. In any microscopy system the resolution is limited by maximum spatial frequency that can be generated or detected by the system and this is typically limited by the wavelength used (or the probe size in the case of scanning probe microscopy). In all picosecond laser ultrasonic systems thus far, the axial limit has been limited by the ultrasonic wavelength but the transverse limit has been limited to optical resolution because the optics limit the maximum ultrasonic spatial frequencies that can be generated or detected.

One possibility for overcoming the problem of the transverse resolution being pegged to the resolution of the underlying optics is to use sub-optical wavelength structures as generators and detectors of ultrasound. These can be used to generate sound with higher spatial bandwidths than the optics alone. There are many candidates for such structures including metallic nanoparticles, nanoshells, nanorods and nanowires. Each of these can be engineered, like the layered transducers, to have optical resonances which can be exploited to enhance the generation and detection of high frequency ultrasound. Figure 3 shows a signal from a single nanoparticle designed to strongly absorb the pump and resonantly scatter the probe, the signal arises because the breathing mode of the particle perturbs the resonant scattering which is picked up by the detectors.

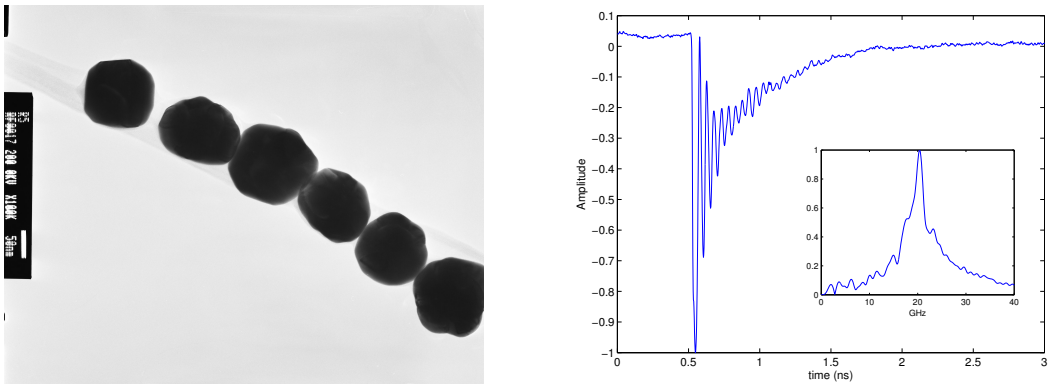

Fig. 3. (left) TEM images of gold nano particles, (right) acoustic response of a single nanoparticle

While the use of nanoparticles and nanostructures undoubtably provides a way to overcome the optical resolution limit and to generate and detect higher spatial frequencies, they are not sufficient in themselves to obtain transverse resolutions limited only by the diffraction limit of the ultrasonic waves. There remains an intriguing problem of how to control the ultrasonic fields at this small scale– *how to form beams*, *how to steer* them and *how to image* with them. There are several possibilities but these are highly speculative and form the basis for much future work.

Acknowledgements

The authors would like to thank the Engineering and Physical Sciences Research Council for funding this work through Grant EP/K021877/1 (Nano agents for read/write microscopy) and CONACYT for F. Pérez-Cota's post-graduate studentship.

References and links

1. J. Litniewski and J. Bereiter-Hahn, "Measurements of cells in culture by scanning acoustic microscopy," J. Microsc. **158**(1), 95–107 (1990).
2. M. Lekka, J. Lekki, M. Marszarek, P. Golonka, Z. Stachura, B. Cleff, and A.Z. Hrynkiewicz, "Local elastic properties of cells studied by SFM," Appl. Surf. Sci. **141**(3-4), 345–349 (1999).
3. D. P. Theret. "Application of the Micropipette Technique to the Measurement of Cultured Porcine Aortic Endothelial Cell Viscoelastic Properties," J. Biomech. Eng. **112**(3) 263 (2008).
4. S. Nawaz, P. Sánchez, K. Bodensiek, S. Li, M. Simons, and S. Iwan, "Cell visco-elasticity measured with AFM and optical trapping at sub-micrometer deformations," PloS one **7**(9) e45297 (2012).
5. J. A. Hildebrand, D. Rugar, R. N. Johnston, and C. F. Quate. "Acoustic microscopy of living cells," Proc. Natl. Acad. Sci. **78**(3), 1656–60 (1981).
6. T. Kundu, J. Bereiter-Hahn, and K. Hillmann, "Measuring elastic properties of cells by evaluation of scanning acoustic microscopy V(Z) values using simplex algorithm," Biophys. J. **59**(6), 1194–1207 (1991).
7. T. Kundu, J. Bereiter-Hahn, and I. Karl. "Cell property determination from the acoustic microscope generated voltage versus frequency curves," Biophys. J. **78**(5), 2270–9 (2000).
8. M. S. Muha, A. A. Moulthrop, G. C. Kozlowski, and B. Hadimioglu, "Acoustic microscopy at 15.3 GHz in pressurized superfluid helium," Appl. Phys. Lett. **56**(11) 1019 (1990).
9. P. A. Mante, J. F. Robillard, and A. Devos, "Complete thin film mechanical characterization using picosecond ultrasonics and nanostructured transducers: experimental demonstration on SiO_2," Appl. Phys. Lett. **93**(7) 071909 (2008).
10. P. Babilotte, P. Ruello, D. Mounier, T. Pezeril, G. Vaudel, M. Edely, J-M. Breteau, V. Gusev, and K. Blary, "Femtosecond laser generation and detection of high-frequency acoustic phonons in GaAs semiconductors," Phys. Rev. C **81**(24), 245207 (2010).
11. W. Chen, Y. Lu, H. Maris, and G. Xiao, "Picosecond ultrasonic study of localized phonon surface modes in Al/Ag superlattices," Phys. Rev. C **50**(19), 14506–14515 (1994).
12. O. Wright, B. Perrin, O. Matsuda, and V. Gusev, "Optical excitation and detection of picosecond acoustic pulses in liquid mercury," Phys. Rev. C **78**(2), 024303 (2008).
13. M. Ducousso, O. E.-F. Zouani, C. Chanseau, C. Chollet, C. Rossignol, B. Audoin, and M.C. Durrieu, "Evaluation of mechanical properties of fixed bone cells with sub-micrometer thickness by picosecond ultrasonics," Eur.Phys.J.-Appl Phys. **61**(1) 11201 (2013).
14. T. Dehoux and B. Audoin, "Non-invasive optoacoustic probing of the density and stiffness of single biological cells," Appl. Phys. **112**(12), 124702 (2012).
15. C. Rossignol, N. Chigarev, M. Ducousso, B. Audoin, G. Forget, F. Guillemot, and M. C. Durrieu, "In Vitro picosecond ultrasonics in a single cell," Appl. Phys. Lett. **93**(12), 123901 (2008).
16. F. Perez-Cota, R. J. Smith, E. Moradi, L. Marques, K. F. Webb, and M. Clark, "Thin-film opto-acoustic transducers for the sub-cellular Brillouin oscillations imaging of individual biological cells," Applied Optics **54** (2015).
17. R. J. Smith, F. Perez-Cota, L. Marques, X. Chen, A. Arca, K. Webb, J. Aylott, M. G. Somekh, and M. Clark, "Optically excited nanoscale ultrasonic transducers," J. Acoust. Soc. Am. **137**(1), 219–227 (2015).
18. R. J. Smith, R. A. Light, S. D. Sharples, N. S. Johnston, M. C. Pitter, and M. G. Somekh, "Multichannel, time-resolved picosecond laser ultrasound imaging and spectroscopy with custom complementary metal-oxide-semiconductor detector," Rev. Sci. Instrum. **81**(2), 024901 (2010).

Analysis of a locally resonant metamaterial for flexural waves in plates and Rayleigh waves in solids.

[1]Andrea Colombi, [1]Daniel Colquit, [1]Richard Craster, [2]Philippe Roux, [3]Sebastien Guenneau

[1]*Dept. of Mathematics, Imperial College London* andree.colombi@gmail.com

[2]*ISTerre Grenoble*

[3]*Institut Fresnel, Marseille*

Abstract

The exotic properties that characterizes a locally resonant metamaterial for flexural waves (A_0 mode) in thin plates are here in deep analyzed. A collection of closely spaced aluminum rods attached to a plate gives rise to bandgaps, slow waves, and hyperbolic properties. Using results from 3D numerical simulation, and high-frequency homogenization, we illustrate the propagation phenomena associated to the exotic points in the dispersion diagram. We present some application that exploits those dispersion properties and help achieving the extreme mechanical properties required to build a cloaking device or lenses for elastic waves.

Finally we extend the results to the case of the halfspace that supports Rayleigh and body waves and that give rise to an extremely rich variety of propagative modes.

1 Introduction

Elastic metamaterials [1] are attracting increasing attention in various branches of wave physics for their capacity of controlling elastic waves almost at will. A very promising subset of these metamaterials is represented by those based on local resonance effects. They are realized using so-called sub-wavelength resonators because of their characteristic size (in the plane of interest), far smaller compared to the wavelength. Laboratory experiments [2] and numerical simulations [3] have shown that when such metamaterials are excited by elastic or acoustic sources they give rise to two types of phenomena (1) band-gap effects, i.e. frequency bands in which elastic energy cannot propagate, or (2) sub-wavelength focusing, i.e. energy conversion on wavelength much smaller than the original propagated signal. These early experiments have been conducted on a cluster of closely spaced aluminium beams rigidly mounted on a thin aluminium plate excited by a source in the kHz's frequency range that excites A_0 Lamb waves in the plate. We now present a further development of this locally resonant metamaterial that exploits regions of the dispersion curves where the mechanical properties are exotic, featuring very low velocity, bandgaps and hyperbolicity.

Subwavelength bandgaps have recently been demonstrated with the full elastic system (Navier's equation), using resonators that may look like forest trees in the frequency range of 10's of Hz. In this case the underlying physics is similar to the case of the plate and therefore it is possible to achieve the same extent of wave control and the variety of phenomena demonstrated in the case of the plate.

Given the complexity of the physics, especially for the 3D case the use of Bloch theory and high-frequency homogenization becomes necessary providing interesting images of the modes.

2-Results

The applications discussed in this paragraph consider the metamaterial made by an aluminum plate and a cluster of rods randomly arranged on a subwavelength scale first introduced by [2,3]. Fig. 1a shows the numerical model used for the 3D simulations with flexural waves. Further details can be found in [2,3,4,5]

The plot in Fig. 1b shows the dispersion curves associated to the metamaterial previously described. The blue line is associated to the low frequency branch of the A_0 mode propagating outside the metamaterial (in the bare plate). The continuous black line shows the bandgaps (2.1-4 kHz) emerging as a result of the coupling between the A_0 mode, polarized out of plane, and the longitudinal resonances of the rods (Fig. 1b). Notice also that the in the region right before the bandgap, group and phase velocity are much lower compared to the plate velocity. On the other hand, the phase velocity of the hybrid mode after the bandgap exceeds the plate velocity.

This result can be explained in terms of effective material properties. The phase velocity v in the plate is defined by the following relationship:

$$v = \sqrt[4]{\frac{Eh^2\omega^2}{12\rho(1-\nu^2)}}; \qquad (1)$$

where k is the wavenumber, ω is the angular wave frequency, ϱ and E are the effective density and effective Young's modulus in the plate, respectively, h is the plate thickness, and ν is the Poisson's ratio. In Equation (1), both E and ϱ are effective parameters originated by the coupling between plates and beams, which make ν a function of the beam's length.

One first interesting possibility explored in this study is the realization of a lens for flexural waves. Maxwell or Eaton lens for instance, require strong velocity contrasts to obtain the correct refracting index. These contrasts are difficulty achieved unless one can locally modify plate thickness/Young modulus. On the other hand, the dispersion law in Fig. 1b provides the right velocity contrast over a narrow frequency bands preceding the bandgap and an appropriate circular arrangement of resonators with radially varying length can provide the sought contrast. This application might be interesting for waveguiding whereby waves can be focused/defocused or bent in different directions.

A more challenging application combines a radially varying velocity profile with the presence of a region protected from flexural waves at the center of the cluster of resonators. This object can realize a so-called "directional cloak". With the help of large 3D spectral element simulations and supercomputing facilities, we have designed a radially varying refractive index plate that allows directional invisibility cloaking of backward-scattered elastic waves. The directional cloak is based on a set of resonating beams that are attached perpendicular to the plate and are arranged at a sub-wavelength scale in few concentric rings. Numerical simulations clearly show that for certain beam configurations (i.e. beam's length), no back scattering and no penetration of elastic waves inside the cloak are obtained over a large frequency band.

To prove that this type of elastic metamaterials, previously limited to plates or acoustics cases, can crossover to the realm of surface waves we show some recent

results obtained propagating Rayleigh waves through a set of resonators that have a lengthscale relevant for seismic applications. A vertical point source located at the surface of a 2D semi-infinite half-space, 150 m long and 30 m deep, excites Rayleigh and body waves over a large frequency band (10-120 Hz). While the body waves disappear in the depth, the Rayleigh waves propagate along the surface toward a row of closely and randomly spaced resonators, which have properties similar to forest trees (Fig. 1c). Through numerical simulations we show how the propagation of the surface waves is deeply modified and characterized by large band gaps.

Finally, through Bloch analysis and mode analysis through high-frequency homogenization (Fig. 1d) we unveil some of the physics underlying this new and promising seismic metamaterial.

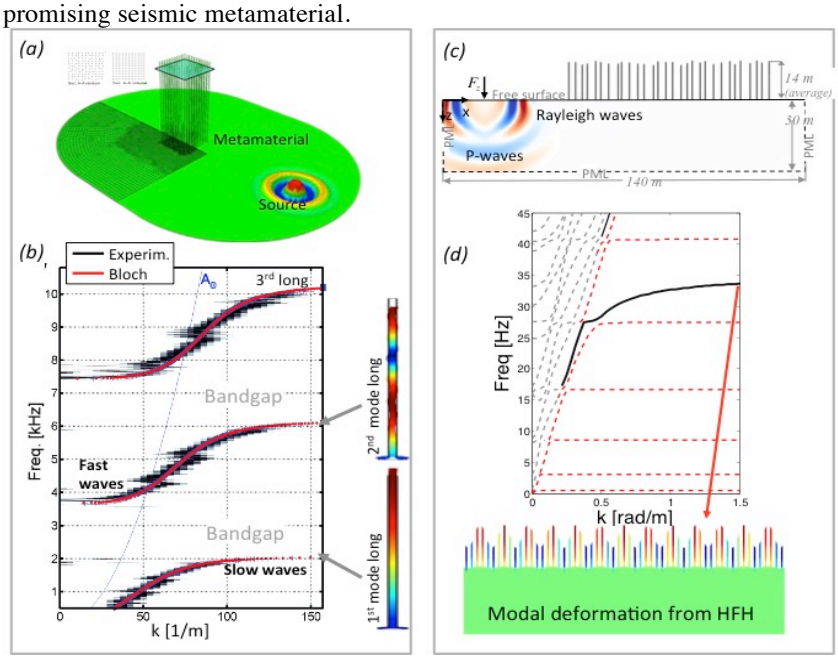

Figure 1 (a) The numerical model of the metamaterial made with plate and rods. (c) (Adapted from Williams et al (2015) and Colombi et al (2014)) Dispersion curves measured (black) and computed with Bloch theory (red) for the case of the plate. Arrows point to the respective modal deformation. The blue line shows the A_0 dispersion curve for the naked plate. (c) Model of the metamaterial for Rayleigh waves. (d) Dispersion curves calculated using Bloch theory and modal deformation from high frequency homogenization (HFH).

References

[1] R. Craster and S. Guenneau, Acoustic Metamaterials: Negative Refraction, Imaging, Lensing and Cloaking (London: Springer, 2012).

[2] Andrea Colombi, Philippe Roux, and Matthieu Rupin, Sub-wavelength energy trapping of elastic waves in a meta-material *Journal of the Acoustic Society of America,* **136**(2), EL192-196, 2014.

[3] Matthieu Rupin, Fabrice Lemoult, Geoffroy Lerosey and Philippe Roux Experimental demonstration of ordered and disordered multi-resonant metamaterials for Lamb waves, *Physical Review Letters*, **112**, 234301, 2014.

[4] Andrea Colombi, Philippe Roux, Sébastien Guenneau, and Rupin Matthieu Directional cloaking of flexural waves in a plate with a locally resonant metamaterial *The Journal of the Acoustical Society of America* **137** (4), 1783-1789, 2015.

[5] Earl G. Williams, Philippe Roux, Matthieu Rupin and W. A. Kuperman Theory of multi-resonant metamaterials for A0 Lamb waves *Physical Review* B, **91**, 104307, 2015.

Coupling plane wave representations and finite elements for the simulation of time-harmonic scattering in anisotropic media

Vahan Baronian, Anne-Sophie Bonnet-Ben Dhia, Sonia Fliss and Antoine Tonnoir

Abstract We consider the time-harmonic diffraction problem of elastic waves by a bounded defect in an anisotropic infinite medium. We derive an original formulation which is suitable for numerical computations: it consists in coupling several plane wave representations of the solution in half-planes and a finite element representation in a bounded area containing the defect.

1 Motivation

The development of non destructive techniques requires numerical simulation of time-harmonic wave propagation in large anisotropic structures, containing cracks or any other localized scatterers. A natural choice is to use finite elements to modelize the area around the scatterers, so that very arbitrary defects can be considered. This gives raise to a classical question: which boundary condition can be imposed at the artificial boundary of the finite element domain to avoid spurious reflections ?

There exist many techniques to do this in an infinite isotropic medium. The most popular approach is the PML method (where PML stands for Perfectly Matched Layer), which is both very simple to implement and very efficient. It is also possible to derive a transparent boundary condition, on a circular/spherical boundary, by using a radial decomposition on Bessel functions (see [3], [4]).

Unfortunately, these techniques fail in the case of anisotropic media. On one hand, in the PML technique, outgoing waves are selected by considering the phase

Vahan Baronian
CEA-List, Gif-sur-Yvette, France, e-mail: vahan.baronian@cea.fr

Anne-Sophie Bonnet-Ben Dhia and Sonia Fliss
POEMS (ENSTA Paristech, CNRS, INRIA, Université Paris Saclay), France, e-mail: anne-sophie.bonnet-bendhia@ensta-paristech.fr, sonia.fliss@ensta-paristech.fr

Antoine Tonnoir
INRIA, Université Paris Saclay, France, e-mail: antoine.tonnoir@inria.fr

velocity instead of the group velocity, which can lead to instabilities in the time domain and to a wrong solution in the frequency domain (see [1]). On the other hand, separation of polar/spherical variables does not work in anisotropic media.

In this work, we propose a new approach which is well-suited for homogeneous anisotropic media. The method is presented in the 2D case, but can be extended to the 3D case. The idea is to couple finite elements in a bounded domain containing the defect with Fourier representations of the elastic field in infinite half-planes. It has been inspired by a previous work [2] concerning periodic media. All the details can be found in the PhD thesis of Antoine Tonnoir [5].

2 The scattering problem, geometry and notations

We consider an infinite anisotropic elastic medium, supposed to be homogeneous, outside a bounded region containing the defects. To fix ideas, we suppose here that the defect is a cavity $\mathscr{O}$. The diffracted displacement field $\mathbf{u} = (\mathbf{u}_1, \mathbf{u}_2)$ has to satisfy the following equations

$$\left| \begin{array}{c} \operatorname{div} \sigma(\mathbf{u}) + \omega^2 \rho \mathbf{u} = 0 \quad \text{in} \quad \mathbb{R}^2 \setminus \mathscr{O} \\ \sigma(\mathbf{u}) \nu = \mathbf{g} \quad \text{on} \quad \partial \mathscr{O} \end{array} \right. \tag{1}$$

where ω is the pulsation, ρ the density and $\mathbf{g}$ is the source term related to the incident field. For simplicity, we suppose here that the material is viscoelastic and the stress tensor $\sigma(\mathbf{u})$ is linked to the strain tensor by a generalized Hooke's law. Then problem (1) has a unique solution $\mathbf{u} \in H^1(\mathbb{R}^2 \setminus \mathscr{O})^2$.

Let us suppose that the scatterer $\mathscr{O}$ is contained in the square $\Omega_a = [-a,a] \times [-a,a]$, itself contained in the larger square $\Omega_b = [-b,b] \times [-b,b]$, with $b \geq a$. We will denote by Ω_{int} the interior domain defined by $\Omega_{int} = \Omega_b \setminus \mathscr{O}$.

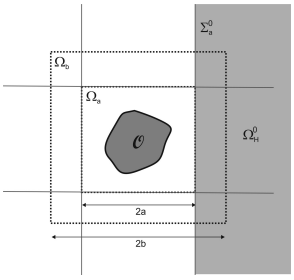

Fig. 1 Definition of the sub-domains used in the formulation

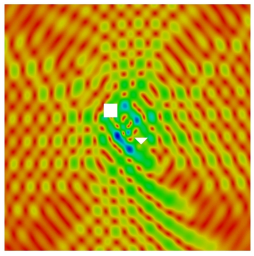

Fig. 2 Diffraction of a quasi-shear wave by defects in a strongly anisotropic material

Finally we introduce the four infinite straight lines and four half-planes which are adjacent to the square Ω_a:

$$\Sigma_a^0 = \{x = a\} \times \mathbb{R},\ \Sigma_a^1 = \mathbb{R} \times \{y = a\},\ \Sigma_a^2 = \{x = -a\} \times \mathbb{R},\ \Sigma_a^3 = \mathbb{R} \times \{y = -a\}$$
$$\Omega_H^0 = \{x \geq a\} \times \mathbb{R},\ \Omega_H^1 = \mathbb{R} \times \{y \geq a\},\ \Omega_H^2 = \{x \leq -a\} \times \mathbb{R},\ \Omega_H^3 = \mathbb{R} \times \{y \leq -a\}$$

and such that $\partial\Omega_H^j = \Sigma_a^j, \quad j = 0,1,2,3.$

3 A formulation using plane wave representations in half-planes

Taking advantage of the homogeneity of the medium in the half-planes Ω_H^j, we can give an explicit (integral) expression of the solution $\mathbf{u}$, given its trace φ^j on the boundary Σ_a^j. Applying a Fourier transform in the direction parallel to Σ_a^j, we get a coupled system of differential equations of order 2 with constant coefficients that we can solve explicitly. This gives an representation of $\mathbf{u}$ in the half-planes as a superposition of propagating and evanescent plane waves.

Then we derive a formulation where the unknowns are the solution $\mathbf{u}$ in the interior domain Ω_{int} and the four traces φ^j of the solution on the edges of the half-planes. Coupling relations are imposed to ensure the compatibility of the different representations in the intersections of adjacent half-planes, or in the intersection between one half-plane and the interior domain (when $b > a$).

This formulation is discretized by using 2D finite elements in Ω_{int} and 1D finite elements on the lines Σ_a^j. The approximations of the traces φ^j are supposed to vanish at some distance of the square Ω_a. Quadrature formulae are used to compute the Fourier integrals. Finally, a direct inversion of the matrix may be costly, because of the presence of full-blocks due to the integral operators. But thanks to the overlapping when $b > a$, we show that our method is well-suited for an iterative resolution using GMRES algorithm.

Once the problem is solved, knowing the traces φ^j enables to reconstruct a posteriori the solution in the half-planes (and therefore in the whole domain), which is impossible when using PML for instance (see Figure 2).

References

1. E. Bécache, S. Fauqueux and P. Joly. Stability of perfectly matched layers, group velocities and anisotropic waves. *Journal of Computational Physics*, 188(2):399–433, 2003.
2. S. Fliss and P. Joly. Exact boundary conditions for time-harmonic wave propagation in locally perturbed periodic media. *Applied Numerical Mathematics*, 59(9):2155–2178, 2009.
3. D. Givoli and J. B. Keller. Non-reflecting boundary conditions for elastic waves. *Wave Motion*, 12(3):261–279, 1990.
4. J. B. Keller and M. J. Grote. Exact nonreflecting boundary condition for elastic waves. *SIAM Journal on Applied Mathematics*, 60(3):803–819, 2000.
5. A. Tonnoir. Conditions transparentes pour la diffraction d'ondes en milieu élastique anisotrope. *PhD thesis*, Ecole Polytechnique, 2015.

A class of reduced-order models for elastic waves in a layer

C. J. Chapman

Abstract This paper shows that the numerical approach to elastic wave propagation in a layer given in Pagneux & Maurel (2001) admits a far-reaching but simple analytical treatment. Among the exact results obtainable, one is that the numerical approach of Pagneux & Maurel gives exact results, both for the dispersion relation and field shape, on an easily determined grid of points in the (frequency, wavenumber) plane. The mathematical methods used in the paper are Fourier series, barycentric representation, Euler truncation, and elimination of removable singularities by L'Hôpital's rule. Thus the methods used are elementary; they amount, in an unexpected way, to interpolation in the (frequency, wavenumber) plane, an idea which appears to be new. A principal finding in the paper is a class of reduced-order models, expressible in simple analytical terms, which display extraordinary numerical accuracy for both the field and dispersion relation, even at low order.

1 Introduction

The starting point for this paper is a recent method for obtaining a family of polynomial approximations to the dispersion relation for elastic waves in a layer [1, 2]. The next stage, to determine the corresponding approximations to the field, is the subject of the present paper. It will be shown that truncations of a suitable class of Fourier series leads to a more tractable analytical treatment than might be expected, via the intermediate stage of barycentric representation of the dispersion relation, and that the analytical results can be used to explain the numerical results in [3]. The paper can also be viewed as an extension, to arbitrary regions of the (frequency, wavenumber) plane, of the approach presented in [4], which is confined to

C. J. Chapman
Department of Mathematics, University of Keele, Staffordshire ST5 5BG, UK
e-mail: c.j.chapman@keele.ac.uk

a strip surrounding the frequency axis. The theory of barycentric approximations is explained in [5, 6, 7].

2 Fourier representation of the field

In standard notation, the field in an elastic layer can be represented as

$$u = hi\frac{V_2}{K}\left\{L_3^2 S(Y,L_1) - L_2^2 S(Y,L_2)\right\}, \qquad v = h\frac{U_1}{K}\left\{L_1^2 C(Y,L_1) - L_3^2 C(Y,L_2)\right\}, \quad (1)$$

where the functions S and C are defined by

$$S(Y,L) = \sum_{n'=1}^{\infty} \frac{(-1)^{n'}\sin\{(2n'-1)\pi Y\}}{\frac{1}{4}L^2 - \{(n'-\frac{1}{2})\pi\}^2}, \qquad C(Y,L) = \sum_{m'=0}^{\infty\prime} \frac{(-1)^{m'}\cos\{2m'\pi Y\}}{\frac{1}{4}L^2 - (m'\pi)^2}. \quad (2)$$

A prime on a summation indicates that the first term is to be halved. This representation gives a periodic extension of the field outside the layer region $|Y| \le \frac{1}{2}$, and has been chosen to make the extension continuous, but with discontinuities in slope at $|Y| = \pm\frac{1}{2}$. Another type of extension, analytic up to and well beyond the layer boundaries, is

$$u = hi\frac{V_2}{K}\left\{\frac{L_3^2 \sin\frac{1}{2}L_1}{L_1}\tilde{S}(Y,L_1) - L_2\sin(\tfrac{1}{2}L_2)\,\tilde{S}(Y,L_2)\right\}, \quad (3)$$

$$v = h\frac{U_1}{K}\left\{L_1^2\cos(\tfrac{1}{2}L_1)\,\tilde{C}(Y,L_1) - L_3^2\cos(\tfrac{1}{2}L_2)\,\tilde{C}(Y,L_2)\right\}, \quad (4)$$

where $\tilde{S}$ and $\tilde{C}$ are defined by $\tilde{S} = \tilde{S}_{\rm o} + \tilde{S}_{\rm e}$ and $\tilde{C} = \tilde{C}_{\rm o} + \tilde{C}_{\rm e}$ with

$$\tilde{S}_{\rm o}(Y,L) = \sum_{n'=1}^{\infty} \frac{-(2n'-1)\pi\sin\{(2n'-1)\pi Y\}}{\frac{1}{4}L^2 - \{(n'-\frac{1}{2})\pi\}^2}, \quad \tilde{S}_{\rm e}(Y,L) = \sum_{m'=1}^{\infty} \frac{2m'\pi\sin(2m'\pi Y)}{\frac{1}{4}L^2 - (m'\pi)^2}, \quad (5)$$

$$\tilde{C}_{\rm o}(Y,L) = \sum_{n'=1}^{\infty} \frac{-\cos\{(2n'-1)\pi Y\}}{\frac{1}{4}L^2 - \{(n'-\frac{1}{2})\pi\}^2}, \quad \tilde{C}_{\rm e}(Y,L) = \sum_{m'=0}^{\infty\prime} \frac{\cos(2m'\pi Y)}{\frac{1}{4}L^2 - (m'\pi)^2}. \quad (6)$$

The subscripts o and e indicate odd multiples $2n'-1$ and even multiples $2m'$ of πY appearing in the trigonometric terms. This extension has discontinuities at $|Y| = \pm 1$. Numerically, the former extension is more useful on the Rayleigh-wave branch of the dispersion relation, and the latter is more useful on the other branches.

3 Barycentric representation of the dispersion relation

When the above representations of the field are used in imposing the boundary conditions, and common factors cancelled, the dispersion relation takes the form

$$\frac{L_3^4}{K^2}\sum_{n'=1}^{\infty}\frac{(-1)^{n'}(2n'-1)\pi}{\frac{1}{4}L_1^2-\{(n'-\frac{1}{2})\pi\}^2}\ {\sum_{m'=0}^{\infty}}'\frac{(-1)^{m'}L_2}{\frac{1}{4}L_2^2-(m'\pi)^2} \;= \\ -L_1L_2\sum_{n'=1}^{\infty}\frac{(-1)^{n'}(2n'-1)\pi}{\frac{1}{4}L_2^2-\{(n'-\frac{1}{2})\pi\}^2}\ {\sum_{m'=0}^{\infty}}'\frac{(-1)^{m'}L_1}{\frac{1}{4}L_1^2-(m'\pi)^2}. \quad (7)$$

This is equivalent to representing the two tangents in the dispersion relation in barycentric form, i.e. as a ratio of two partial fraction expansions. Zeros in more than one denominator simultaneously are of exceptional physical importance, in defining the 'grid of resonances'. They are analysed in a straightforward way by L'Hôpital's rule or local expansion in differentials.

4 Reduced-order models

Truncations of the infinite series in (7) lead to a polynomial approximation to the dispersion relation which is exact on a grid of point in the (frequency, wavenumber) plane. Extremely high accuracy is obtained by using Euler truncation: the first member of this family is obtained from the rule 'add half the first term omitted'; the second member is obtained from the first two terms omitted, with coefficients $3/4$ and $1/4$; and so on to arbitrary order r, with appropriate coefficients [8, p. 161]. For each of these truncations, there is a corresponding truncation of the Fourier series representations of the field. These are the reduced-order models referred to in the introduction. They have remarkable numerical accuracy up to high frequencies and wavenumbers, even at low order. Full details, with extensive graphs and comparisons, are presented in [9], submitted for publication.

References

1. Chapman CJ, Sorokin SV. 2010 The finite-product method in the theory of waves and stability. *Proc. R. Soc. A* **466**, 471–491. (doi:10.1098/rspa.2009.0255)
2. Chapman CJ. 2013 An asymptotic decoupling method for waves in layered media. *Proc. R. Soc. A* **469**: 20120659. (doi:10.1098/rspa.2012.0659)
3. Pagneux V, Maurel A. 2001 Determination of Lamb mode eigenvalues. *J. Acoust. Soc. Am.* **110**, 1307–1314. (doi:10.1121/1.1391248)
4. Kaplunov J, Nolde E, Rogerson GA. 2006 An asymptotic analysis of initial-value problems for thin elastic plates. *Proc. R. Soc. A* **462**, 2541–2561. (doi:10.1098/rspa.2006.1687)
5. Schneider C, Werner W. 1986 Some new aspects of rational interpolation. *Mathematics of Computation* **47**, 285–299.

6. Berrut J-P, Trefethen LN. 2004 Barycentric Lagrange interpolation. *SIAM Review* **46**, 501–517. (doi:10.1137/S0036144502417715)
7. Trefethen LN. 2013 *Approximation theory and approximation practice*. Philadelphia, USA: SIAM.
8. Press WH, Teukolsky SA, Vetterling WT, Flannery BP. 1992 *Numerical recipes in Fortran. 2nd edition*. Cambridge, UK: Cambridge University Press.
9. Chapman CJ, Sorokin SV. 2015 A class of reduced-order models in the theory of waves and stability. *Proc. R. Soc. A* (submitted).

Veering of dispersion curves and prestress effects in multi-wire helical waveguides

Fabien Treyssède

Abstract Guided wave based methods are of potential interest for the non destructive evaluation of cables. However, the understanding of mechanisms governing the propagation of guided waves is particularly complicated owing to the helical and multi-wire structure of strands, the basic elements constituting cables. The complexity of the problem is further increased by the effect of high tensioning forces applied on cables. A typical dispersion curve veering phenomenon, sensitive to the applied loads, occurs in seven-wire strands, a common type of strands in modern constructions. The main goal of this paper is to highlight the origin of this phenomenon.

1 Introduction

Based on a semi-analytical finite element (SAFE) method, recent progress has been made in the modeling of wave propagation in seven-wire strands [1, 2]. Nevertheless, some works are still required. A typical dispersion curve veering phenomenon occurs for the fundamental longitudinal mode. This phenomenon, sometimes referred to as *notch frequency*, has been observed both experimentally [3] and numerically [1] but its origin is still unexplained. Besides, the notch frequency significantly increases with applied loads. This increase turns out to be essentially caused by interwire contact effects, as shown by numerical tests [2]. However, the convergence of numerical results has to be assessed. In particular, further works are needed to quantitatively check the modeling of contact with reference solutions.

IFSTTAR, GERS, GeoEND, F-44340 Bouguenais, France, e-mail: fabien.treyssede@ifsttar.fr

2 Numerical method

SAFE modeling of helical waveguides under prestress. The application of a SAFE method consists in assuming a axial harmonic dependence of acoustic fields before finite element discretization, so that only the cross-section needs to be meshed. With this technique, the axial variables must be separable. For helical strands, this separation is possible with a specific curvilinear coordinate system, called twisting coordinate system [1, 4], which has constant non zero torsion but zero curvature. In order to acount for prestress effects, one starts from the so-called linearized updated Lagrangian formulation of non-linear mechanics (see for instance Ref. [5]). This formulation is here extended to twisting coordinates and adapted to a SAFE formulation. The SAFE method finally leads to the following kind of eigensystem, characterizing the elastic guided modes in prestressed strands:

$$\{\mathbf{K}_1 - \omega^2\mathbf{M} + ik(\mathbf{K}_2 - \mathbf{K}_2^T) + k^2\mathbf{K}_3\}\mathbf{U} = \mathbf{0}, \tag{1}$$

The matrices $\mathbf{K}_i$ (i=1,2,3) include geometric stiffness terms related to the Cauchy prestress of the static state. Further details can be found in Refs. [2].

Static contact modeling. The first step of the analysis is to compute the static prestress state. One starts from the homogenization method described in Ref. [6]. In this paper, an iterative procedure is used to properly account for contact, based on a node-to-node procedure together with a direct elimination method [7]. As the axial load is incremented, contact pairs of nodes are formed on both sides of the initial point-to-point interwire contact zone, until the prescribed axial strain ε is reached.

3 Results

Notch frequency phenomenon and interwire contact effects. The cross-section of the seven-wire strand (steel) is meshed with six-node triangles and refined at contact regions. Based on the static model, the contact half-width is computed as a function of the normal contact force up to the prescribed axial strain ε=0.6%. Good agreement is found with Hertz analytical solution for parallel cylinders (results not shown for paper conciseness). Based on the SAFE model, Figure 1a shows the notch frequency phenomenon of the fundamental longitudinal mode, usually denoted as $L(0,1)$. The notch frequency increases from 0.32 (62Hz) in the unloaded case to 0.42 (82Hz) in the loaded case. These values are in agreement with the experiments of Refs. [3, 8]. The notch frequency corresponds to a curve veering phenomenon between the dispersion curves of two distinct longitudinal-like wave modes [1], labeled as $L(0,1)a$ and $L(0,1)b$. As recalled in Sec. 1, its increase is indeed mainly due to the increase of interwire contact width rather than prestress itself [2]. In order to briefly assess convergence, Fig. 1a also gives results with a refined mesh (46893 dofs): changes are negligible for the loaded case, thus indicating a good accuracy

with the initial mesh. Convergence can yet hardly be achieved for the unloaded case, somehow purely theoretical, because the contact width tends to zero.

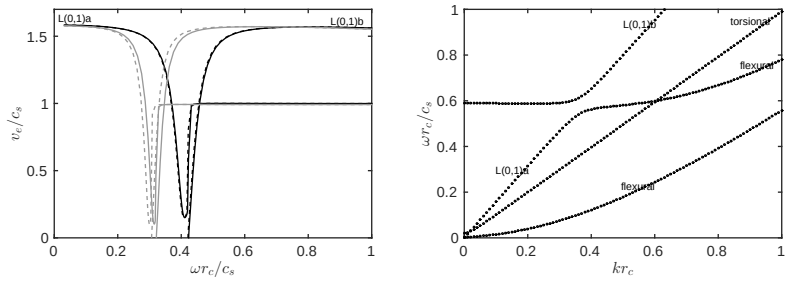

(a) (b)

Fig. 1: (a) Curve veering for ε=0% (gray) and for ε=0.6% (black), continuous lines: initial mesh (12369 dofs), dashed lines: refined mesh (46893 dofs). (b) Dispersion curves in the (k,ω) plane for the uncoupled blocked peripheral wire.

The uncoupled peripheral wire. Following the analysis of Ref. [9], curve veering phenomena usually occur in a weakly coupled system and may be predicted from the uncoupled system. Let us consider an uncoupled peripheral wire, radially blocked along its contact width. Blocking the radial displacement in such a narrow region completely breaks the circular symmetry of the wire and, as opposed to the free cylinder case, the compressional, flexural and torsional motions get fully coupled. A curve veering actually occurs, in a very similar fashion as for the fully coupled strand. This veering is due to the coupling between two modes, one of longitudinal type and the other of flexural type, as shown in the (k,ω) plane by Fig. 1b. It can be inferred that the origin of the notch frequency inside seven-wire strands lies in the radial displacement constraint imposed on peripheral wires by the central one.

References

1. F. Treyssède and L. Laguerre. *J. Sound Vib.*, 329:1702–1716, 2010.
2. F. Treyssède, A. Frikha, and P. Cartraud. *Int. J. Solids Struct.*, 50:1383–1393, 2013.
3. H. Kwun, K. A. Bartels, and J. J. Hanley. *J. Acoust. Soc. Am.*, 103:3370–3375, 1998.
4. F. Treyssède. *J. Acoust. Soc. Am.*, 129:1857–1868, 2011.
5. K. J. Bathe. *Finite Element Procedures*. Prentice Hall, Englewood Cliffs, New Jersey, 1996.
6. A. Frikha, P. Cartraud, and F. Treyssède. *Int. J. Solids Struct.*, 50:1373–1382, 2013.
7. P. Wriggers. *Computational Contact Mechanics*. Springer-Verlag, Berlin, 2006.
8. L. Laguerre, M. Brissaud, and J. C. Aime. *Bull. Liaison Lab. Ponts Chaussées*, 239:7–27, 2002.
9. B. R. Mace and E. Manconi. *J. Acoust. Soc. Am.*, 131:1015–1028, 2012.

A Generic GTD-Kirchhoff Scattering Model for Ultrasonic NDT of Planar Defects

Michel DARMON, Vincent DORVAL, Audrey KAMTA DJAKOU, Larissa FRADKIN, Sylvain CHATILLON

Abstract Simulation is helpful for evaluating the performances of inspection techniques and requires the modeling of waves scattering from defects.

Two classical flaw scattering models have been previously evaluated and implemented in the CIVA platform developed by CEA/LIST to deal with planar defects: the geometrical theory of diffraction (GTD) and the Kirchhoff approximation (KA). These two approaches appear to be complementary. Combining them so as to retain only their advantages, we have developed a combined model (the so-called Kirchhoff & GTD) based on the Physical Theory of diffraction (PTD).

Both theoretical and experimental validations of the Kirchhoff & GTD model have been carried out in various practical NDE (pulse echo and TOFD) configurations studying both direct and corner echo modes. Theoretical validations have consisted in comparisons between this new model and other scattering models (GTD, KA and a finite-element method).

Whereas the previously existing models were notably useful to respectively simulate specular reflection echoes for Kirchhoff and edges diffractions for GTD, the performed validations have shown that the Kirchhoff & GTD model provides a generic modeling of both the two main scattering phenomena arising from a planar flaw: specular reflection and edges diffraction.

1 Principle of the Kirchhoff & GTD model

The Kirchhoff model is useful for the modelling of echoes due to specular reflections but is less accurate for observation directions far from the specular one since it doesn't model correctly and quantitatively edges diffraction. On the other hand, contrary to Kirchhoff, the GTD model is not valid for specular observation

Michel DARMON, Vincent DORVAL, Audrey KAMTA DJAKOU, Sylvain CHATILLON
CEA, LIST, Department Imaging and Simulation for NDT, F-91191 Gif-sur-Yvette cedex, France, e-mail: michel.darmon@cea.fr

Audrey KAMTA DJAKOU. Also at Laboratoire d'Acoustique de l'Université du Maine (LAUM) UMR CNRS 6613, 72085 Le Mans, France

Larissa FRADKIN, Sound Mathematics Ltd., Cambridge, CB4 2AS, U.K, e-mail: l.fradkin@soundmathematics.com

direction since the GTD coefficient diverges but GTD is very effective to predict edge diffractions echoes in most configurations.

The developed Kirchhoff & GTD model (Zernov et al., 2012) is devoted to the simulation of both reflection and diffraction echoes from crack-like flaws. It is based on the Physical Theory of Diffraction (PTD) (Ufimtsev, 2007) which consists in correcting the Kirchhoff edge diffraction field by that modelled by GTD. The PTD field is the sum of the Kirchhoff field and a GTD modified field in which the GTD coefficient has been replaced by the difference between GTD and Kirchhoff edge diffraction coefficients:

$$\mathrm{U}^{PTD}(\mathrm{x}) = \mathrm{U}^{\mathrm{KA}}(\mathrm{x}) + \left[D_{\alpha\beta}^{GTD}(\mathrm{x}) - D_{\alpha\beta}^{KA}(\mathrm{x}) \right] \frac{\mathrm{e}^{ikr}}{\sqrt{kr}} \tag{1}$$

At the specular observation direction, the Kirchhoff field is finite leading to an effective prediction of specular reflection. But the GTD $D_{\alpha\beta}^{GTD}(\mathrm{x})$ and Kirchhoff $D_{\alpha\beta}^{KA}(\mathrm{x})$ edge diffraction coefficients diverge but have the same singularity. When making the difference of the two coefficients, their singularities cancel each other and the diffraction coefficients difference $D_{\alpha\beta}^{GTD}(\mathrm{x}) - D_{\alpha\beta}^{KA}(\mathrm{x})$ is finite. Consequently the PTD scattered field is spatially uniform and presents no singularity at the specular observation direction unlike GTD. The Kirchhoff field is then predominant compared to the edge diffraction contribution and the Kirchhoff & GTD model leads to similar results than the Kirchhoff model:

$$\mathrm{U}^{PTD}(\mathrm{x}) \approx \mathrm{U}^{\mathrm{KA}}(\mathrm{x}) \tag{2}$$

When the observation direction is far from to the specular direction, edge diffraction effects are predominant compared to reflection phenomena, the Kirchhoff field is equal to the Kirchhoff edge diffraction contribution and so cancels it so that the Kirchhoff & GTD model leads to similar results than the GTD model.

$$\mathrm{U}^{\mathrm{KA}}(\mathrm{x}) \approx D_{\alpha\beta}^{KA}(\mathrm{x}) \frac{\mathrm{e}^{ikr}}{\sqrt{kr}} \text{ and } \mathrm{U}^{PTD}(\mathrm{x}) \approx D_{\alpha\beta}^{GTD}(\mathrm{x}) \frac{\mathrm{e}^{ikr}}{\sqrt{kr}} = \mathrm{U}^{GTD}(\mathrm{x}) \tag{3}$$

Flaws which can be modelled thanks to Kirchhoff & GTD are the same than with the GTD model: planar flaws (rectangular, semi-elliptical or CAD contour planar flaws), multi-facetted flaw and branched flaw.

2 Validations of the Kirchhoff & GTD model

As example, for P waves, in Figure 1, the Kirchhoff & GTD model leads to a very good agreement with FEM for all tilt angles. A logical equivalence with KA is observed near the specular reflection configuration (α=90°) and with GTD (not represented here for simplification) for a diffraction configuration. In the latter case, the Kirchhoff model leads to prediction errors for tilt angles corresponding to observation directions far from the specular one.

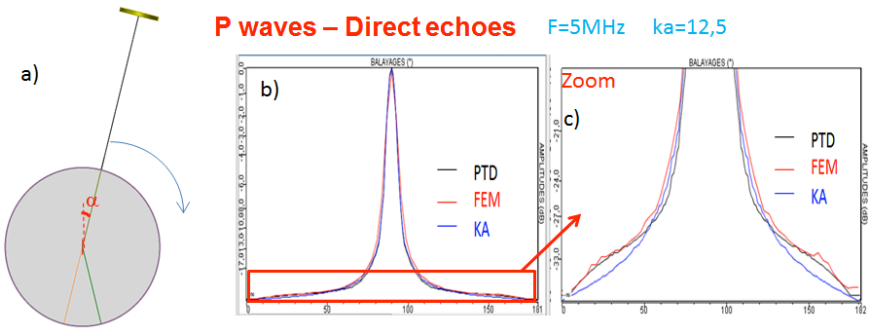

Figure 1: a) inspection at 5MHz with P waves of various incidences of a rectangular 5mm high defect b) and c) zoom: comparison of the simulated echoes amplitude in dB versus the tilt angle α for different 2D models: FEM, Kirchhoff (KA) and Kirchhoff & GTD (PTD).

Satisfactory experimental validations (Darmon et al., 2016) of the developed PTD model have also been obtained in both pulse echo and TOFD configurations.

References

Darmon, M., Dorval, V., Kamta Djakou, A., Fradkin, L., and Chatillon, S. (2016). A system model for ultrasonic NDT based on the Physical Theory of Diffraction (PTD). Ultrasonics *64*, 115–127.

Ufimtsev, P.Y. (2007). Fundamentals of the Physical Theory of Diffraction (Hoboken, USA: John Wiley & Sons.).

Zernov, V., Fradkin, L., and Darmon, M. (2012). A refinement of the Kirchhoff approximation to the scattered elastic fields. Ultrasonics *52*, 830–835.

Bearing defects prediction using Empirical Wavelet Transform

M. Er-raoudi, M. Diany, H. Aissaoui, M. Mabrouki

Abstract: Rolling bearing elements are a mechanical components considered as the most widespread parts in machines. However, its operating conditions are not always ideal. This causes defects and may reduce the machine service life. The real-time monitoring of the bearing vibration is essential to detect and classify the defects.
This work simulates a three-degree-of-freedom system of rotating ball bearings introducing defects and detects their presence using Empirical Wavelet Transform. The results of this new approach are discussed and compared with the Empirical decomposition mode.

1 Background

1.1 Empirical Mode Decomposition

The Empirical Mode Decomposition (EMD) is an adaptive method, proposed by Huang et al. [1], aims to decompose a signal into a sum of N + 1 components called Intrinsic Mode Functions (IMFs) $f_k(t)$ [2]:

$$f(t) = \sum_{K=0}^{N} f_k(t) \tag{1}$$

1.2 Empirical Wavelet

The construction of the Empirical wavelets (EW) is equivalent to the construction of Band-pass filters. The empirical scaling function and the empirical wavelets are expressed by equations (2) and (3), respectively [2].

$$\hat{\phi}_n = \begin{cases} 1 & if \quad |\omega| \le \omega_n - \tau_n \\ \cos\left[\frac{\pi}{2}\beta\left(\frac{1}{2\tau_n}\left(|\omega| - \omega_n + \tau_n\right)\right)\right] & \text{if} \quad \omega_n - \tau_n \le |\omega| \le \omega_n + \tau_n \\ 0 & otherwise \end{cases} \tag{2}$$

M.Er-raoudi
Faculty of Sciences and Techniques, Beni Mellal, e-mail: erraoudi.mina@gail.com

M.Diany
Faculty of Sciences and Techniques, Beni Mellal , e-mail: m.diany @yahoo.fr

$$\hat{\psi}_n = \begin{cases} 1 & if \quad \omega_n + \tau_n \le |\omega| - \tau_{n+1} \\ \cos\left[\frac{\pi}{2}\beta\left(\left(\frac{1}{2\tau_{n+1}}\left(|\omega| - \omega_{n+1} + \tau_{n+1}\right)\right)\right)\right] & \text{if} \quad \omega_{n+1} - \tau_{n+1} \le |\omega| \le \omega_{n+1} + \tau_{n+1} \\ \sin\left[\frac{\pi}{2}\beta\left(\frac{1}{2\tau_n}\left(|\omega| - \omega_n + \tau_n\right)\right)\right] & \text{if} \quad \omega_n - \tau_n \le |\omega| \le \omega_n + \tau_n \\ 0 & otherwise \end{cases} \tag{3}$$

2 Modelization

In the rolling element bearing model, all bearing components are considered: Inner race, outer race, ball and lubrication film between races and balls [3].

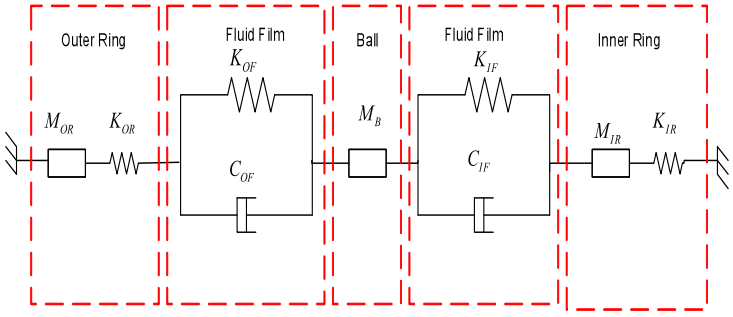

Figure 1: The mechanical Model of bearing system [3]

Where M_{OR},M_B and M_{IR} are respectively the Outer Race, ball and Inner Race mass.
K_{OR}, K_{OF},K_{IF}, and K_{IR} are respectively the outer race ,outer race fluid film,inner race fluid film and inner race stiffness.
C_{OR} and C_{IF} are the outer and the inner race damping
Excitation forces (F_1, F_2, F_3) corresponding to the loading in the presence of defects which can affect the inner race, outer race, cage and ball [4].
The motion equations are:

$$\begin{cases} M_{OR}\ddot{y}_1 + C_{OF}\dot{y}_1 - C_{OF}\dot{y}_2 + (K_{OR} + K_{OF})\,y_1 - K_{OF}y_2 = F_1 \\ M_B\ddot{y}_2 - C_{OF}\dot{y}_1 + C_{OF}\dot{y}_2 - K_{OF}y_1 + (K_{OF} + K_{IF})\,y_1 = F_2 \\ M_{IR}\ddot{y}_3 - C_{IF}\dot{y}_2 + C_{IF}\dot{y}_3 - K_{IF}y_3 + (K_{IR} + K_{IF})\,y_1 = F_3 \end{cases} \tag{4}$$

Where (y_1, y_2 , y_3) represent the displacements along the radial direction.

3 Kinematics of rolling bearing defect

Assuming that both races may rotate, the outer and inner races are respectively rotating at a constant speed □0 and □i; the frequencies generated by a bearing are [5]:

$$FTF = \frac{1}{2}\left[\omega_i\left(1-\frac{B_d\cos(\theta)}{P_d}\right)+\omega_i\left(1+\frac{B_d\cos(\theta)}{P_d}\right)\right] \quad (5)$$

$$BPFO = \frac{N_b}{2}\left(1-\frac{B_d\cos(\theta)}{P_d}\right)\omega \quad (6)$$

$$BPFI = \frac{N_b}{2}\left(1+\frac{B_d\cos(\theta)}{P_d}\right)\omega \quad (7)$$

$$BSF = \frac{N_b}{2}\left(1+\left(\frac{B_d\cos(\theta)}{P_d}\right)^2\right)\omega \quad (8)$$

Where B_d is the ball diameter, P_d is the pitch diameter, N is the number of rolling elements and □ is the contact angle, BPFO is the ball pass frequency on an outer race defect, BPFI is the ball pass frequency on an inner race defect, FTF is the fundamental train frequency; BSF is the ball spin frequency.

4 Numerical simulation

The equation 4 is solved using simulink/matlab. Indeed, Wavelet Transform lets to extract more information's form the vibratory signal in the presence of shocks [6] [7] .In the present study we have considered the Wavelet Transform with a specific Wavelet (EW). A comparative study is made between EMD and EWT, which showed that all of the two methods lets us to detect bearing shocks. This simulation gives good result for EWT detection relatively to the EMD. The EMD gives too many modes while the EWT lets to separate different AM-FM modes composing the signal.

5 Conclusion

This work is devoted to bearing fault prediction based on the Empirical Wavelets Transform. The obtained results demonstrates that the EWT is a powerful tool in the field of bearing health monitoring.

References

[1] N.E. Huang and Z. Shen and S.R. Long and M.C. Wu and H.H. Shih and Q. Zheng and N-C. Yen and C.C. Tung and H.H. Liu, The empirical mode decomposition and the Hilbert spectrum for nonlinear and nonstationary time series analysis, Proc. Royal Society London A., vol. 454, pp. 903–995, 1998

[2] Jerome Gilles, Empirical wavelet transform, IEEE trans. On signal processing, vol. Xx, no. Xx, February 2013.

[3] S.Sassi, B.Badri,M.Thomas,A Numerical Model to Predict Damaged Bearing Vibrations, Journal of Vibration and Control, 13(11):1603–1628, 2007.

[4] N.Tandon. and A. Choudhury., An analytical model for the prediction of the vibration response of rolling element bearings due to a localized defect,Journal of Sound and Vibration205(3), 275–292,1997.

[5] Thomas, M., 2002, Fiabilité, maintenance prédictive et vibrations de machines,(in French) ETS editions, Montréal,Canada.

[6] M.Er-raoudi ,M.Diany,H.Aissaoui ,M.Mabrouki,Détection des défauts d'engrenages en se basant sur les réseaux de neurones et la transformée en ondelettes discrète,2eme édition du Congrès International de Génie Industriel et Management des Systèm,Fès,Maroc,2015.

[7] M.Er-raoudi , M.Diany,H.Aissaoui ,M.Mabrouki,Détection et analyse des défauts de dentures d'engrenages par la Transformée en ondelettes et la Transformée de Hilbert , Journées Doctoriales, université sultan moulay slimane, Béni Mellal,Maroc,2015.

Junction of acoustic waveguides at low frequencies; application to periodic media

Jean Kergomard

Abstract When the walls are rigid, the fundamental mode of waveguides or cavities is uniform. For the case of waveguides, this mode is the unique mode propagating at low frequencies. For this reason, the junction between several waveguides can be represented asymptotically as the combination of an acoustic compliance and a matrix of acoustic masses. Examples are given for 2, 3 or 4 guides. A particular example is that of a junction of a cylindrical tube and a truncated cone.

1 Introduction

The purpose of this paper is the study of solutions of the Helmholtz equation in a set of waveguides with perfectly rigid walls. For cylindrical pipes, the fundamental pressure mode is the planar one (with zero transverse eigenfrequency), with is uniform over a cross section. Similarly for closed (3D) cavities the fundamental mode is uniform, with a zero eigenfrequency. Using these peculiarities, we derived the behavior of the junction of a waveguide set at low frequencies. This behavior exists for other shapes of waveguides, such as conical waveguides: the fundamental mode has a spherical symmetry.

The paper presents the general formulation for the junction of a waveguide set, then the example of the junction of a cylinder with a cone.

2 Formulation of the junction of several waveguides

Figure 1 shows the junction of 3 cylindrical guides, with a junction cavity of volume V. The integral equation that links the acoustic pressure $p(\mathbf{r})$ and velocity $v(\mathbf{r})$ normal to the surface is written as:

$$p(\mathbf{r}) = j\omega\rho \int_S G(\mathbf{r},\mathbf{r}')v(\mathbf{r}')dS'. \tag{1}$$

ω is the angular frequency, ρ the air density, $G(\mathbf{r},\mathbf{r}')$ the Green's function of the cavity when it is closed. A useful feature is the modal expansion:

$$G(\mathbf{r},\mathbf{r}') = \frac{c^2}{V}\sum_{mnp}\frac{\boldsymbol{\phi}_{mnp}(\mathbf{r})\boldsymbol{\phi}_{mnp}(\mathbf{r}')}{\omega_{mnp}^2-\omega^2} \tag{2}$$

where c is the speed sound, and ω_{mnp} the eigenfrequencies of the modes $\boldsymbol{\phi}_{mnp}(\mathbf{r})$. The first mode $\boldsymbol{\phi}_{000}(\mathbf{r})$ is uniform, with $\omega_{000}=0$. Therefore the dependence of two first terms of the expansion of $G(\mathbf{r},\mathbf{r}')$ is ω^{-2}, then 1.

Eq. (1) can be projected on the modes of each guide i, which are chosen to be dimensionless and constitute the vector $\boldsymbol{\psi}_i$. The dimension of this vector is infinite. This leads to the following impedance matrices $\mathbf{Z}_{ij}$ for the guides i and j:

$$\mathbf{Z}_{ij} = \frac{j\omega\rho}{S_iS_j}\int_{S_i}\int_{S_j}\boldsymbol{\psi}_i G(\mathbf{r},\mathbf{r}')\,{}^t\boldsymbol{\psi}_j dS_i dS_i'. \tag{3}$$

A basic hypothesis is the absence of interaction of the two extremities of each guides, i.e., the absence of overlap between evanescent modes at the two extremities. The impedance matrix for these modes is diagonal, involving the characteristic impedances. Handling sub-matrices with this hypothesis allows the reduction of the impedance matrix to the propagating modes, i.e., at low frequencies to the fundamental modes, as follows:

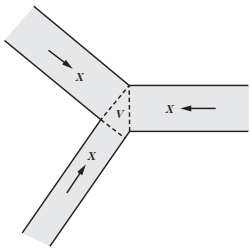

Fig. 1 Junction of 3 cylindrical waveguides with junction cavity of volume V

Jean Kergomard
Laboratoire de Mecanique et d'Acoustique CNRS - 4 impasse Nikola Tesla CS 40006 13453 Marseille Cedex 13 , e-mail: kergomard@lma.cnrs-mrs.fr

$$\begin{pmatrix} P_0 \\ P_1 \\ P_2 \end{pmatrix} = \left[\frac{\rho c^2}{j\omega V} \begin{pmatrix} 1 & 1 & 1 \\ 1 & 1 & 1 \\ 1 & 1 & 1 \end{pmatrix} + j\omega \begin{pmatrix} M_{00} & M_{01} & M_{02} \\ M_{10} & M_{11} & M_{12} \\ M_{20} & M_{21} & M_{22} \end{pmatrix} + O(\omega^3) \right] \begin{pmatrix} U_0 \\ U_1 \\ U_2 \end{pmatrix} \quad (4)$$

P_i and U_i are the amplitude of the planar mode pressure and flow rate in guide i. The first term corresponds to the compressibility effect, while the second corresponds to inertial effect: the matrix $\mathbf{M}$ is proportional to ρ (for an incompressible fluid, it can be found by solving the Laplace equation for different boundary conditions). $\mathbf{M}$ is symmetric (reciprocity). When the volume V vanishes, the total flow rate vanishes too, and the N equations are replaced by $N-1$ equations, obtained by writing the difference between 2 equations.

3 Examples and applications

Several examples of junctions of 2, 3 or 4 cylindrical waveguides for which the volume V is zero have been treated in many papers [2, 3, 4, 5]). Recently we treated the junction of a cylinder with a cone, and improved previous results. A particular case of the latter problem is the radiation of a cylindrical pipe into an infinite flange [7], and the present formulation leads to excellent approximations up to the first cutoff $\omega = 3.84c/R$, under the condition that the zero-frequency length correction (0.8216 times the radius R) is known [6].

This low-frequency model can be used for non-interacting discontinuities, i.e., in general for guides with transverse dimensions much smaller than the length between two discontinuities. Then a general model can be deduced for the coupling of two waveguides by perforations, or, more generally, for guides with periodic discontinuities. The example of perforated tube mufflers is well known. A generalization to various applications can be done, thanks to an analytical calculation of 4th order matrices, corresponding to a medium with two waves in each direction [4].

References

1. J. Kergomard, A. Lefebre, G. Scavone, Acta Acustica united with Acustica 101 (2015) 1189-1198.
2. Fock, V. Doklady Akad. Nauk. SSSR) **31**, 875–878 (1941)
3. J.C. Bruggeman, J. Acoust. Soc. Am. 82 (1987) 1045-1051.
4. J. Kergomard, A., Khettabi, X. Mouton. Acta Acustica 2 (1994) 1-16.
5. V. Dubos, J. Kergomard, A. Khettabi, J.P. Dalmont, D. Keefe, C.J. Nederveen, Acustica united with Acustica, 85 (1999) 153- 169.
6. P.A. Martin, J. Eng. Math. 71 (2011) 291–304.
7. A.N.Norris, I.C. Sheng. J. Sound Vib. 135 (1989) 85-93.

Huang Hilbert Transform based procedure for multi-crack identification of beams under a moving excitation

H. Chouiyakh, L. Azrar, K.Alnefaie and O. Akourri

Abstract Non destructive testing is concerned by techniques of damage detection in structures, e.g. ultrasonic, eddy-current, radiographic, acoustic emission testing, etc. Those procedures can be classified as local techniques for non destructive testing. Otherwise, the global techniques are mainly concerned by vibration based methods. The present work aims first to study free and forced vibrations of multi-cracked beams (forward problem) and secondly to analyze the obtained signals by Huang Hilbert Transform (Inverse problem) for cracks identification. The cracks are assumed to be open and modeled through rotational spring model. In this paper, the use of this transform for cracks detection is highlighted. Instantaneous frequency will be investigated as damage index tool.

1. Short overview of the Huang Hilbert Transform

The Huang Hilbert transform (HHT) consists of empirical mode decomposition and Hilbert spectral analysis.The Empirical mode decomposition (EMD) is a technique representing non linear and non-stationary signals as sum of simpler components called Intrinsic Mode Functions (IMFs). The decomposition is performed through a repeated sifting procedure. At the end, the time signal x(t) can be expressed in terms of n number of IMFs:

$$x(t) = \sum_{j=1}^{n} c_j(t) + r_n(t) \tag{1}$$

where $c_j(t)$ is the j^{th} intrinsic mode function and $r_n(t)$ is the residue. The Hilbert transform is then applied to each of those components, in order to get instantaneous frequency plots. Hilbert Transform (HT) of the function $c_j(t)$ is defined by [4]:

$$H(c_j(t)) = h_j(t) = \frac{1}{\pi}\int_{-\infty}^{+\infty}\frac{c_j(\tau)}{t-\tau}d\tau \tag{2}$$

The instantaneous amplitude $A_j(t)$ and phase $\theta_j(t)$ are given respectively by:

$$A_j(t) = \sqrt{(c_j(t))^2 + (h_j(t))^2} \qquad \theta_j(t) = \arctan\left(\frac{h_j(t)}{c_j(t)}\right) \tag{3}$$

Instantaneous frequency (IF) measures the rate and direction of a phase in the complex plane, and is defined as the derivative of the phase $\theta_j(t)$:

H. Chouiyakh
Faculty of Sciences and Techniques, Tangier; Morocco, e-mail: hajar.chouiyakh@gmail.com
L.Azrar
Faculty of Sciences and Techniques, Tangier; Morocco e-mail: azrarlahcen@yahoo.fr

$$\omega_j(t) = \frac{d\theta_j(t)}{dt} \tag{5}$$

2. Vibration of beams carrying moving excitation

Let us consider an Euler-Bernoulli uniform beam containing 'r' cracks and subjected to a travelling load F(x,t). The transverse displacement of each segment of the beam is denoted by $y_i(x,t)$ and the partial differential equation governing the motion of each sub-beam is :

$$EI\frac{\partial^4 y_i(x,t)}{\partial x^4} + c\frac{\partial y_i(x,t)}{\partial t} + \rho A\frac{\partial^2 y_i(x,t)}{\partial t^2} + \alpha\frac{\partial^5 y_i(x,t)}{\partial x^4 \partial t} = F_0 \sin(\Omega t)\delta(x - Vt) \quad i = 1,2,...,r+1. \tag{6}$$

where ρ , A, c and α are mass density, cross sectional area, damping coefficient, viscoelastic coefficient respectively. In order to find eigenmodes and eigenfrequencies of the considered multi-cracked beam, one has to solve the following boundary value problem for each sub-beam i: [2]

$$\begin{cases} \dfrac{\partial^4 w_{ij}(x)}{\partial x^4} - \mu_j^4 w_{ij}(x) = 0 \ ; \ \mu_j^4 = \dfrac{\rho A}{EI}\omega_j^4 \quad i = 1,2,3,...,r+1; \ \ j = 1,2,3,....,N \\ + \ \text{Boundary} \quad \text{Conditions} \end{cases} \tag{7}$$

where w_{ij} is the local displacement associated to the j^{th} vibration mode of the i^{th} sub-beam and ω_j is the j^{th} eigen frequency . In order to solve the present problem, the following compatibility equations at cracks locations are incorporated:

$$\begin{cases} w_{ij}(x_i) = w_{(i+1)j}(x_i) \\ w''_{ij}(x_i) = w''_{(i+1)j}(x_i) \\ w'''_{ij}(x_i) = w'''_{(i+1)j}(x_i) \end{cases} \tag{8-a}$$

$$\begin{cases} w'_{(i+1)j}(x_i) = w'_{ij}(x_i) + C_i w''_{ij}(x_i \\ \overline{C_i} = \dfrac{2h}{EI} f\left(\dfrac{a_i}{h}\right) \end{cases} \tag{8-b}$$

where: $f\left(\dfrac{a_i}{h}\right) = (5.93 - 19.69\left(\dfrac{a_i}{h}\right) + 37.14\left(\dfrac{a_i}{h}\right)^2 - 35.84\left(\dfrac{a_i}{h}\right)^3 + 13.12\left(\dfrac{a_i}{h}\right)^4)$

By using the modal expansion theory the set of decoupled time differential equations is obtained:

$$\ddot{q}_j(t) + \left(\frac{c}{\rho A} + \alpha\frac{\omega_j^2}{EI}\right)\dot{q}_j(t) + \omega_j^2 q_j(t) = \frac{F_0}{M_{jj}} w_j(Vt) \qquad j = 1,2,...., \overline{N} \tag{10}$$

Vibration of the multi-cracked beams is a problem of big interest. With high number of cracks, this problem needs well adapted mathematical procedures in order to overpass the numerical implementation and computation difficulties and particularly when the spring model is adopted. The differential quadrature method (DQM) is elaborated here for the space and time domains.

3. Numerical results

Various numerical results are obtained and only some of them are presented here. Accuracy and convergence of the elaborated differential quadrature method is demonstrated in Table 1.

B-C	Analytical approach			DQM (N=150)			Error %	
	μ1	μ2	μ3	μ1	μ2	μ3	μ1	μ2
Pinned-Pinned	3,13409	6,26525	9,39787	3,13409	6,26525	9,39787	$6{,}732\text{x}10^{-8}$	$-7{,}66\text{x}10^{-9}$
Clamped-Free	1,87014	4,68749	7,84055	1,87014	4,68749	7,84055	$2{,}513\text{x}10^{-7}$	$-1{,}05\text{x}10^{-7}$
Clamped-Clamped	4,72552	7,84087	10,9687	4,72552	7,84087	10,9687	$-1.22\text{x}10^{-8}$	$-1{,}30\text{x}10^{-8}$
Clamped-pinned	3,92157	7,05630	10,1870	3,92157	7,05630	10,1870	$3{,}57\text{x}10^{-8}$	$-2{,}52\text{x}10^{-8}$

Table 1: First three natural frequencies of beams containing four cracks with various B-C

Huang Hilbert Transform is a powerful tool for detection, and localization of considered cracks. By analyzing obtained signals, on can see clearly that instantaneous frequency can be considered as a damage index since the curve presented in Figure1 shows accurately positions of all considered cracks.

Figure 1: Multi-crack detection of a beam containing eight equally spaced cracks

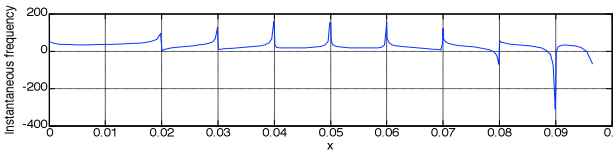

4. Conclusion

A methodological approach based on the differential quadrature method and the HHT is elaborated for multi-cracks identification. The HHT are applied to the computed eigenmodes as well as to the computed forced responses. This work demonstrates robustness of HHT in detection of cracks by using linear vibration responses. Instantaneous frequency plots are used for cracks identification.

References

[1] Boller, C., Fou-Kuo, C., & Yozo, F. (2009). *Encyclopedia of structural health monitoring.* John Wiley & Sons.

[2] Chouiyakh, H., Azrar, L.,Alnefaie, K., Akourri, O. (2014). Multicracks identification of beams based on moving harmonic excitation and wavelet transforms,submitted to *Structural Engineering and Mechanics* .

[3] Cohen, L. (1995). *Time frequency analysis.* New Jersey: Prentice-Hall PTR.

[4] Feldman, M. (2011). Tutorial Review: Hilbert transform in vibration analysis. *Mechanical Systems and Signal Processing*,735–802.

Analytical solution for the diffuse scattered field of elastic waves at randomly rough surfaces

Fan Shi[1], Michael J.S. Lowe[1], Elizabeth Skelton[2], and Richard Craster[2]

Abstract

There is a growing interest in elastic wave scattering from randomly rough surfaces nowadays, with applications in Non-destructive evaluation (NDE) and seismology. In NDE it is important to know the expectation of the scattering intensity and its angular distribution, as the information can be used for optimizing the detection by selecting inspection angles where a reasonably large scattering amplitude can be measured. Knowledge of the expected intensity is also vital for the approval and qualification of proposed inspection procedures. The expected value can be obtained as a sample average of quantities via the Monte Carlo method. However, while this can provide the results for any case of interest, it does not inform the underlying link between the roughness and the scattered field. Moreover it can be very tedious and time-consuming to accumulate the many solutions to be averaged, for example multiple Finite Element simulations. Analytical methods provide alternatives since the surface statistics are embedded into the formulae, and the relationship between the roughness and the scattering properties can be revealed. The analytical solution for the coherent intensity has been found by Ogilvy for elastic waves [1]. However, no analytical solutions for the diffuse intensity have been developed so far.

In this work, we present the development of an elastodynamic theory for the diffuse field using the Kirchhoff approximation (KA). Analytical solutions are derived for predicting the diffuse intensity with a wide range of roughness within the valid region of the KA [2]. This enables the analytical prediction of the expected intensity of the reflection and mode conversion of elastic waves from surfaces of

Fan Shi,
Mike Lowe, Department of Mechanical Engineering, Imperial College London SW7 2AZ, e-mail: f.shi12@imperial.ac.uk

Elizabeth Skelton,
Richard Craster, Department of Mathematics, Imperial College London SW7 2AZ

given statistical roughness. The theory is then verified by numerical Monte Carlo simulations and also experiments using phased arrays.

Furthermore, we apply the theory to analytically investigate the impact of the roughness and elasticity on the mode conversion, and consequently on the scattering intensity for different modes. In addition, the 3D roughness-induced depolarization is also investigated.

[1] J. A. Ogilvy. *Theory of Wave Scattering from Random Rough Surfaces*. Adam Hilger Ltd., 1991.

[2] F. Shi, W. Choi, E. A. Skelton, M. J. S. Lowe and R. V. Craster. 'The validity of Kirchhoff theory for scattering of elastic waves from rough surfaces'. *Proc. R. Soc. A*, 471:1-9, 2015.

Objective defect characterisation using ultrasonic phased array data

Katherine M. M. Tant and Anthony J. Mulholland

Abstract Ultrasonic phased array systems are playing an increasingly important role in the maintenance of safety-critical structures. Information on the presence and nature of defects can be extracted from the data collected by these multi-element arrays via imaging algorithms. However, the resulting flaw characterisations are dependent on the choice of threshold at which the defect measurements are made, thus producing ambiguous results. The work discussed here endeavours to eliminate this aspect of subjectivity by developing an explicit formula for the crack length as a function of the frequency domain scattering matrix. Due to the formulaic nature of this work, conclusions can be drawn on the method's sensitivity to various experimental parameters which can then be corroborated using synthetic data. Finally, the algorithm is modified and applied to experimental data and an objective measurement of 6.4mm is reached for a crack with actual length 6mm.

1 Introduction

Ultrasonic non-destructive testing is vital for the life-extension and maintenance of safety critical structures such as those found in the nuclear, oil, and aerospace industries. The development of ultrasonic phased array transducers and the subsequent collection of full matrix capture (FMC) data [2] has allowed advances to be made in the reconstruction of the interiors of key structural components. Defects can be detected and characterised using imaging algorithms such as the total focussing method (TFM) [2] and phase coherent imaging (PCI) [1]. However, accurate characterisation can sometimes be impeded as these imaging algorithms are typically reliant on the choice of threshold at which the defects are measured and thus an aspect of ambiguity is introduced. To combat this, a mathematical expression for crack size derived from the Born approximation is presented. This model based approach to measuring cracks is entirely objective and allows the effects of varying the system parameters to be studied. To corroborate the conclusions drawn from the analysis, ultrasonic phased array inspections have been simulated

Katherine M. M . Tant
University of Strathclyde, Livingstone Tower, 26 Richmond Street, Glasgow, G1 1XH.
Email: katy.tant@strath.ac.uk

Anthony J. Mulholland
University of Strathclyde, Livingstone Tower, 26 Richmond Street, Glasgow, G1 1XH.
Email: anthony.mulholland@strath.ac.uk

using the finite element package PZFlex. The algorithm is subsequently modified to allow successful application to experimental data.

2 Model-based crack sizing

An alternative to image based crack sizing has previously been examined in [5] where it was shown that a correlation existed between the crack length and the properties of its associated scattering matrix. The work presented here builds on this premise and extends the analysis of a method developed in previous work by the authors [3] where use of the roots of the pulse-echo response (the diagonal of the scattering matrix) allowed the formulation of a mathematical expression for the crack length. The scattering of a pressure wave by an ellipsoidal inclusion in an elastic medium is considered via the Born approximation. The following expression for the crack length a is then derived

$$a = \sqrt{\frac{M^2\lambda^2}{4\pi^2}\csc^2(\phi_i + \theta) - 4a_2^2\cot^2(\phi_i + \theta)} \tag{1}$$

where M=4.49341, λ is the wavelength, θ is the crack orientation (relative to the x axis) and $\phi_i = \operatorname{atan}(x_i/r)$, the angle between the vertical axis and the vector connecting the centre of the flaw at depth r to the element at which the root occurs along the pulse echo response, x_i.

From equation (1), formulae for the minimum resolvable crack length, the optimal experimental parameters for the characterization of a specified range of crack lengths and the expected error due to discretization by the array pitch [3] can also be derived.

3 Results

The crack-sizing formula was tested using synthetic data generated in the finite element package PZFlex. To test the method's limitations, a 3MHz ultrasonic phased array inspection of a sub-wavelength crack of length 1.4mm, embedded in a steel block, was simulated. On examination of the resulting scattering matrix, the defect was correctly identified as a crack and an objective measurement of 2mm was obtained. The TFM (in its most basic form) produced a similar defect measurement (dependent on thresholding) however the resulting image suggested that the flaw was volumetric [4]. The benefit of an objective method for defect characterisation was thus shown.

For application to experimental data it was decided that, to extend the method's capabilities and combat the introduction of experimental noise and scattering by the microstructure, the entire scattering matrix should be exploited. Hence, a multi-frequency optimization method was developed where the scattering matrices

over the bandwidth of the transducer were compared to those arising from the Born approximation over a range of crack lengths. This algorithm was applied to FMC data arising from the phased array inspection of welded austenitic plates containing a 6mm lack-of-fusion crack (see Figure 1 (a)) and an objective measurement of 6.4mm was obtained. To reiterate the benefit of an objective approach to crack sizing, a reconstruction of the 6mm crack by the TFM (in its most basic form) is shown in Figure 1 (b) and the subjective nature of imaging algorithms is thus demonstrated.

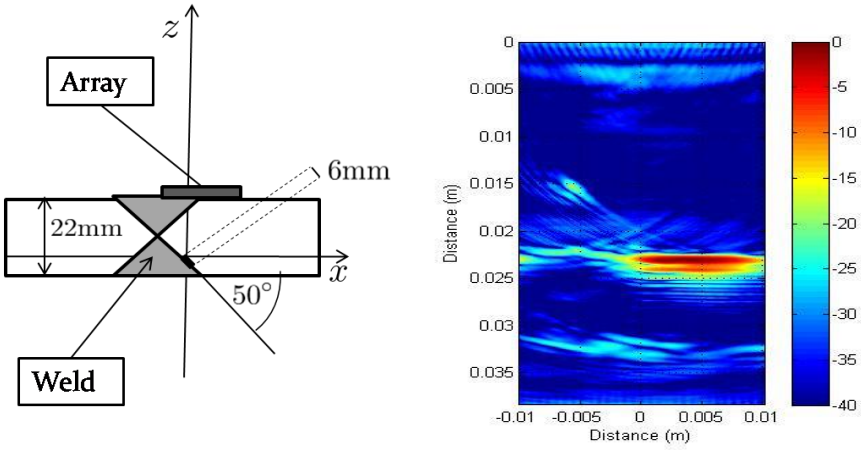

(a) (b)

Figure 1: (a) A schematic of the phased array inspection of the 6mm lack-of-fusion crack between two welded austenitic plates. (b) The resulting TFM reconstruction from the collected FMC data.

References

1. Phase Coherent Imaging. **J Camacho, M Parrilla and C Fritsch.** 2009, IEEE TUFFC, Vols. 56, nO 5, pp. 958-974.

2. Post-processing of the full matrx of ultrasonic transmit receive array data for nondestructive evaluation. **C Holmes, B W Drinkwater and P D Wilcox.** 2005, NDT Int, Vols. 38, No 8, pp. 701-711.

3. *A Model-Based Approach to Crack Sizing With Ultrasonic Arrays.* **K M M Tant, A J Mulholland, A Gachagan.** May 2015, IEEE TUFFC, Vols. 62, No 5, pp. 915-926.

4. *An analytical approach to objectively sizing cracks using ultrasonic phased array data.* **K M M Tant, A J Mulholland, A Gachagan.** September 2015, BINDT Conf. Proc. Telford, U.K.

5. *The use of ultrasonic arrays to characterise crack-like defects.* **J Zhang, B W Drinkwater and P D Wilcox.** 2010, J. NDE, Vols. 29, No. 4, pp. 222-232.

Ultrasonic particle sizing in non-dilute suspensions

Raied S. Al-Lashi[*], and Richard E. Challis[**]
[*] School of Food Science and Nutrition, Faculty of Mathematics and Physical Sciences, University of Leeds, UK.
[**]Faculty of Engineering, Department of Mechanical Engineering, Imperial College, UK.
Correspondence Email: R.Al-lashi@leeds.ac.uk

Abstract
Particle size distributions (PSDs) in solid-in-liquid suspensions can be estimated from ultrasonic attenuation measurements based on using a wave propagation model. In this model, the estimated attenuation is adaptively fitted to the measured data across frequency range. The current wave propagation model breaks down at high solid concentration. This is more likely due to the use of continuous phase viscosity instead of the effective viscosity of the mixture surrounding particles. This presentation shows the PSDs estimation from incorporating effective viscosity formulations into the wave propagation model. It has been found that the Happel model provides the best estimate of the PSD in high concentration suspensions.

Interfacial waves and neutrality for semi-infinite platonic crystals

S. G. Haslinger, R. V. Craster, A. B. Movchan, N. V. Movchan, I. S. Jones

Abstract We present new results for localisation and transmission of flexural waves in a structured elastic plate comprising a semi-infinite two-dimensional array of rigid pins. Trapped waves close to the interface of the homogeneous part of the Kirchhoff-Love plate and the part containing the rigid pins are analysed. The connection between the dispersion properties of flexural Bloch-Floquet waves and the semi-infinite platonic crystal considered here is demonstrated using the discrete Wiener-Hopf technique.

1 Introduction

Since the 1980's, there has been substantial attention devoted to wave interaction with periodic structures leading to the recent surge of interest in designing metamaterials, photonic crystals and micro-structured media that are able to generate effects unattainable by natural media. Many of the concepts originate in electromagnetism and optics but are now filtering into other systems such as the Kirchhoff-Love plate equations for flexural waves. This analogue of photonic crystals, labelled as platonics by [1], features many of the effects from photonics such as ultra-refraction, negative refraction, Dirac-like cones and cloaking [2, 3, 4] amongst others.

The Kirchhoff-Love equations are good approximations and capture much of the essence of the wave physics. Multipole methods extending pins to cylinders [5], or high-frequency homogenization approaches [6] to get effective continuum equations that encapsulate the microstructure, have emerged relatively recently. For finite pinned regions of a plate, a Green's function approach [7] leads to rapid numerical solutions, or for an infinite grating, one may use an elegant method for exploring Rayleigh-Bloch modes. This includes extensions to stacks of gratings and the trapping and filtering of waves [8]. A natural extension is to consider semi-infinite gratings, or edge states in semi-infinite lattices, and here we present exact solutions, together with illustrative examples of localisation and other wave phenomena.

S.G. Haslinger, A.B. Movchan, N.V. Movchan
University of Liverpool, Department of Mathematical Sciences, Liverpool L69 7ZL, UK e-mail: sgh@liverpool.ac.uk

R.V. Craster
Imperial College, London SW7 2AZ, UK

I.S. Jones
Liverpool John Moores University, Liverpool L3 3AF, UK

2 Formulation

For an infinite Kirchhoff-Love plate with a semi-infinite array of rigid fixed pins, the equation of motion for the amplitude of flexural displacement $U(\mathbf{r})$ is

$$\Delta^2 U(\mathbf{r}) - \beta^4 U(\mathbf{r}) = \sum_n A_n \delta(\mathbf{r} - \mathbf{r}'_n), \tag{1}$$

with $U(\mathbf{r}'_n) = 0$. The diffracted field is of the form

$$U(\mathbf{r}) = \sum_{n=0}^{\infty} A_n G_n^q(\beta; \mathbf{r}), \tag{2}$$

where A_n are to be determined and G_n^q is a quasi-periodic grating Green's function defined in the form:

$$G_0^q(\beta, x; \kappa_y, d_y) = \frac{i}{8\beta^2} \sum_{j=-\infty}^{\infty} \left[H_0^{(1)}\left(\beta\sqrt{(jd_y)^2 + x^2}\right) + \frac{2i}{\pi} K_0\left(\beta\sqrt{(jd_y)^2 + x^2}\right) \right] e^{i\kappa_y j d_y}. \tag{3}$$

Here d_y is the vertical period and κ_y is the corresponding Bloch parameter.

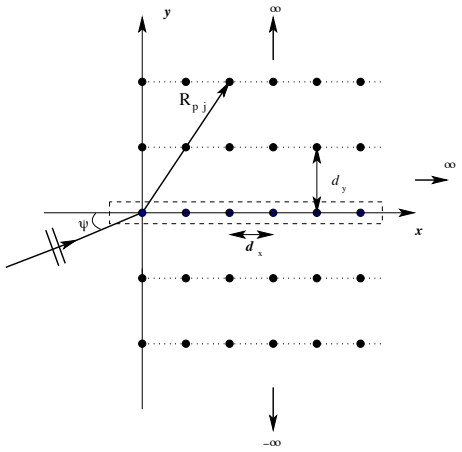

Fig. 1 The semi-infinite lattice of rigid pins, consisting of an array of infinite gratings with period d_y in the vertical direction and horizontal spacing d_x. The single semi-infinite grating is also highlighted. A plane wave is incident at an angle ψ for the rectangular lattice illustrated here.

The gratings are centred at points $(nd_x, 0)$ for $n \geq 0$ (see Fig. 1) and we introduce displacements at pins (nd_x, jd_y) such that $b_n = 0$ for $n \geq 0$ but are unknown for $n < 0$. Referring to (2), $A_{-n} = 0 \ \ \forall n > 0$ since there are no sources on the left-hand side. For an incident plane wave, we have

$$e^{ind_x\beta\cos\psi} + \sum_{m=0}^{\infty} A_m G_m^q(\beta|n-m|d_x; \kappa_y, d_y) = b_n, \quad n \in \mathbb{Z}. \tag{4}$$

Following the discrete Wiener-Hopf treatment of [9] for the Helmholtz problem for a single semi-infinite grating, we employ the z-transform and sum over all n:

$$\sum_{n=-\infty}^{\infty} z^n e^{ind_x\beta\cos\psi} + \sum_{n=-\infty}^{\infty}\sum_{m=0}^{\infty} A_m G^q_{n-m}(\beta|n-m|d_x;\kappa_y,d_y)z^n = \sum_{n=-\infty}^{\infty} z^n b_n. \qquad (5)$$

Defining $A(z)$,$\mathscr{K}(z)$ as z-transforms, (5) becomes a single functional equation of the Wiener-Hopf type:

$$F(z)+A(z)\mathscr{K}(z)=B(z), \qquad \text{where} \quad B(z)=\sum_{n=1}^{\infty} b_{-n}z^{-n}, \qquad (6)$$

and the kernel function $\mathscr{K}(z)$ is connected with the doubly quasi-periodic Green's function when $z=e^{i\kappa_x d_x}$ with $\kappa_x=\beta\cos\psi$.

3 Illustrative examples

We present displacement fields associated with semi-infinite arrays using the discrete Wiener-Hopf method outlined above and results obtained for a truncated semi-infinite array analysed with a method attributable to [10]. We adopt a wave-vector

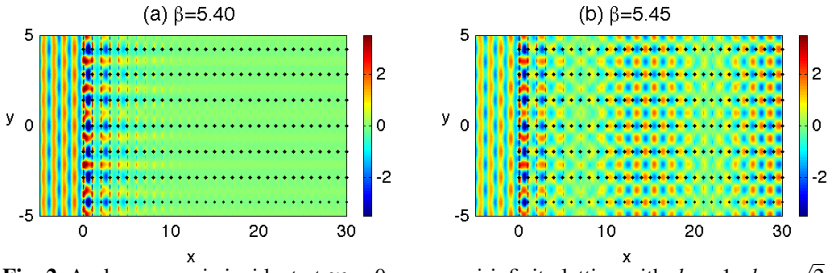

Fig. 2 A plane wave is incident at $\psi=0$ on a semi-infinite lattice with $d_x=1$, $d_y=\sqrt{2}$. (a, b) Total displacement field for $\beta=5.40, 5.45$ respectively.

diagram strategy, analogous to that demonstrated by [11] for electromagnetism, to show that the platonic crystal system supports localised interfacial waves, amongst other dynamic effects associated with stationary and Dirac-like points on the dispersion surfaces for the doubly periodic array. For a plane wave incident at $\psi=0$ on a semi-infinite array of gratings with $d_x=1.0$ and $d_y=\sqrt{2}$ we plot the real part of the total displacement field for $\beta=5.40$ and 5.45 in Figs. 2(a, b). For $\beta=5.40$ the localised interfacial wave clearly dominates any action inside the pinned region whilst $\beta=5.45$ supports both edge localisation and wave propagation.

Acknowledgements The authors thank the EPSRC (UK) for their support through the Programme Grant EP/L024926/1.

References

1. R. C. McPhedran, A. B. Movchan & N. V. Movchan: Platonic crystals: Bloch bands, neutrality and defects, *Mechanics of Materials*, **41**, p.356-363, 2009.
2. M. Farhat, S. Guenneau & S. Enoch: High-directivity and confinement of flexural waves through ultra-refraction in thin perforated plates, *E*uropean Physics Letters, **91**, 54003.
3. D. Torrent, D. Mayou & J. Sánchez-Dehesa: Elastic analog of graphene: Dirac cones and edge states for flexural waves in thin plates, *Phys. Rev. B*, **87**, 115143, 2013.
4. R. C. McPhedran, A. B. Movchan, N. V. Movchan, M. Brun & M. Smith: "Parabolic" trapped modes and steered Dirac cones in platonic crystals, *Proc. R. Soc. Lond.* A, **471**, 2015.
5. A. B. Movchan, N. V. Movchan & R. C. McPhedran: Bloch-Floquet bending waves in perforated thin plates, *Proc. R. Soc. A*, **463**, p.2505-2518, 2007.
6. T. Antonakakis & R. V. Craster: High frequency asymptotics for micro-structured thin elastic plates and platonics, *Proc. R. Soc. Lond.* A, **468**, p.1408-1427, 2012.
7. D. V. Evans & R. Porter: Penetration of flexural waves through a periodically constrained thin elastic plate in *vacuo* and floating on water, *J. Eng. Maths.*, **58**, p.317-337, 2007.
8. S. G. Haslinger, A. B. Movchan, N. V. Movchan & R. C. McPhedran: Symmetry and resonant modes in platonic grating stacks, *Waves in Random and Complex Media*, **24**, p.126-148, 2014.
9. N. L. Hills & S. N. Karp: Semi-infinite diffraction gratings I, *Comm. Pure Appl. Math.*, **18**, p.203-233, 1965.
10. L. L. Foldy: The multiple scattering of waves I, General theory of isotropic scattering by randomly distributed scatterers, *Phys. Rev.*, **67**, p.107-119, 1945.
11. R. Zengerle: Light propagation in singly and doubly periodic waveguides, *J. Mod. Opt.*, **34**, p.1589-1617, 1987.

Texture determination from ultrasonic wave speeds for HCP and cubic materials

Bo Lan, Michael J.S. Lowe, Fionn P.E. Dunne
Imperial College London, Exhibition Road, London, UK, SW7 2AZ

Crystallographic texture in polycrystalline HCP and cubic materials, often developed during thermomechanical deformations, has profound effects on properties at the macroscopic or component level. Given the respective natures of current detection techniques, a non-destructive, three-dimensional bulk texture detection method for these materials is yet to be developed. This talk aims to achieve this goal through systematic studies on the relationship between ultrasonic wave velocity and texture.

The feasibility of such development is firstly reviewed via the combination of computational and experimental studies on exemplary HCP materials [1]. Numerical results obtained via a representative volume element (RVE) methodology reveal that the wave speed varies progressively and significantly with changing texture, and experimental ultrasound studies combined with EBSD characterisation demonstrate distinguished velocity profiles for samples with different textures. Thus the possibility of the development is proved by the combined results.

A novel convolution theorem is then presented, which couples the single crystal wave speed (the kernel function) with polycrystal orientation distribution function to give the resultant polycrystal wave speed function. Firstly developed on HCP [2] and then successfully extended to general anisotropic materials [3], the theorem expresses the three functions as harmonic expansions thus enabling the calculation of any one of them when the other two are known. Hence, the forward problem of determination of polycrystal wave speed is solved for all crystal systems with verifications on varying textures, showing near-perfect representation of the sensitivity of wave speed to texture as well as quantitative predictions of polycrystal wave speed. More importantly, the theorem also presents a solution to the long-standing inverse problem for HCP and cubic materials, with proof of principle established where groups of HCP and cubic textures are recovered solely from polycrystal wave velocities through the theorem, and the results show good agreements with the original textures. Therefore the theorem opens up the possibility of developing a powerful package for bulk texture measurement and wave propagation studies in HCP, cubic materials and beyond.

Further experimental validations of the proposed theoretical model are then conducted, with a series of samples made of typical HCP and cubic materials, including commercially pure (CP) Ti, copper, Ti-6Al-4V, examined by carefully designed experimental setup for the measurement of the angular variations of ultrasonic wave velocities. Texture information of the samples are extracted out from the measured velocities using the theoretical model, for the comparison and calibration against the set of information of the same samples measured independently by the well-established neutron diffraction technique. This part of the research is still an ongoing process.

References:

[1]. B Lan, MJS Lowe, FPE Dunne, "Experimental and computational studies of ultrasound wave propagation in hexagonal close packed polycrystals for texture direction", Acta Materialia, Vol. 63, pp. 107-122, 2014.

[2]. B Lan, MJS Lowe, FPE Dunne, "A spherical harmonic approach for the determination of HCP texture from ultrasound: a solution to the inverse problem", J Mech Phys Solids, Vol. 83, pp. 179-198, 2015.

[3]. B Lan, MJS Lowe, FPE Dunne, "A generalised spherical harmonic deconvolution to obtain texture from ultrasonic wave speed", J Mech Phys solids, Vol. 83, pp. 221-242, 2015.

An ultrasonic test bench for reproducing oceanic sound fluctuations

Gaultier Real, Dominique Habault, Xavier Cristol, Dominique Fattaccioli, Jean-Pierre Sessarego

Abstract Sound propagation in the ocean is subject to many phenomena of fluctuations. The most critical ones are the internal waves which occur frequently and induce fluctuations of the spatial distribution of the sound speed. The aim of this project was to develop and validate an experimental scaled model in a water tank in order to test the performance of sonar techniques in the case of sound fluctuations [1]. It was therefore essential to propose a reproducible experiment in a controlled environment. The protocol consists in transmitting an ultrasonic wave through a slab. The input face of the slab is flat, the output face is "randomly" rough in order to produce distortions of the received wavefront. The characteristics of the fluctuations induced on the acoustic signals are controlled by tuning the roughness parameter of the slab. A dimensional analysis has been developed in order to be able to compare results in the water tank and in an ocean perturbed by internal waves. Comparisons between the statistical moments of the sound pressure in both media are presented.

1 Introduction

The internal waves and the fluctuations they induce on the sound speed in ocean and therefore on sound propagation have been extensively studied theoretically and experimentally for several tens of years (see [2, 3] for example). The spatial variations of the sound speed are characterised by vertical and horizontal correlation lengths L_V and L_H of the order of several kms with $L_V \approx L_H/10$. The temporal variations are of the order of several hours. The aim of the project was to develop an experimental scaled model of these phenomena in order to test sonar techniques. Let us underline that the objective was not to reproduce exactly the fluctuations phenomena but rather to produce fluctuations qualitatively similar. The sound pressure fluctuations are often described with 3 propagation regimes : The unsaturated regime (leading to

G. Real and D.Habault
CNRS-LMA, CS40006, 13453 Marseille Cedex 13, France. e-mail: real,habault@lma.cnrs-mrs.fr

phase fluctuations of the sound pressure), the fully saturated regime (which can be described by uncorrelated eigenrays) and in-between the partially saturated regime. Two main parameters are used to characterise these regimes : The strength parameter Φ and the diffraction parameter Λ. These parameters and the correlation lengths of the sound pressure $L_{h,v}$ are used to link the experiment in the water tank and an experiment in the ocean.

2 The experiment in a water tank

Fluctuations of the sound pressure in the water tank have been obtained by placing a slab between a source and a receiver (see fig. 1). The input face of the slab ($y =$constant, on the source side) is flat. Its output face is characterised by a roughness parameter $y = \xi(x,z)$. This parameter is chosen as a normal Gaussian function of zero mean value and with standard deviation equal to ξ_0. A large number of slabs were designed and realised at the laboratory, each one corresponding to one realisation of ξ. The source emits an ultrasonic wave of frequency 2.25 MHz. The receiver is placed on a motorised rail in order to simulate measurements on vertical arrays. The distance between source and receiver varies from 250 to 450 mm. Statistical studies were carried out on the sound pressure measured at the receiver.

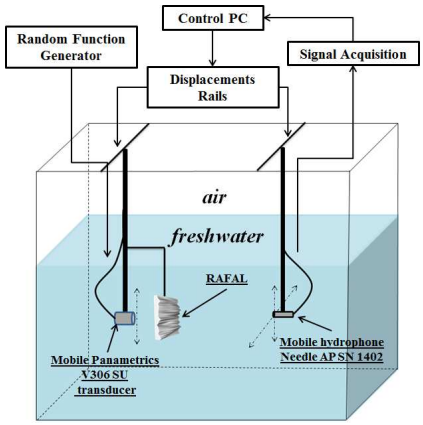

Fig.1 - Water tank experiment

In parallel, a dimensional analysis was conducted. The first step was to define and calculate equivalent parameters $\tilde{\Phi}$ and $\tilde{\Lambda}$ in the case of the slab. They depend on the characteristics of the experiment : mainly, roughness of the slab, frequency, distance source-receiver. The second step was to calculate an analytical approximation of the correlation lengths $\tilde{L}_{h,v}$ of the sound pressure in the case of the slab. Finally, the

characteristics of the experiment were tuned to obtain values of $\tilde{\Phi}$, $\tilde{\Lambda}$ and $\tilde{L}_{h,v}$ equal to those obtained for typical experiments of interest in an oceanic case.

3 The mutual coherence function

Figure 2 shows an example of comparison of the mutual coherence function (second-order moment of the sound pressure) versus the spacing distance between two positions of the receiver s on a vertical line. The spacing distance is related to the acoustic wavelength λ. The black curve (continuous line) corresponds to a simplified theory, the red circles are the measured values, the blue squares and the violet diamonds correspond to numerical simulations for the oceanic case and the slab case respectively.

The experiment has been validated on several configurations corresponding to the 3 propagation regimes. The next step is to test sonar techniques in the presence of fluctuations.

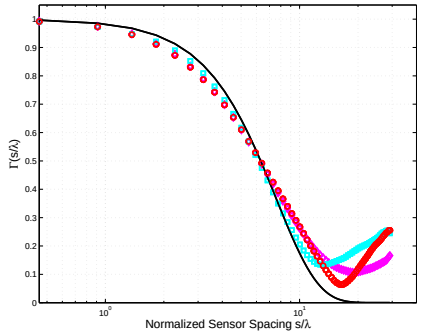

Fig.2 - Mutual coherence function of the sound pressure - Partially saturated regime

References

1. G.Real, An ultrasonic test bench for the degradation of sonar performance in a fluctuating ocean, *PhD thesis, Aix-Marseille University*, France, November 2015.
2. S.Flatté and F.Tappert, Calculation of the effect of internal waves on the ocean sound transmission *Jal of the Ac. Soc of Am.*, 58(6), p.1151-1158, 1975.
3. R.Dashen, S.Flatté, W.Munk, F.Zachariasen, Sound transmission through a fluctuating ocean *Cambridge University Press*, 2010.

Domain Decomposition Method for scattering problem in 3D elastic waveguides

Vahan Baronian, Anne-Sophie Bonnet-Ben Dhia, Sonia Fliss, Antoine Tonnoir

Abstract We consider the time-harmonic diffraction problem by an arbitrary localized perturbation in an infinite elastic waveguide. The Domain Decomposition Method is used to derive an original formulation which is well adapted for a numerical resolution. A coupling between a finite element representation in a bounded domain containing the perturbation, and a modal expansion in unbounded regular domains of the guide is achieved by introducing an overlap between the two domains. We will detail how this approach offers the possibility to derive iterative algorithms of resolution and leads to a complete efficient strategy of coupling.

1 Motivation

This work fits into the context of simulation of non destructive experiment by guided waves. One major issue is to dispose of an efficient numerical method to compute the interaction of guided waves with an arbitrary localized perturbation (cracks, inclusions, shape modification,...). In order to handle such range of defects, the finite element method is classically used to model the area containing the perturbations. The remaining question concerns the choice of the boundary condition that need to be imposed on the boundary of the computational domain to avoid spurious reflections and get an "efficient" method. Among the approaches used to bound the scattering domain, a hybrid method [1], involving a coupling between the finite element and the modal representations of the solution, has been proposed few years ago. Unfortunately, it gives rise to a small but partially dense linear system that

Vahan Baronian
CEA-List, Gif-sur-Yvette, France, e-mail: vahan.baronian@cea.fr

Anne-Sophie Bonnet-Bendhia and Sonia Fliss
POEMS (ENSTA Paristech, CNRS, INRIA, Universite Paris Sacaly), France, e-mail: Anne-Sophie.Bonnet-Bendhia@ensta-paristech.fr,Sonia.Fliss@ensta-paristech.fr

Antoine Tonnoir
INRIA,Universit Paris Saclay, France, e-mail: antoine.tonnoir@inria.fr

can induce prohibitive computational cost, especially for large 3D configurations. Moreover this method is limited for orthotropic medium. Our aim is to offer an improved release of the previous version, that will reduce the computational cost (due to the inversion) and overcome the anisotropic limitation. Therefore, a new class of hybrid FE/Modal boundary operator has been designed, where the matching between the two representations is done on two separated boundaries and is said "with overlap" by analogy with the domain decomposition methods. This approach which is suitable for an iterative resolution, has been already used in the case of acoustic waveguide [2] and recently extended to elastic waveguide [3].

2 The radiation problem, geometry and notations

We consider an infinite elastic waveguide supposed to be homogenous, outside a bounded region containing the defects. The total displacement field $\mathbf{u}$ has to satisfy the following equations of the radiation problem

$$\left|\begin{array}{l} \operatorname{div}\sigma(\mathbf{u})+\rho\omega^2\mathbf{u}=\mathbf{f} \quad \text{in } \Omega \\ \qquad\qquad \sigma(\mathbf{u}).\nu=0 \quad \text{on } \partial\Omega \end{array}\right. \tag{1}$$

where ω is the pulsation, ρ the density and $\mathbf{f}$ the source term. The medium is supposed to be anisotropic so that the stress tensor $\sigma(\mathbf{u})$ is mapped to the strain tensor $\varepsilon(\mathbf{u})$ by the generalized Hooke's law.

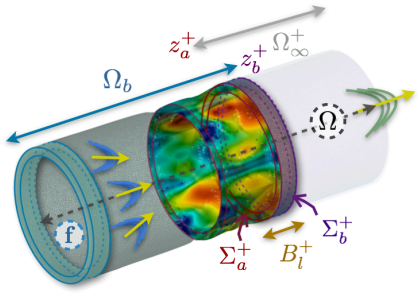

Fig. 1 Definition of the sub-domains used in the formulation associated to the radiation problem

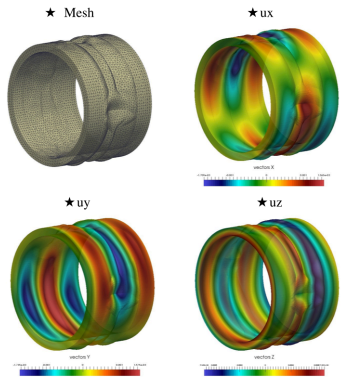

Fig. 2 Diffraction of an extensional mode by a corroded area in a pipe

In our domain decomposition approach, the infinite domain Ω is subdivided in two parts. The bounded domain $\Omega_b = \Omega \cap \{0 \le z \le z_b^+\}$ that contains the perturbation and the source $\mathbf{f}$, and the semi-infinite regular domain $\Omega_\infty = \Omega \cap \{\mathbb{R}^3, z \ge z_a^+\}$, where the radiated field can be expressed by using the modal expansion. Finally, the overlap $B_l^+ = \Omega_b \cap \Omega_\infty$, of size l, which is delimited by the boundaries $\Sigma_a^+(z = z_a^+)$ and $\Sigma_b^+(z = z_b^+)$, where an appropriate Transmission Condition (TC) will be imposed.

3 A Hybrid FE/Modal formulations with overlap

Taking advantage of the regularity of Ω_∞, a modal representation of the solution $\mathbf{u}$ is given, involving the elastic modes $\mathscr{U}_k^+$ and the unknown diffracted coefficients a_k^+. From the displacement field $\mathbf{u}_{|B_l^+}$ in B_l^+, the traces of the displacement $\mathbf{u}_{|\Sigma_a^+}$ and the stress $\sigma(\mathbf{u})_{|\Sigma_a^+}$ fields on Σ_a^+ can also be obtained. According to these data, the coefficients a_k^+ can be recovered as a function of $\mathbf{u}_{|B_l^+}$ by using two different relations on Σ_a^+, named (Y) and (O) in the following. Among the advantages offered by the "O" relation, the possibility to handle anisotropic material is also given.

$$\mathbf{u}(\mathbf{x}) = \sum_{k\geq 0} a_k^+(\mathbf{u}_{|B_l^+}) e^{i\beta_k(z-z_a^+)} \mathscr{U}_k^+(\mathbf{x_s}) \quad \text{for} \quad z \geq z_a^+ \tag{2}$$

The relation (2) allows us to build new hybrid FE/Modal operators $T^{+l}_{\ldots\to R}(\mathbf{u}_{|B_l^+})$ ("..." stands for "Y" or "O"), that will be used to express the missing TC on Σ_b^+. A so-called Robin TC is chosen: $TC(\star) = \sigma(\star).\nu + \alpha\star$, (such that $\Im(\alpha) > 0$) where α is a "tuning" parameter. Finally, a variational formulation is derived where the unknown is $\mathbf{u}$ in the bounded domain Ω_b.

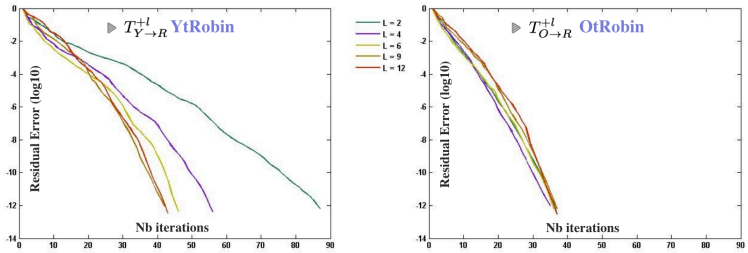

Fig. 3 Evolution of the residual error vs number of iterations for different sizes of overlap

Thanks to the overlap B_l^+, this formulation can be adapted in an iterative form and be solved using the GMRES algorithm. Figure [3] illustrates the influence of l on the convergence, for the operators $T^{+l}_{Y\to R}$ and $T^{+l}_{O\to R}$. A significant result is obtained using the $T^{+l}_{O\to R}$ operator, since the convergence is independent of l. Therefore the size of B_l^+ can be reduced to its minimum and leads to a complete efficient transmission condition.

References

1. V. Baronian, A.-S Bonnet-Ben Dhia and E. Luneville. Transparent boundary conditions for the harmonic diffraction problem in an elastic waveguide, *JCAM*,vol. 234(6), pp.1945-1952, 2010.
2. N. Gmati and N. Zrelli. Numerical study of some iterative solvers for acoustics in unbounded domains, *ARIMA*, vol. 4, pp.1-23, 2006.
3. V. Baronian, A.-S Bonnet-Ben Dhia, S. Fliss and A. Tonnoir., Iterative methods for scattering problems in unbounded anisotropic waveguides, *submitted in WaveMotion*, 2015.

Noise reduction in ultrasonic array imaging by the DORT method

Eduardo Lopez Villaverde, Sébastien Robert, Claire Prada

Abstract In the present work, the Synthetic Transmit Aperture (STA) algorithm is used to image flaws from corrupted signals recorded by a contact transducer array probe. In order to reduce the structural or electronic noise, as well as artifacts due to surface guided waves, the Decomposition of the Time Reversal Operator method is performed before calculating STA images in the time domain.

1 Introduction

The Synthetic Transmit Aperture (STA) imaging [1, 2], also called Total Focusing Method (TFM), is a delay-and-sum algorithm that provides optimized images in Non-Destructive Testing (NDT). However, this method leads to a poor Signal-to-Noise Ratio (SNR) in the case of noisy materials, such as coarse-grained steels of the nuclear industry. The highly heterogeneous structure of these materials yields a strong coherent noise that hides the defect echo and complicates its detection, even at relatively low frequencies. The detection is also difficult in homogeneous materials when they are characterized by a strong attenuation, such as plastic pipes made of polyethylene. The main attenuation effect is a dramatic increase of the incoherent electronic noise in STA imaging. In the present work, we propose to apply the Decomposition of the Time Reversal Operator (DORT is the French acronym) method in order to improve the detection in presence of coherent or incoherent noise in the data.

Eduardo Lopez Villaverde
CEA, LIST, Gif-sur-Yvette, F-91191, France, e-mail: eduardo.lopezvillaverde@cea.fr

Sebastien Robert
CEA, LIST, Gif-sur-Yvette, F-91191, France e-mail: sebastien.robert@cea.fr

Claire Prada
Institut Langevin, 1 rue Jussieu, 75238 Paris Cedex 05, France e-mail: claire.prada-julia@espci.fr

2 Noise filtering principle with the DORT method

The DORT method consists of a singular value decomposition of the full array transfer matrix $\hat{\mathbf{K}}(f)$ at each frequency [3]. In the ideal case of a point-like defect with a low-level noise, $\hat{\mathbf{K}}(f)$ can be expressed as the sum of the two matrices:

$$\hat{\mathbf{K}}(f) = \sigma_1(f)\mathbf{u}_1(f){\mathbf{v}_1}^{\dagger}(f) + \sum_{q=2}^{N} \sigma_q(f)\mathbf{u}_q(f){\mathbf{v}_q}^{\dagger}(f), \tag{1}$$

where $\sigma_q(f)$ is the q-th singular value, $\mathbf{u}_q(f)$ and $\mathbf{v}_q(f)$ are the received and transmitted singular vectors, respectively. The first term in Eq. (1) is the matrix that contains the spectral information of the defect, whereas the second term is a matrix associated with the noise.

In practice, for materials with higher noise, the singular value associated with the defect varies with the frequency. In order to track the index of this singular value, denoted $p(f)$, we consider the delay law that focuses on the defect $\boldsymbol{\tau}_{\text{ref}}$. Then, $p(f)$ is determined through the cross-correlation between the delay laws $\boldsymbol{\tau}_q(f)$, extracted from $\mathbf{v}_q(f)$, and $\boldsymbol{\tau}_{\text{ref}}$. After identification of $p(f)$, we redefine a new matrix:

$$\hat{\mathbf{K}}'(f) = \sigma_{p(f)}(f)\mathbf{u}_{p(f)}(f){\mathbf{v}_{p(f)}}^{\dagger}(f). \tag{2}$$

In the time domain, the associated full array matrix $\mathbf{K}'(t)$ contains only information about the defect [4]. The application of the STA algorithm to $\mathbf{K}'(t)$ provides an image with a reduced noise.

3 Imaging in coarse-grained steel: coherent noise filtering

In the case of a coarse-grained steel, the data contain coherent noise, which is due to the structure of the material. The singular value distribution of $\hat{\mathbf{K}}(f)$ for a hole at 40 mm depth in this sample is displayed in Fig 1(a). The significant singular value around 1.1 MHz characterizes the defect. The other significant values at 0.5 and 0.8 MHz, are associated with the cross-coupling and the Rayleigh waves, respectively. The dotted curve $\sigma_{p(f)}(f)$ is obtained by tracking the index $p(f)$. Figures 1(b) and 1(c) display the STA images calculated from $\mathbf{K}(t)$ and $\mathbf{K}'(t)$, respectively.

4 Imaging in high density polyethylene: incoherent noise filtering

The data recorded inspecting a high density polyethylene [see Fig. 2(a)] are corrupted by an incoherent electronic noise. Because of the strong attenuation in this material at 5 MHz, the echoes amplitudes get close to the electronic noise. First obtained results are shown in Figs. 2(b) and 2(c).

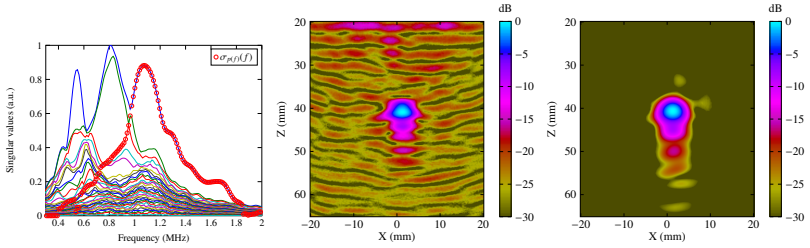

(a) (b) (c)

Fig. 1 (a) Singular values distribution of $\hat{\mathbf{K}}(f)$; (b) STA image; (c) STA with DORT filtering.

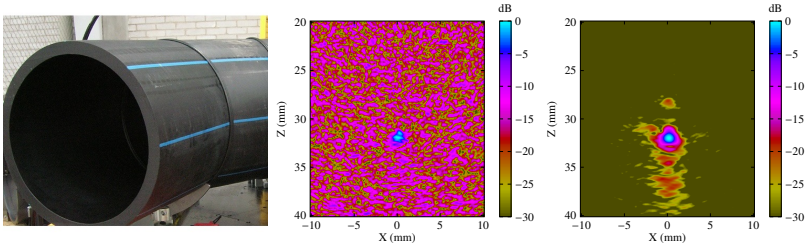

(a) (b) (c)

Fig. 2 (a) Polyethylene pipe with butt fusion joint; (b) STA image; (c) STA with DORT filtering.

5 Conclusion

The proposed approach selects correctly the spectral content associated with the defect. It is applicable to materials with structural noise, and attenuating materials. The STA image calculated from the filtered matrix present a significant reduction of the noise, either coherent or incoherent.

References

1. R. Y. Chiao, L. J. Thomas, S. D. Silverstein, : Sparse array imaging with spatially-encoded transmits, *Ultrasonics Symposium, 1997. Proceedings., 1997 IEEE*, V. 2, p. 1679-1682, 1997.
2. L. Le Jeune, S. Robert, E. Lopez Villaverde, C. Prada, : Plane Wave Imaging for ultrasonic non-destructive testing: Generalization to multimodal imaging, *Ultrasonics*, V. 64, 128-138, 2016.
3. C. Prada, S. Manneville, D. Spoliansky, M. Fink, : Decomposition of the time reversal operator: Detection and selective focusing on two scatterers, *Journal of the Acoustical Society of America*, V. 99, p. 2067-2076, 1996.
4. S. Bannouf, S. Robert, O. Casula, C. Prada, : Noise filtering in the total focusing method by decomposition of the time reversal operator and the virtual array approach, *American Institute of Physics Conference Series*, V. 1511, p. 857-864, 2013.

Experimental and numerical studies of the non-linear interaction between a longitudinal wave and contact interface

Abdelkrim Saidoun, Anissa Meziane, Mathieu Rénier, Christophe Bacon, Fan Zhang, Henri Walaszek

Abstract Early detection and characterization of damages in materials are important to control the durability and reliability of parts and materials in service. Although linear ultrasonic methods are sensitive for detecting and sizing open cracks, they failed to detect closed cracks. An alternative to linear ultrasonic methods is to use nonlinear methods, which have shown to be effective for this kind of defects. Nowadays, there are several nonlinear acoustic techniques used in non-destructive evaluation. In this study the harmonic generation technique is considered. Measurements were carried out on a real fatigue crack. Numerical analysis was performed using a 2D FE model describing the interaction between plane longitudinal acoustic wave and a contact interface. Different contact interface profile had been studied, showing specific evolution of the amplitude of the second harmonic as function of applied force.

Introduction The conventional techniques often rely on the linear property modifications of ultrasonic waves near a defect, such as reflection, attenuation, mode conversion etc, for crack detection. However, these linear features are reported to be not sensitive enough to detect closed cracks. On the other hand it has been noticed that in a great variety of structural materials, micro crack or closed cracks can produce very significant nonlinear effect. Using the nonlinear behavior of these defects, nonlinear ultrasonic techniques such as nonlinear resonance [1] higher harmonic generation [2] and frequency modulation [3] have been shown to be sensitive to micro cracks or closed cracks.

In this study the harmonic generation technique is considered. If the magnitude of the incident wave is sufficient to activate clapping between the tow interfaces of closed crack, higher harmonics appear in the frequency spectrum of transmitted and reflected waves. This effect, due to Contact Acoustic Nonlinearity (CAN) [4], is of increasing interest for characterization of closed cracks or imperfectly bonded interfaces [4,5].

Measurements were carried out on a CT specimen containing a fatigue crack using harmonic generation method. Numerical analysis was performed using a 2D FE model describing the linear propagation of a plane longitudinal acoustic wave

Abdelkrim Saidoun, Anissa Meziane, Mathieu Rénier, Christophe Bacon
I2M, 351 cours de la liberation, 33405 Talence, e-mail: Abdelkrim.saidoun@u-bordeaux.fr

Fan Zhang, Henri Walaszek

CETIM, 52 avenue Félix Louat, 60300 Senlis e-mail: fan.zhang@cetim.fr; henri.walaszek@cetim.fr

and its interaction with contact interface. In order to study the influence of the morphology of contact interface on the non-linear interaction with the acoustic wave, different interface morphologies were considered, showing specific evolution of the amplitude of the second harmonic as function of applied force.

Specimen and experimental set-up

Figure.1.a shows dimensions of the specimen used in our investigation, which is a compact tension (CT) specimen of steel material. This specimen was fatigue tested; it contains a crack of 44mm length.

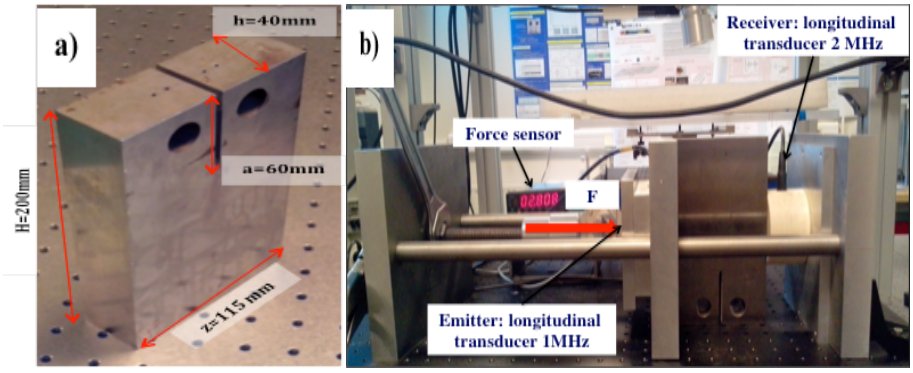

Figure. 1. *(a) Geometry of the specimen. (b) Experimental set-up.*

Figure.1.b shows the experimental set-up. A force [0.5,5] kN was applied to the specimen in order to close the crack. A 1MHz longitudinal transducer was used as transmitter; 2MHz longitudinal transducer was used as receiver to measure the first and second harmonic components in the transmitted wave. The transmitted signal was a 1MHz tone-burst of 10 cycles.

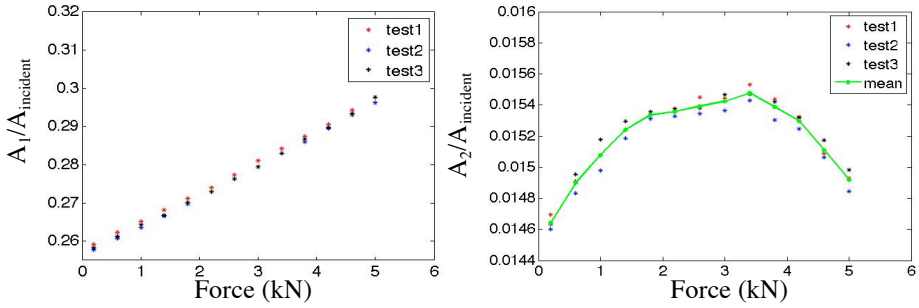

Figure. 2. *Experimental results (a) Evolution of transmission and (b) the amplitude of the second harmonic as function of the applied force for 3 different tests.*

Figure.2 shows the evolution of the transmission and the second harmonic as function of the applied force. The transmission of the wave increases with compression. The evolution of the ratio $A_2/A_{incident}$ shows an optimal value at F=3.4kN.

Compared to numerical result obtained by Hirose [6] for a smooth contact interface, it is noted that $A_2/A_{incident}$ is very low, and its evolution show some differences. A possible way to explain this differences is the geometrical effect at the interface (roughness, non perfect planarity…). Numerical analysis was conducted considering different morphologies of contact interfaces to investigate their influence on of the evolution of transmission and the second harmonic as function of the applied force.

Numerical Analysis

FE model using the software Plast2 [6] is used to study the interaction between an acoustic wave and contact interface between two identical homogeneous isotropic solids. First, the interfaces are considered planar, initially closed (figure.3.a) and initially opened (figure.3.b). In real contact interface, open and closed zones coexist on interface. In order to account of this, a first step consist in considering a "convex" surface on plane one (figure.3.c), and a "concave" surface on plane surface (figure.3.d). The unilateral contact law with Coulomb friction is applied to the interface. The contact algorithms are based on forward Lagrange multipliers. The friction coefficient μ= 0.3. Force is applied in the upper part of the two blocks. A plane wave of five cycles is generated on the top face of the solid. The central frequency of this pulse is 1MHz. The wavelength of the incident waves is thus λ= 6 mm. The incident stress is 1MPa.

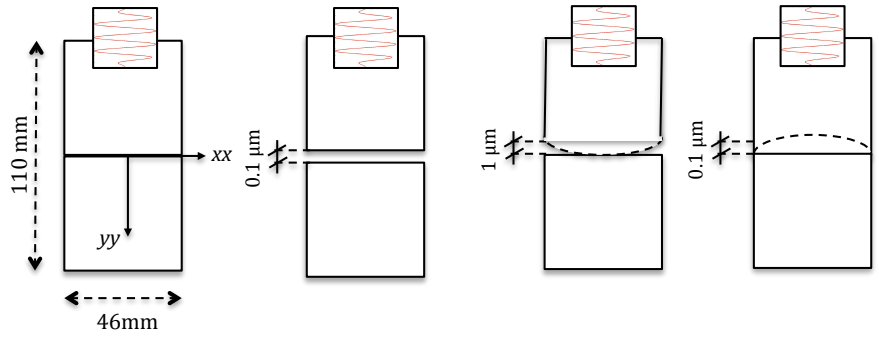

Figure. 3. *Model used for the interaction between the wave and the contact interface*. (a) Closed *planar interface. (b) Opened planar interfaces. (c) Concave interface. (d) Convex interface.*

Figure.4.a shows the evolution of the transmission and the second harmonic as function of the applied force in the case of closed planar interface. The transmission of the wave increases with compression up to F=7.5kN. The evolution of the ratio $A_2/A_{incident}$ have an optimal value at F=3kN.

In the case of the model with the convex interface, the evolution of $A_2 / A_{1transmitted}$ as a function of the applied force is close to the same evolution obtained experimentally. It shows two different regimes (figure.4.b), limited at F=3.25kN and an optimal value at F=5kN.

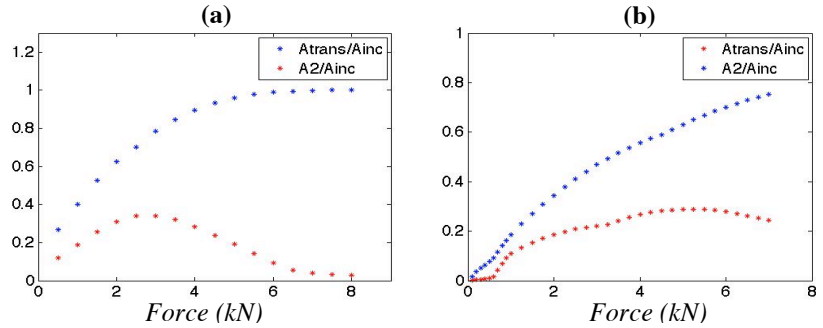

Figure. 4. *Evolution of transmission and the second harmonic as function of the applied force in the case on a) Planar interfaces. b) Convex interface.*

To explain the origin of the two observed regimes, an analysis of the harmonic sources at the interface were performed. It shows differences on distribution of these sources between the two regimes. Regime 1 corresponds to the second harmonic generation mainly on the edges of the interface, while the regime 2 corresponds to the second harmonic generation mainly at the center of the interface.

Conclusions

In this paper, the detection of closed cracks was investigated using the higher harmonic generation method. An evaluation of the second harmonic in the transmitted wave through a fatigue crack has been described. The evolution of $A_2/A_{incident}$ as function of the applied force shows an optimal value, which is characteristic of CAN. Numerical analysis showed that it shows that the geometry of the interface has an effect on the non-linear interaction between the acoustic wave and the contact interface.

References

1. K.E.-A. Van Den Abeele, J. Carmeliet, J. A. Ten Cate, and P. A. Johnson. Nonlinear elastic wave spectroscopy (news) techniques to discern material damage, part ii : Single-modenonlinear resonance acoustic spectroscopy. Research in Nondestructive Evaluation, 12 (1) :31–42, 2000.
2. O. Buck, W. L. Morris, and J. M. Richardson. Acoustic harmonic generation at unbounded interfaces and fatigue cracks. Applied Physics Letters, 33(5) :371 –373, sep 1978.
3. K. Van Den Abeele, P. A. Johnson, and A.Sutin. Nonlinear elastic wave spectroscopy (news) techniques to discern material damage, part i : Nonlinear wave modulation spectroscopy (nwms). Journal of Nondestructive Evaluation, 12 :17–30, 2000.
4. Solodov, I.Y., Krohn, N., Busse, G. (2002). CAN: An example of nonclassical acoustic nonlinearity in solids. Ultrasonics, vol. 40, no. 1-8, p. 621-625.
5. Dawei Yan, Bruce W. Drinkwater, and Simon A. Neild. Measurement of the ultrasonic nonlinearity of kissing bonds in adhesive joints. NDT & E International, 42(5) :459–466, 2009.
6. S. Hirose. 2d scattering by a crack with contact-boundary conditions. Wave Motion, 19 :37–49, 1993.

Mathematical Modelling in the Centre for Ultrasonic Engineering

Anthony MULHOLLAND

Abstract: The Centre for Ultrasonic Engineering is based in the University of Strathclyde which is in the heart of Glasgow in the UK (see www.strath.ac.uk/eee/research/cue/). Tony Mulholland has worked within this group for over 15 years and oversees the mathematical modelling activities. The group specialises in the development of new ultrasonic transducers and the application of ultrasonic transducers. It consists of more than 50 academics, researchers and technicians. The research interests are very broad and include nondestructive testing, medical imaging and therapies, ultrasound in biology, industrial process control, robotics and automation, and sonar. As such CUE is comprised of engineers, biologists, physicists, chemists, material scientists, and mathematicians. In this talk I will provide some insights into the role that mathematics plays in CUE and talk about our current work in both transducer design and in ultrasound applications. To illustrate the breadth of mathematics that one can use in this field I will discuss projects that have used notions from graph theory, renormalisation, the fractional Fourier transform, nonlinear elasticity, numerical analysis, functional analysis, scattering theory, inverse problems, and uncertainty quantification.

On crack detection in NDT using Love waves

Philippe Destuynder and Caroline Fabre

Abstract In a large number of problems, one has to deal with bimaterials. It is the case for instance for water pipes whose main body is in steel. A non corrosive coating is set on the inside of the pipe in order to avoid rust developments. It happens frequently that cracks start from the interface between the two materials and propagate along this interface. Even if classical ultrasonic inspections enable one to detect these cracks, the handling is long and costly. Therefore, the use of guided waves has been the object of many research in order to define a strategy for exploring long range pieces of structures order for reducing the exploration time, specially for long pipes. The goal of this presentation would be to suggest a criterion based on convective derivative of PDEs which could contain information on the existence and the position of such a crack. An optimal control method can then be used to fit the experimental data with the results derived from a simulation. Nevertheless, the criterion suggested is not perfect and there can exist cracks which are not seen by the criterion. In fact this depends on the frequencies used in the detection by ultrasonic waves. After a short presentation of the method and the criterion, the presentation focuses on the hidden cracks which can not be be detected for a particular given frequency.

1 Introduction

Following the ideas of many researchers in NDT, this presentation aims at giving a mathematical base of new methods introduced for instance in [1], [2], [3], [4], [5] and many others. Let us consider a rectangle -say R- as shown on figure 1. Let us assume that there is a crack parallel to the axis bearing the coordinate x_1. Its two

Philippe Destuynder
M2N-CNAM, 292, rue saint Martin, Paris 75003 e-mail: philippe.destuynder@cnam.fr

Caroline Fabre
LMO-UMR 8628 91405 Orsay cedex e-mail: caroline.fabre@u-psud.fr

extremities are at points A and B with abscissae a and b. Both sides of the segment AB are the crack lips and denoted by Γ_f. The wave equation that we consider is set on the open set $\Omega = \mathring{R} \setminus \Gamma_f$. On the boundary of the rectangle R -say Γ_1- the free edge condition is assumed. The unit normal outwards Ω and along its boundary is ν. Therefore the Helmholtz model is the following one, where c is the wave velocity (which is piecewise constant for a bimaterial) and u the transverse displacement to the plane containing Ω.

$$\begin{cases} -\omega^2 \hat{u} - div(c^2 \nabla \hat{u}) = \hat{f} \ \text{ in } \ \Omega, \\ \dfrac{\partial \hat{u}}{\partial \nu} = 0 \ \text{ on } \ \partial\Omega = \Gamma_f \cup \Gamma_1, \end{cases} \tag{1}$$

Using an eigenmodes expansion (the eigenvectors being denoted by $\{w_i\}$ and the eigenvalues by $\{\lambda_i\}$):

$$\hat{u}(\omega, x) = \sum_{i \geq 1} \frac{\int_\Omega \hat{f}(\omega, x) w_i(x)}{\lambda_i - \omega^2} w_i(x).$$

1.1 The solution of the wave model

The computation of the eigenmodes of the structure can be performed analytically when there is no crack, even (and mainly), for a bimaterial as shown on figure 1 with two different velocities. In this case, one obtains two families of eigenvectors.

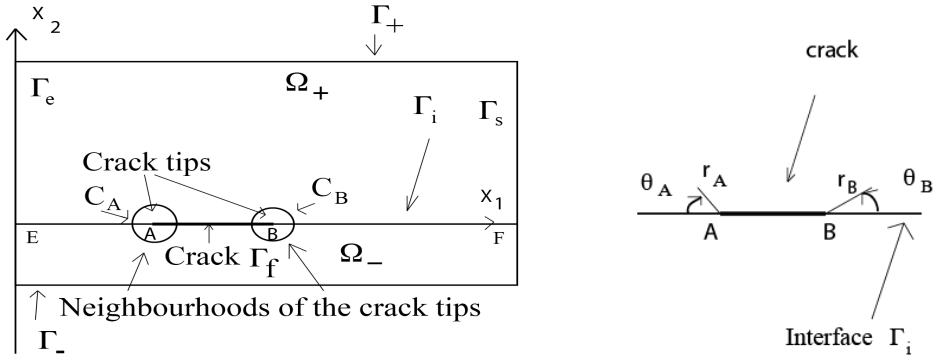

Fig. 1 The neighborhoods of the crack tips A and B. The local polar coordinates are respectively (r_A, θ_A) and (r_B, θ_B). The angles θ_A and θ_B are counted from the interface line Γ_i.

One contains the so-called Love stationnary waves which are mainly localized in the open set Ω_- if $c_- < c_+$ with an exponential decay inside Ω_+ from the separation line Γ_i. The second one contains global waves and their energy is developed in the whole domain Ω. But from a local analysis, it is also possible to describe the local behaviour of $\hat{u}$. More precisely, one has:

Theorem 1. *Let $\hat{u}$ be the solution of (1). One can write (c is discontinuous):*

$$\hat{u}(x,\omega) = \frac{K_A(\omega)}{c^2}\sqrt{r_A}\sin(\frac{\theta_A}{2}) + \frac{K_B(\omega)}{c^2}\sqrt{r_B}\sin(\frac{\theta_B}{2}) + \hat{u}^R(x,\omega), \tag{2}$$

where K_A (respectively K_B) is the stress intensity factor at point A (respectively B) and $\hat{u}^R$ is a smooth function. Furthermore, one has the following relationship which only requires boundary measurements and which is the criterion suggested for crack detection:

$$\int_{\Gamma_e \cup \Gamma_s} [-\omega^2\hat{u}^2 + c^2|\frac{\partial \hat{u}}{\partial x_2}|^2]\nu_1 - \int_\Omega q\frac{\partial \hat{u}}{\partial x_1} = \frac{\pi}{8}(\frac{1}{c_-^2} + \frac{1}{c_+^2})(K_B^2 - K_A^2). \tag{3}$$

The problem is now to detect among the Love waves (w_i^L, λ_i^L) which ones could be used for detecting a crack along the interface Γ_i. Furthermore, if the crack length is small enough, the eigenvectors w_i^L can be replaced by those computed without crack. This is the discussion which is carried out in the presentation. The point is to avoid the case $K_A = \pm K_B$ for which the crack is not visible by the criterion suggested.

2 Conclusion

The criterion introduced in theorem1 is an energetical quantity which enables to detect the existence of a crack in a bimaterial. This criterion can be used jointly with Love waves in order to detect a crak as soon as the frequencies are well chosen. But the position of the excitations should also be correctly adjusted.

References

1. G. Diot, A. Kouadri-David, L. Dubourg, J. Flifla, S. Guegan, E. Ragneau, Mesures de défauts par ultrasons laser dans des soudures d'alliage d'aluminium, Publications du CETIM, (2014).
2. A.Galvagni and P.Cawley, The reflection of guided waves from simple supports in pipes, *Journal of the Acoustical Society of America*, **(129)**, (2011), 1869-1880.
3. M.J.S. Lowe, Characteristics of the reflection of Lamb waves from defects in plates and pipes, *Review of Progress in Quantitative NDE*, DO Thompson and DE Chimenti (eds), Plenum Pr ess, New-York, **(17)**, (2002), 113-120.
4. P. M. Marty, *Modelling of ultrasonic guided wave field generated by piezoelectric transducers*, Thesis at Imperial college of science, technology and medecine, university of London, (2002), http://www3.imperial.ac.uk/pls/portallive/docs/1/50545711.PDF
5. R.Ribichini, F.Cegla, P.Nagy and P.Cawley, Study and comparison of different EMAT configurations for SH wave inspection, *IEEE Trans.UFFC*, **(58)**, (2011), 2571-2581.

Imaging defects in an acoustic waveguide using time-dependent surfacic data

Vahan Baronian, Laurent Bourgeois, Arnaud Recoquillay

Abstract In this lecture, we are interested in the possibility of using the Linear Sampling Method [1] in its modal form [2] to image defects in an acoustic waveguide using realistic scattering data, that is data coming from sources and receivers on the surface of the waveguide in the time domain.

1 The Linear Sampling Method: a modal formulation

We consider a two dimensional waveguide $\Omega = \Sigma \times \mathbb{R}$ of section $\Sigma = (0,h)$. We denote $\Gamma = \Gamma_0 \cup \Gamma_h$ the boundary of Ω, with $\Gamma_0 = \{0\} \times \mathbb{R}$ and $\Gamma_h = \{h\} \times \mathbb{R}$. Every solution u to the equation $\Delta u + k^2 u = 0$ in Ω with boundary condition $\partial_\nu u = 0$ on Γ, where ν is the outward unit normal, can be decomposed along the guided modes $u_n^\pm$, the sign depending on the way of propagation. A finite number N of those modes are propagating, the other ones are evanescent. We then consider a defect D inside the guide which lies between two sections $\Sigma_{\pm R} = \Sigma \times \{\pm R\}$, $R > 0$. The scattered field $u_n^{s\pm}$ associated to the incident mode $u_n^\pm$ is solution of the following forward problem:

$$\begin{cases} \Delta u_n^{s\pm} + k^2 u_n^{s\pm} = 0 \text{ in } \Omega, \\ \partial_\nu u_n^{s\pm} = 0 \quad \text{on } \Gamma, \\ u_n^{s\pm} = -u_n^\pm \quad \text{on } \partial D, \\ (RC) \end{cases}$$

Vahan Baronian
CEA Saclay e-mail: vahan.baronian@cea.fr

Laurent Bourgeois
ENSTA ParisTech, e-mail: laurent.bourgeois@ensta-paristech.fr

Arnaud Recoquillay
CEA Saclay e-mail: arnaud.recoquillay@cea.fr

with (RC) a radiation condition. The data in this case are the components of the scattering matrix $\mathscr{S}$, that is the modal projections on the two sections $\Sigma_{\pm R}$ of the scattered fields $u_n^{s\pm}$, the number of lines and columns being limited to $2N$. The Linear Sampling matrix $\mathscr{U}$ is obtained by multiplying $\mathscr{S}$ by a diagonal matrix depending only on the waveguide. Solving the system $\mathscr{U}h = m(z)$ for all points $z \in \Omega$, where m is a vector function given explicitly, provides an indicator function of the defect.

2 The case of surface solicitations and measurements

The method shown above needs data within the waveguide, which is not realistic. Let $(g_i^{\pm}(x))_{1\leq i\leq M} = (g(x-x_i^{\pm}))_{1\leq i\leq M}$ be a family of source functions for an even, compactly supported function g defined on $\mathbb{R}$ with $x_i^{\pm} = \pm(R+i\delta)$. The diffraction problem satisfied by the total field u is:

$$\begin{cases} \Delta u + k^2 u = 0 \text{ in } \Omega, \\ \partial_\nu u = g_i^{\pm} \text{ on } \Gamma_h \\ \partial_\nu u = 0 \text{ on } \Gamma_0, \\ u = 0 \text{ on } \partial D, \\ (RC). \end{cases} \tag{1}$$

The corresponding scattered field u^s is $u-u^i$, where u^i solves the same problem (1) as u without the boundary condition $u=0$ on ∂D. Our data are the components of a matrix $\mathscr{M}$ defined by the scattered fields measured at points $(h, x_j^{\pm})_{1\leq j\leq M}$ for all sources $(g_i^{\pm})_{1\leq i\leq M}$. The measurement matrix $\mathscr{M}$ is related to the LS matrix $\mathscr{U}$ by the relationship

$$\mathscr{M} = -\mathscr{R}\mathscr{U}\mathscr{E}^T, \tag{2}$$

where $\mathscr{R}$ and $\mathscr{E}$ are the reception and emission matrices. These matrices mainly depend on a Vandermonde matrix the conditioning of which strongly depends on the number $2M$ of sources and receivers and on the minimal distance δ between them. Inverting the system (2) enables us to compute $\mathscr{U}$ and then to apply the modal LSM as in section 1.

3 The case of data in the time domain

In the time domain, we consider the following problem:

$$\begin{cases} (1/c^2)\partial_{t^2} u - \Delta u = 0 \text{ in } \Omega \times (0,+\infty), \\ \partial_\nu u = g_i^{\pm}(x)\chi(t) \text{ on } \Gamma_h \times (0,+\infty), \\ \partial_\nu u = 0 \text{ on } \Gamma_0 \times (0,+\infty), \\ u = 0 \text{ on } \partial D \times (0,+\infty), \\ u = \partial_t u = 0 \text{ on } \Omega \times \{0\}. \end{cases}$$

The data consist of the corresponding scattered fields measured at the same points as before in the time interval $(0,+\infty)$. Here, $\chi(t)$ is suitably chosen so that the frequencies for which the group velocity vanishes are avoided. By applying a Fourier transform to our data, we recover the previous system (1) at a given pulsation ω, with $k = \omega/c$. We have now multi-frequency data, which allows us to image the defect with a better accuracy. In the figures below, $N = 12$ for the image using one frequency and it is varying between 8 and 12 for the one using multiple frequencies.

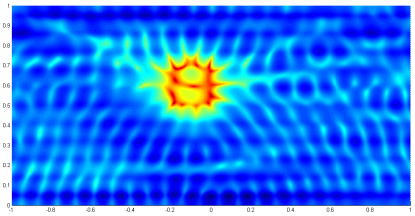

Fig. 1: Defect identification using one frequency

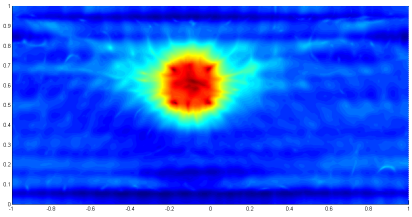

Fig. 2: Defect identification using multiple frequencies

4 Perspectives

Our next goal will be to adapt this method to an elastic waveguide, starting from the method developped in [3]. We then want to try it on experimental data.

Acknowledgements The artificial data were obtained thanks to the code Ondomatic developed at CEA by Alexandre Impériale.

References

1. D. Colton, A. Kirsch: A simple method for solving inverse scattering problems in the resonance region, *Inverse Problems*, V. 12, p. 383-393, 1996.
2. L. Bourgeois, E. Lunéville: The Linear Sampling Method in a wavegide: a modal formulation, *Inverse Problems*, V. 24, p. 15-18, 2008
3. L. Bourgeois, F. Le Louër, E. Lunéville: On the use of Lamb modes in the linear sampling method for elastic waveguides, *Inverse Problems*, V. 27, 2011

Apparent anisotropy of an adhesive layer induced by imperfect interfaces and evaluation of interfacial stiffness's.

Emmanuel Siryabe[1*], Mathieu Renier[1], Anissa Meziane[1], Jocelyne Galy[2], Michel Castaings[1]
[1]*I2M – UMR 5295 CNRS-Université Bordeaux, Talence Cedex, France*
[2]*IMP – UMR 5223 CNRS- INSA Lyon, Villeurbanne Cedex, France*

Introduction

The increasing use of adhesively bonded joints requires non-destructive evaluation methods to be developed, mostly for safety reasons. An adhesive joint can be divided into two sensitive zones that may cause mechanical failure: the body of the adhesive layer (cohesive zone) and the interphase between that adhesive and one of the substrate (adhesion zone). Weaknesses of these cohesive or adhesive zones can come, for example, from an incomplete curing of the adhesive or from inappropriate initial treatment of the substrate surface, respectively. The present research attempts to characterize mechanical properties, which are representative of the adhesive and cohesive states of adhesively bonded assemblies, using a through-transmission ultrasonic method. Inverse problems are then solved to infer the elastic moduli of the adhesive layer. The measurement of the transmitted acoustic field and estimation of elastic moduli are performed for several angles of incidence (θ) in a reduced experimental frequency bandwidth. For assemblies presenting a low level of adhesion, an apparent anisotropy of the adhesive layer moduli is observed, and thus reveals the presence of such defects. Furthermore, the interfacial stiffness coefficients are assessed.

1) Elastic moduli measurement principle

The elastic moduli measurement principle is presented in **Figure 1**. An incident plane wave, radiated in a water tank by a large transducer (E) is transmitted through a single or multi-layered plate with an incidence angle θ and then received by a second transducer (R). The measured spectrum $A_T(\theta, f)$ of the transmitted field is then computed for various incidence angles. In order to infer the elastic moduli of one of the layers, assuming that the elastic properties of the others layers are known, an optimization process, based on theoretical plane wave transmission coefficient, is proceed.

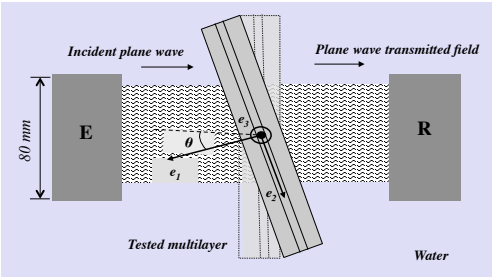

Figure 1: Measurement principle

* Corresponding author
I2M – UMR 5295 CNRS-Université Bordeaux, Talence Cedex, France
e-mail: emmanuel.siryabe@u-bordeaux.fr

The theoretical calculation of the transmitted acoustic field is based on the surface impedance matrices method [1]. The plane wave transmitted field includes all internal echoes inside the multilayer. Its modulus is given by:

$$\left|A^{Th}(\theta,f)\right| = \left|T^{Th}(\theta,f).A_I^{Exp}(f)\right| \quad (1)$$

where $A_I(f)$ is the measured spectrum $A_I(f)$, obtained by removing the multilayered plate.

The model takes into account the anisotropy and viscoelasticity of materials using the concept of heterogeneous plane waves and complex viscoelasticity moduli $C_{ij}=C_{ij}'+I.C_{ij}''$[2], with continuity of stress and displacements at different interfaces of the multilayer. The C_{ij}' and C_{ij}'' represent the anisotropic stiffness and the anisotropic viscoelasticity constants respectively. The elastic material properties of one of the layer are optimized using a combination of Newton-Raphson [3] and Simplex [4] algorithms. For a given plane of incidence (P_{12} in the present study) and using measurement obtained for various angles of incidence, the 4 moduli (C_{11}, C_{22}, C_{12} and C_{66}) can be measured. A calculation of the error is performed using the insensitivity matrix [5]. In this paper, a study of the influence of the interfacial properties on the measurement of an adhesive layer between two substrates is presented.

2) Results and discussion

In this purpose, six assemblies have been made. The substrates are all made of aluminium (2 mm thick). 3 of the assemblies are made of a 100% cured epoxy adhesive layer (1mm thick), while the epoxy is only 80% cured for the 3 others. The viscoelastic properties of those components have been measured on single plates using the time-of-flight method. The results are listed on *Table 1*. As expected, the measured elastic moduli show the isotropic of epoxy and aluminium samples. Lower values for the incompletely cured epoxy are obtained.

Table 1: *Elastic moduli measured on individual samples. The real parts are estimates at ±1% and the imaginary parts are measured equal to 3% of real parts.*

Medium	***ϱ (g/cm³)***	***Thickness (mm)***	***C_{11} (GPa)***	***C_{22} (GPa)***	***C_{66} (GPa)***	***C_{12} (GPa)***
Aluminium	*2.76*	*2*	*107*	*109*	*26*	*55*
Epoxy100%	*1.16*	*2.93*	*7.77*	*7.75*	*1.71*	*4.35*
Epoxy 80%	*1.16*	*2.96*	*7.56*	*7.52*	*1.53*	*4.25*

Then for each level of curing, three different surfaces treatments are applied before assembling, in order to vary the quality of adhesion: (1) degreasing, sandblasting and Silane treatment (reference sample with nominal adhesion properties, noted "DSSi"), (2) degreasing and sandblasting (intermediate adhesion level, "DS") and (3) degreasing only (very weak adhesion, "D").

a) Numerical study of the influence of interfacial properties on the determination of elastic moduli of an adhesive between two substrates

The procedure used is described as follow: First, we model the bonded assembly by 5 layers (2 Aluminium substrates and 1 epoxy layer with C_{ij} listed on *Table 1*) wherein the interphases are modelled by two interfaces thin isotropic layers thin (h^{int}= 1 μm), with elastic moduli $C_{ij}^{int} = \alpha . C_{ij,epoxy}$ where α is a parameter intro-

duced in order to model interfacial degradation ($\alpha \leq 1$). For nominal interfacial properties the values of interfacial elastic moduli (C_{11}^{int}, C_{66}^{int}) are equal to the elastic moduli of the adhesive layer.

Then, the simulation of the transmission of plane waves through the assembly is performed for different θ and the computed transmitted acoustics fields are then considered as experimental results for the previously introduced optimization process. The optimization process is then performed assuming perfect interfaces, providing the apparent elastic moduli C_{ij}^{app} of the adhesive layer.

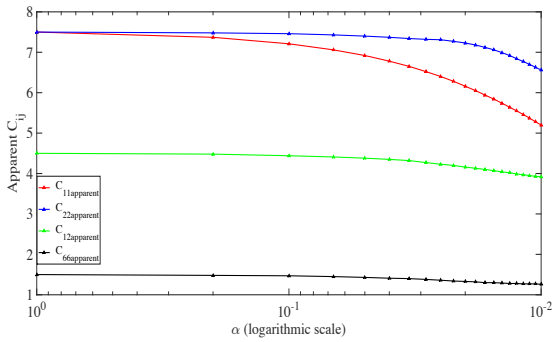

Figure 2: Evolution of elastic moduli of an epoxy (80% cured) between two substrates vs the state of degradation of interphases

The evolution of apparent elastic moduli of epoxy adhesive between two substrates, function of the parameter α, which indicate the state of degradation of interphases, is presented in **Figure 2.** We observe a decrease of all apparent elastic moduli of adhesive epoxy with an anisotropy when the interphases are degraded ($\alpha \approx 10^{-2}$), This apparent anisotropy is indicative of the presence of anomalies at interphases. The same evolution is obtained for the epoxy 100% cured.

b) Experimental validation

Measurements are done on the six samples models, manufactured and described in section 1. The experimental setup shown in **Figure 1** is used to determine the apparent elastic moduli of the adhesive layer between the two substrates. The transmitted spectra (in a 0,5 to 1,5 MHz frequency range) through the assembly are measured for different θ. The apparent elastic moduli measured for epoxy adhesives 80% cross-linked are shown in *Table 2***.** The experimental results confirm those previously obtained by simulations: all the apparent elastic moduli decrease when the interphases are slightly or severely degraded, with $C_{11}^{app} < C_{22}^{app}$, showing the apparent anisotropy confirmed by the fact that $C_{12}^{app} \neq C_{11}^{app} - 2C_{66}^{app}$. Thus, the surface treatment applied has therefore a significant influence on the determination of the elastic moduli. When the joint has nominal interphases, the adhesive layer's apparent elastic moduli located are close to those obtained on the individual adhesive sample. When the joint has slightly or severely degraded interphases, slight or strong apparent anisotropy on elastic moduli of adhesive layer is observed. The same results are obtained for epoxy adhesive 100% cross-linked. Conversely, keeping perfect interfacial properties, a weakness in the cohesive

properties (uncompleted cured state) of the adhesive layer is manifested by a decrease of all the adhesive layer apparent elastic moduli, with an apparent isotropy.

***Table 2**: Presentation of C_{ij}^{app} for the epoxy adhesives layers 80% cross-linked measured on the different bonded joints assemblies (Surface T: Surface Treatment and h: thicknesses). The error are evaluated from the insensitivity matrices*

Surface T	***h (mm)***	***C_{11}(GPa)***	***C_{22} (GPa)***	***C_{66}(GPa)***	***C_{12}(GPa)***
DSSi80	*1.09 ± 0.01*	*7.4±0.06*	*7.1 ± 0.5*	*1.7 ± 0.1*	*4.4 ± 0.2*
DS80	*0.78 ± 0.01*	*6.2 ± 0.2*	*6.8 ± 0.9*	*1.4 ± 0.2*	*4.1 ± 0.4*
D80	*0.75 ± 0.01*	*5.5 ± 0.1*	*6.8 ± 0.9*	*1.3 ± 0.2*	*3.9 ± 0.4*

c) Characterization of the interfacial properties

We focus in this section, on the evaluation of the interfacial stiffness ($k_L = C_{11}^{int}/h^{int}$ and $k_T = C_{66}^{int}/h^{int}$) representative of the state of adhesion for each surface treatment of substrates. The interfacial stiffness's are obtained from the measurements of the transmission coefficient for a given θ using least squares minimization algorithm [6], assuming now that the adhesive layer's C_{ij} correspond to the apparent ones measured on the reference DSSi samples (**Table 2**). The k_L is estimated at normal incidence ($\theta=0°$) and the k_T is obtained at oblique incidence ($\theta=15°$). For bonded joints made with epoxy adhesive 80% cured, **Table 3** presents the set of estimated interfacial stiffness values, which are representative of the adhesion state at the interfaces. The optimization results show that, significantly lower interfacial stiffness values are obtained when interphases are degraded. The transverse stiffness appears to decrease more than the longitudinal one. We can observe that, for the same state of the surfaces treatment of the substrates before assembling, whether the adhesive epoxy is 100% or 80% cross-linked, we get the same interfacial elastic moduli values (**Table 3**).

***Table 3**: Presentation of the interfacial stiffness values estimated for the six samples assembled with an epoxy adhesive partially and totally cross-linked (1PPa=10^{15} Pa).*

	DSSi100	***DS100***	***D100***	***DSSi80***	***DS80***	***D80***
k_L (PPa/m)	2.5	0.225	0.10	2.5	0.225	0.135
k_T (PPa/m)	1.6	0.04	0.025	1.6	0.03	0.02

Conclusion

The measurement of the adhesive layer apparent elastic moduli, for various incidence angles and without any isotropy assumption could provide an indication about the presence of interfacial weaknesses. Furthermore, if the adhesive layer's elastic moduli are known, an evaluation of the interfacial stiffness is possible. The results obtained show that, both the longitudinal and transverse interfacial stiffness are sensitive to the surface treatment of the substrates.

References:

1. B. Hosten, M. Castaings, Ultrasonics 41, 501-507, 2003.
2. B. Hosten, M. Castaings, J. Acoust. Soc. Am., 94(3), 1488–1495, 1993.
3. B. Hosten, M. Castaings, T. Kundu, Rev Progr Quantitative NDE, 17, 1117–1124, 1998.
4. MR. Karim, AK. Mal, Y. Bar-Cohen, J. Acoust. Soc. Am., 88 (1), 482–491, 1990.
5. S. Baudoin, B. Hosten, J. Acous. Soc. Am., 102 (6), 3450-3457, 1997
6. A. Lavrentyev, S. I. Rokhlin, J. Acoust. Soc. Am. 102, 3467–3477, 1997.

Design of acoustic beam shifters and related experiments

Rowley W.D., Parnell W.J., Abrahams I.D. and Voisey S.R.

Abstract In this talk we discuss the design process and paths to realisation of an acoustic metamaterial beam shifter. We will find that an anisotropic effective mass density tensor is required, and look at how this can be achieved by layered media in the homogenised limit. We discuss the challenges in realising such a material in both the cases of water and air surrounding the device.

1 Introduction

Transformation acoustics is a widely used technique, that provides the required material properties in order to achieve a given coordinate transform on a pressure field [1]. We consider a virtual isotropic space (x',y',z') and choose a coordinate mapping onto the physical space (x,y,z), that describes the desired action of the wave-manipulating device. We then apply this mapping and notice that Helmholtz' equation can be regained on the correct choice of a new effective mass density and bulk modulus.

In this talk we will introduce the technique of transformation acoustics as a way of finding the required material properties of a given wave-manipulating device. We

William D. Rowley
The University of Manchester, School of Mathematics, University of Manchester, Oxford Road, Manchester M13 9PL, e-mail: william.rowley-3@postgrad.manchester.ac.uk

William J. Parnell
The University of Manchester, School of Mathematics, University of Manchester, Oxford Road, Manchester M13 9PL e-mail: william.parnell@manchester.ac.uk

I. David Abrahams
The University of Manchester, School of Mathematics, University of Manchester, Oxford Road, Manchester M13 9PL e-mail: i.d.abrahams@manchester.ac.uk

S. Ruth Voisey
Dyson Ltd., Tetbury Hill, Malmesbury, Wiltshire, SN16 0RP e-mail: ruth.voisey@dyson.com

will apply this theory to the design of an acoustic beam shifter, a device that shifts incident sound pressure waves in space, [1].

In order to find the required material properties for a beam shifter we want to transform a region of the plane, $x' \in [0,a]$, as,

$$x = x', \qquad y = y' + f(x'), \qquad z = z'. \tag{1}$$

In the following we will fix the definition of $f(x) = bx/a$, this defines a linear shift of height b over the device thickness a. The Jacobian can be calculated to determine the required effective properties of the beam shifter. The Jacobian has unit determinant and so the bulk modulus of our beam shifter must be that of the background, that is the material in the undeformed region surrounding the device, the density must be anisotropic and is given by,

$$\rho_{eff}^{-1} = \begin{pmatrix} 1 & \frac{b}{a} & 0 \\ \frac{b}{a} & 1+\frac{b^2}{a^2} & 0 \\ 0 & 0 & 1 \end{pmatrix}. \tag{2}$$

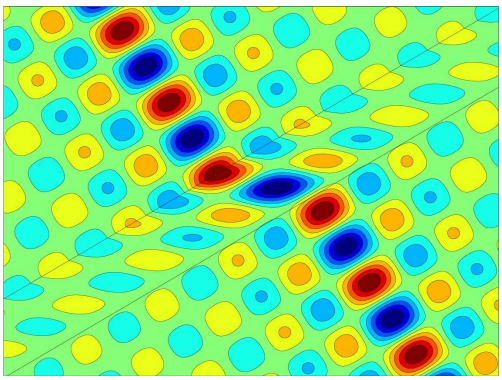

Fig. 1 Should we be able to realise these properties, an incident pressure field of arbitrary type will enter the material with perfect transmission and leave it again, directed as it was before entering, but at a new, shifted height. We focus on three such incident pressure fields: a plane wave, point source and Bessel beam [2], as shown here.

2 Realisation through layered media

In the homogenised limit an infinite periodic array of two layered fluids behaves as a homogeneous anisotropic material. We show that under certain circumstances with the correct choice of material layers this layered material can become a beam shifter. We will see that the direction of the material layering and the beam shift are not, in general, aligned.

We discuss the material properties required to construct a beam shifter from layered materials when the host phase is water. We see that it can be achieved by using

a layer of material with density less than that of water. We then consider the host phase to be air. Once again, in the case of layered materials we will need a material with lower density than air, which poses a challenge.

3 An imperfect impedance condition

In order to realise the beam shifter in a host phase of air, we attempt to sacrifice the perfect impedance condition in order to widen the range of possible materials. This is done by introducing a scale factor n to the required material properties. In this sense the properties we are aiming to achieve are no longer the properties required to shift a beam in air, but the properties required to shift a beam in a fictitious material that has the material properties of air scaled by a factor n. In this case we see that a layer with greater stiffness and density than that of the background can be utilised, these can then be selected in order to maximise the transmitted field.

4 Other roads to realisation

We consider alternative ways to realise the anisotropic mass density condition required to create a beam shifter. We still use a layered medium but allow the second material to be made of an infinite array of cylinders made of two different materials [3]. In the case of the layered media we could only tune the material properties of the additional layer and the volume fraction. Here, however we are able to tune the material properties of an arbitrary number of fibres with elliptical cross-section and their volume fraction[4]. We can then consider an even broader class of materials, where we can then alter the above parameters, the aspect ratios of ellipses and their relative alignment. This increase in degrees of freedom means that the effective materials that can be created in this way are much richer.

Acknowledgements This work was carried out at the University of Manchester and funded through a CASE award studentship awarded by the EPSRC and Dyson Ltd.

References

1. S.A. Cummer: Transformation Acoustics, *Acoustic Metamaterials*, Ch 8 , 197-216, 2013.
2. R.L. Nowack: A tale of two beams: an elementary overview of Gaussian beams and Bessel beams, *Studia Geophysica et Geodaetica*,V. 56, 2, 355-372, 2012.
3. D. Torrent, J. Sánchez-Dehesa, : Acoustic metamaterials for new two-dimensional sonic devices, *New Journal of Physics*, 9, 323, 2007.
4. W.J. Parnell, I.D. Abrahams, : Dynamic homogenization in periodic fibre reinforced media. Quasi-static limit for SH waves, *Wave Motion*, 43, 474-498, 2006.

Conformal mapping for the scattering by a rough surface

G. Favraud and V. Pagneux

Abstract We consider the scattering of an acoustic wave from a periodic rough surface. The method we propose is based on the use of a conformal mapping and of the multimodal admittance method. Showing very good convergence (exponential), the method allows us to solve scattering at high frequencies and also to find trapped surface wave propagating above the rough surface. A simple perturbation expansion, based on a small roughness approximation, is also developed.

1 The method: conformal mapping and multimodal approach

When a wave is incident on a rough surface it implies a complex scattering process [1, 2, 3] and efficient methods are still welcome to improve the understanding of this scattering (surface waves, high frequencies scattering, etc ...). In this work, we present a method [4] based both on conformal mapping and mutlimodal admittance method.

We consider the scattering of an incident plane wave by a rigid periodic rough boundary with Neumann boundary condition (the case of Dirichlet boundary condition might be treated as well). The boundary is represented by a curve $\mathscr{C}$ in the (X,Y) plane: it is 2π—periodic in the X direction (fig. 1(a)). The domain considered is the upper infinite half plane above this curve $\mathscr{C}$. In the harmonic regime ($e^{-i\omega t}$), the total field Φ satisfies the Helmholtz equation with rigid boundary condition:

$$\begin{cases} \Delta_{XY}\Phi + k^2\Phi = 0 \\ \nabla\Phi \cdot N = 0 \qquad on \qquad \mathscr{C}, \end{cases} \tag{1}$$

G. Favraud and V. Pagneux
Laboratoire d'Acoustique de l'Université du Maine (LAUM), UMR CNRS 6613, Avenue Olivier Messiaen, 72085 Le Mans Cedex 9, FRANCE., e-mail: vincent.pagneux@univ-lemans.fr

where k is the wavenumber and where Δ_{XY} and ∇ are the Laplacian and the gradient operators with respect to the (X,Y) variables, and N is the unit normal vector to $\mathscr{C}_{XY}$. We then consider the conformal mapping that maps the rough surface $\mathscr{C}$ to the

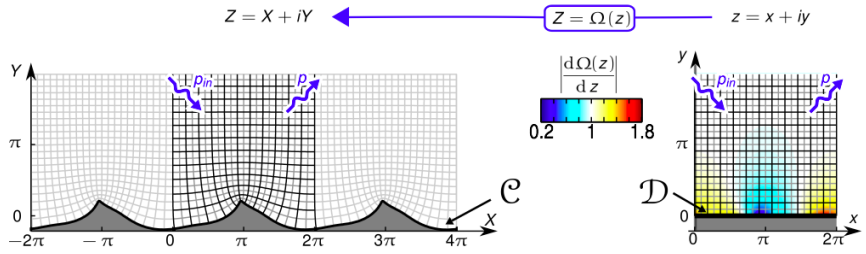

Fig. 1 (a) physical plane (X,Y) (b) computational plane (x,y). The mapping function Ω transforms the computational plane into the physical plane. The rough boundary $\mathscr{C}$ is mapped to the flat boundary $\mathscr{D}$. An index appears in the computational domain.

flat surface $\mathscr{D} = \{y = 0 \,|\, x \in [0,2\pi]\}$ (fig. 1(b)). The conformal mapping is defined by:

$$Z = \Omega(z), \tag{2}$$

where Ω is a periodic function of the form $\Omega(z) = z + f(e^{iz})$. We impose that $f(0) = 0$ in order that the mapping tends to the identity for $y \to \infty$ ($\mathrm{e}^{\mathrm{i}z} \to 0$). This is important since it allows to localize the effect of the mapping near the boundary at $y = 0$. The function Ω maps the *computational plane* (x,y), in which the problem will be solved [fig. 1(b)], to the *physical plane* (X,Y), in which the problem is initially stated [fig. 1(a)]. In the computational plane (x,y) the problem is now written as :

$$\begin{cases} \Delta_{xy}\Phi + k^2 n^2 \Phi = 0 \\ \frac{\partial}{\partial y}\Phi = 0 \qquad at \qquad y = 0 \end{cases} \tag{3}$$

where $n(x,y) = \left|\frac{\mathrm{d}Z}{\mathrm{d}z}\right|$. It appears that $n(x,y)$ acts as an equivalent spatially varying index. An important aspect of the conformal mapping is that, in the computational plane, the boundary condition becomes very simple.

To solve the scattering problem, Φ is now split into the sum of an incident field φ_{in} and of a scattered field φ ($\Phi = \varphi_{in} + \varphi$), where the incident field is supposed to be of the form of a plane wave in the physical plane ($\varphi_{in} = \mathrm{e}^{\mathrm{i}\alpha_0 X - \mathrm{i}\beta_0 Y}\sqrt{2\pi}$) with $\alpha_0^2 + \beta_0^2 = k^2$. Owing to the 2π—periodicity of the problem in the x direction, and to the form of the incident field, the scattered field is quasi-periodic in the x direction: $\varphi(x,y) = \varphi(x+2\pi,y)\mathrm{e}^{2\mathrm{i}\pi\alpha_0}$, and the problem can be solved on the semi-infinite vertical strip $[0,2\pi]\times[0,+\infty)$. The scattered field φ is decomposed as a Fourier series

$$\varphi(x,y) = \sum_{n=-\infty}^{+\infty} \varphi_n(y) g_n(x), \tag{4}$$

where $g_n(x) = e^{i\alpha_n x}/\sqrt{2\pi}$ with $\alpha_n = \alpha_0 + n$. This leads naturally to coupled mode equations along the axis y for the coefficients φ_n. These equations cannot be directly integrated numerically because of the presence of evanescent modes which are responsible for numerical instability. Therefore, we introduce the admittance matrix Y which can be seen as a matrix representation on the Fourier basis of the Dirichlet to Neumann operator. The equation governing the variation of the admittance matrix along y is a Riccati equation that has to be solved from the radiation condition. This is the principle of the multimodal method [5] that is used to solved the problem.

2 Some results: scattering and trapped surface waves

Typical results are shown in Figure 2. It has been verified that we have an exponentiel convergence with respect to the number N of Fourier components that is used in equation 4.

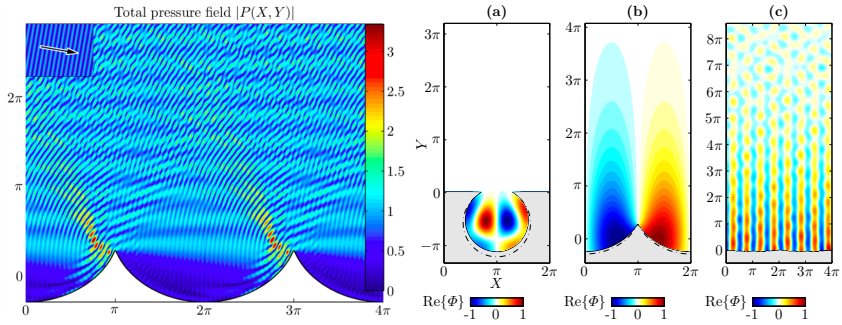

Fig. 2 Left: scattering by a rough surface. Right (a)-(c): different exemples of surface waves trapped by a rough surface

References

1. Beckmann P, Spizzichino A. 1968 *The Scattering of Electromagnetic Waves from Rough Surfaces*. New York: MacMillan.
2. Ogilvy J. 1991 *Theory of wave scattering from random rough surfaces*. Bristol: IOP Publishing.
3. Voronovich A. 1999 *Wave scattering from rough surfaces*. Berlin: Springer-Verlag
4. Favraud, G. and Pagneux, V. " Multimodal method and conformal mapping for the scattering by a rough surface." *Proc. Roy. Soc. Lond. A*, **471**(2175),. 20140782 (2015)
5. Pagneux V. "Multimodal admittance method in waveguides and singularity behavior at high frequencies", *J. Comp. Appl. Math.* **234**, 1834–1841 (2010)

A new scheme for the effective properties of complex composites

D. Joyce, W. J. Parnell, I. D. Abrahams

Abstract In this work a new, alternative method to model the effective macroscopic properties of periodic composite materials shall be outlined based on an integral equation form of Navier's equations. For ease of illustration the case of antiplane shear wave propagation through a fibre reinforced composite (FRC) will be the main case study. The main resulting advantage is a new explicit analytical formulae, valid at arbitrary volume fraction, in terms of parameters linked to specific physical phenomena (e.g. inclusion shape, lattice type).

1 Introduction and example geometry

The integral equation method (IEM), first outlined in [1] for the antiplane (SH) wave problem for fibre reinforced composites (FRCs - an example of which is depicted in Figure 1) at leading order with respect to both volume fraction ϕ and non-dimensional frequency ε, proved advantageous for its validity in non-dilute regimes and a solution structure where individual terms account for specific physical features such as fibre cross section and material properties. In contrast the method of asymptotic homogenisation (MAH) lacks this structure, instead hiding the detail within the cell problem and the numerical schemes used to solve it. This work extends the IEM beyond the leading order in ϕ.

Consider identical, unidirectional isotropic fibres, of arbitrary cross-section embedded periodically in an isotropic host material. The lattice geometry is restricted such that the effective material appears to be, at most, orthotropic on the macroscale. SH waves are then polarised in the x_3 direction and propagate in the x_1x_2 plane.

D. Joyce e-mail: duncan.joyce@postgrad.manchester.ac.uk, · W. J. Parnell e-mail: name@email.address, · I. D. Abrahams e-mail: i.d.abrahams@manchester.ac.uk
School of Mathematics, The University of Manchester, Manchester M13 9PL, UK

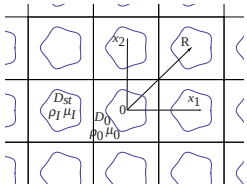

Fig. 1: Example FRC geometry with square periodic cell and associated notation. Material properties are μ (shear modulus) and ρ (density). I subscripts referring to inclusions and 0 the host.

In this regime ϕ is defined as being per unit span in the x_3 direction and non-dimensional frequency is $\varepsilon = qk_0$, q being the characteristic length scale of the periodic cell and k_0 the wavenumber of the host.

2 Methodology and results

Scaling lengthsclaes on k_0, and taking $\rho_I = \rho_0$, the governing equations for the displacement in the x_3 direction, $w(\boldsymbol{x})$, can be written in integral form as

$$w(\boldsymbol{x}) = -(1-m)\sum_{\substack{s,t=-\infty \\ s,t\in\mathbb{Z}}}^{\infty}\left(\int_{D_{st}} \nabla_y w(\boldsymbol{y})\cdot\nabla_y G(\boldsymbol{y}-\boldsymbol{x})d\boldsymbol{y}\right),$$

where $\boldsymbol{x} = (x_1, x_2)$, $G(\boldsymbol{x})$ is the Green's function, $m = \mu_I/\mu_0$ and D_{st} is the domain of the (s,t)th fibre. Further manipulation yields a system in displacement gradient moments $W_{ij}^{(k)}(\boldsymbol{r})$ (weighted averages of w over the fibre cross-section) and shape factor terms $\mathscr{A}_{ij}^{(k)}(\boldsymbol{r})$. The latter are related to the Hill tensor [2]. By seeking plane wave solutions (propagating in the x_1 direction) $W_{ij}^{(k)}(\boldsymbol{r}) = \hat{W}_{ij}^{k}\exp(i\gamma_1 r_1)$, with $\gamma_1^2 = 1/\mu_1^*$, one ultimately obtains a linear system of the form

$$\begin{bmatrix} \mathscr{G}_{00}(\gamma_1) & \mathscr{G}_{01} & \mathscr{G}_{02} & \cdots \\ \mathscr{G}_{10}(\gamma_1) & \mathscr{G}_{11} & \cdots & \\ \vdots & \vdots & \ddots & \\ \mathscr{H}_{00} & \mathscr{H}_{01} & \cdots & \\ \mathscr{H}_{10} & \cdots & & \\ \vdots & \ddots & & \end{bmatrix} \begin{Bmatrix} \hat{W}_{00}^{(1)} \\ \hat{W}_{10}^{(1)} \\ \vdots \\ \hat{W}_{00}^{(2)} \\ \vdots \end{Bmatrix} = \mathbf{0}.$$

In general all matrix coefficients $\mathscr{G}_{ij}$, $\mathscr{H}_{ij}$, depend on ϕ and lattice sums (terms involving the singular behaviour of derivatives of $G(\boldsymbol{x})$).

Asymptotic expansions in ϕ are then posed for $\hat{W}_{ij}^{(k)}$ in powers of ϕ, and

$$\frac{1}{(\mu_1^{*-1}-1)} = \frac{a_{-1}}{\phi} + a_0 + a_1\phi + \ldots \tag{1}$$

Retaining powers of ϕ successively generates a hierarchy of equations, each permitting evaluation of a_j and thus μ_1^* via (1). μ_2^* is obtained by rotating the material by $\pi/2$ and using the same wave type.

In the case of fibres of circular cross-section in a square lattice

$$\mu_j^* = \frac{1-(1-m)\phi/(1+m) - C_{4j}^2\phi^4 - C_{8j}^2\phi^8 + \ldots}{1+(1-m)\phi/(1+m) - C_{4j}^2\phi^4 - C_{8j}^2\phi^8 + \ldots} \tag{2}$$

where C_{4j} and C_{8j} depend upon m and the fourth and eight order lattice sums respectively. Figure 2 illustrates how the accuracy of the IEM increases as successive powers of ϕ are added and how it compares with the MAH result.

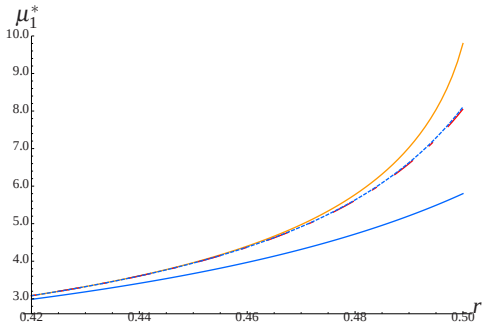

Fig. 2: Plot of effective longitudinal shear modulus versus radius of circular cylindrical graphite fibres in epoxy for square lattice, m =18.75, using the MAH (top) and the integral equation method (IEM) model at order ϕ (bottom), ϕ^4 (dot dashed), ϕ^8 (dashed)

Other cross sections shall be examined in the presentation, as well as an outline of how the scheme extends to the acoustic wave problem for composites with three dimensional inclusions. The scheme can also be adapted to thermal conductivity and many other applications.

Acknowledgements D. Joyce is grateful to Thales Underwater Systems Ltd and EPSRC for funding via a CASE studentship.

References

1. W. J. Parnell, I. D. Abrahams: An new integral equation approach to elastodynamic homogenization, *Proc. R. Soc. A*, V 464, p. 1461-1482, 2008.
2. W. J. Parnell, : The Hill and Eshelby tensors for ellipsoidal inhomogeneities in the Newtonian potential problem and linear elastostatics, *J. Elasticity*, arXiv:1507.07165.

Acoustic inverse scattering using topological derivatives

Cédric Bellis, Marc Bonnet, Fioralba Cakoni

Abstract Originally formulated in the context of topology optimization, the concept of topological derivative has also proved effective as a qualitative inversion tool for wave-based identification of finite-sized objects. This approach remains however largely based on a heuristic interpretation of the topological derivative, whereas most other qualitative approaches to inverse scattering are backed by a mathematical justification. As an effort towards bridging this gap, this study focuses on a topological derivative approach applied to the L^2-norm of the misfit between far-field measurements. Either an inhomogeneous medium or a finite number of point-like scatterers are considered, using either the Born approximation or a full scattering model. Topological derivative-based imaging functionals are analyzed using a suitable factorization of the far-field operator, for each of the considered cases, in order to characterize their behavior and assess their ability to reconstruct the unknown scatterer(s). Results include the justification of the usual sign heuristic underpinning the method for (i) the Born approximation and (ii) full-scattering models limited to moderately strong scatterers. Semi-analytical and numerical examples are presented. Within the chosen framework, the topological derivative approach is finally discussed and compared to other well-known qualitative methods.

1 Inverse scattering by an inhomogeneous medium

The illumination by an incident wave u_i of a given trial obstacle $D_\star$, characterized by an assumed contrast $q_\star$ such that $1+q_\star > 0$ in $D_\star$ and $\overline{D}_\star = \mathrm{supp}(q_\star)$, generates the corresponding acoustic scattered far-field pattern $v_\star^\infty$. Therefore, in order to quantify the discrepancy between $D_\star$ and an obstacle D to be identified, one may introduce

Cédric Bellis
Laboratory of Mechanics and Acoustics, CNRS, Marseille, France, e-mail: bellis@lma.cnrs-mrs.fr

Marc Bonnet
POems, CNRS-INRIA-ENSTA, Palaiseau, France

Fioralba Cakoni
Department of Mathematics, Rutgers University, Piscataway, USA

the following type of least-squares cost functional $\mathscr{J}$ evaluating the misfit between some scattered far-field measurements $v^\infty_{\rm obs}$ and their trial counterpart $v^\infty_\star$:

$$\mathscr{J}(D_\star, q_\star) := \int_{\mathbb{S}} \frac{1}{2} |v^\infty_\star(\hat{x}) - v^\infty_{\rm obs}(\hat{x})|^2 \, \mathrm{d}S_{\hat{x}}. \tag{1}$$

One further assumes that the data $v_{\rm obs}$ featured in (1) consists of noise-free measurements on the unit sphere $\mathbb{S}$ of the acoustic field scattered by D. The above functional assumes data from just one incident wave; multiple data may then be taken into account via finite sums or continuous superposition of functionals, as required.

If the incident field is chosen as a plane wave propagating in the direction $\theta \in \mathbb{S}$, i.e. $u_i = h(\cdot, \theta)$ with $h(x,\theta) = e^{\mathrm{i}kx\cdot\theta}$ for all $x \in \mathbb{R}^d$, the corresponding far-field pattern v^∞ is denoted $A(\cdot,\theta)$. Then, if D is illuminated instead by a continuous superposition of plane waves, i.e. u_i is a Herglotz wave with density $g \in L^2(\mathbb{S})$:

$$u_i(x) = \int_{\mathbb{S}} h(x,\theta) g(\theta) \, \mathrm{d}S_\theta = Hg(x) \quad x \in \mathbb{R}^d, \tag{2}$$

the corresponding far-field pattern v^∞ is expressed in terms of the far-field operator $F : L^2(\mathbb{S}) \to L^2(\mathbb{S})$ with kernel A:

$$v^\infty(\hat{x}) = Fg(\hat{x}), \qquad Fg(\hat{x}) := \int_{\mathbb{S}} A(\hat{x},\theta) g(\theta) \, \mathrm{d}S_\theta. \tag{3}$$

Sampling methods are commonly investigated under the assumption that full-aperture far-field data be available for *all* possible directions of incident plane waves, i.e. that the kernel $A(\hat{x},\theta)$ of F be known from measurements for all $\hat{x},\theta \in \mathbb{S}$, as this data uniquely determines the refraction index q. The cost functional of type (1) corresponding to this situation, denoted alternatively as $\mathscr{J}_{\mathbb{S}}$, is defined by

$$\mathscr{J}_{\mathbb{S}}(D_\star, q_\star) := \int_{\mathbb{S}} \int_{\mathbb{S}} \frac{1}{2} |A_\star(\hat{x},\theta) - A(\hat{x},\theta)|^2 \, \mathrm{d}S_{\hat{x}} \, \mathrm{d}S_\theta, \tag{4}$$

The case of a single incident wave of Herglotz type of the form $u_i = Hg$ for some $g \in L^2(\mathbb{S})$, is also of interest, especially when g is selected on the basis of the full experimental information $A(\hat{x},\theta)$. The corresponding cost functional (1), denoted by $\mathscr{J}[g]$ to emphasize its dependence on the Herglotz density g, is defined by

$$\mathscr{J}[g](D_\star, q_\star) := \int_{\mathbb{S}} \frac{1}{2} |Fg(\hat{x}) - F_\star g(\hat{x})|^2 \, \mathrm{d}S_{\hat{x}}. \tag{5}$$

This study is mainly focused on studying the topological derivative of the cost functionals $\mathscr{J}_{\mathbb{S}}$ and $\mathscr{J}[g]$ as means for the qualitative reconstruction of D.

2 Topological derivative of L^2 cost functionals

For a given *sampling* point $z \in \mathbb{R}^d$, let the trial obstacle be endowed with a uniform contrast $q_\star$ and geometrically defined by $D_\star = D_z^\varepsilon := z + \varepsilon\mathscr{D}$, where $\mathscr{D} \subset \mathbb{R}^d$ is a fixed open set containing the origin and with volume measure $|\mathscr{D}|$. The *topological derivative* $\mathscr{T}(z)$ of $\mathscr{J}$ at z is defined through the asymptotic expansion of $\mathscr{J}$ as $\mathscr{J}(D_z^\varepsilon, q_\star) \underset{\varepsilon\to 0}{=} \mathscr{J}(\emptyset) + \eta(\varepsilon)\mathscr{T}(z) + o(\|v^\infty_{\varepsilon,z}\|_{L^2(\mathbb{S})})$ where $v^\infty_{\varepsilon,z}$ is the far-field pattern arising from the scattering of u_i by D_z^ε, $\eta(\varepsilon)$ defines the leading asymptotic behavior of $\mathscr{J}$ as $\varepsilon \to 0$ and $\mathscr{J}(\emptyset)$ is the value of $\mathscr{J}$ in the absence of any trial obstacle.

The topological derivatives associated with the cost functionals (4) and (5) can be recast as follows in terms of the far-field operator F associated with the unknown scatterer (D, q):

$$\mathscr{T}[g](z) = -|\mathscr{D}|k^2 q_\star \mathrm{Re}\left[(g, \Phi_z^\infty)_{L^2(\mathbb{S})} (\Phi_z^\infty, Fg)_{L^2(\mathbb{S})}\right], \tag{6a}$$

$$\mathscr{T}_{\mathbb{S}}(z) = -|\mathscr{D}|k^2 q_\star \mathrm{Re}\left[\left(\Phi_z^\infty, F\Phi_z^\infty\right)_{L^2(\mathbb{S})}\right]. \tag{6b}$$

The value $\mathscr{T}(z)$ quantifies the sensitivity of the featured cost functional $\mathscr{J}$ to the perturbation of the reference medium induced by the nucleation at $z \in \mathbb{R}^d$ of an infinitesimal obstacle with contrast $q_\star$. It is then natural to consider $z \mapsto \mathscr{T}(z)$ as a potential obstacle indicator function, as was previously done on several occasions (see e.g. Fig. 1). The heuristic underlying this usage is as follows: if $q_\star$ is of the same sign than q, then the sought object D (or the set thereof) is expected to be located at the sampling points z at which $\mathscr{T}$ attains its most pronounced *negative* values, i.e. at which the introduction of a sufficiently small scatterer with a contrast of the same sign than that of D induces the most pronounced decrease of $\mathscr{J}$. Note that no smallness requirement for D is made in this approach, which is referred to hereinafter as the *sign heuristic* of the topological derivative. Up to now, this sign heuristic lacks rigorous justification but is supported by many numerical experiments.

Based on formulations such as (6a) and (6b), this study aims at investigating the validity of such heuristic and determining conditions under which it has a mathematical justification, in the limited framework of the identification of obstacles characterized by refraction index perturbations using far-field data.

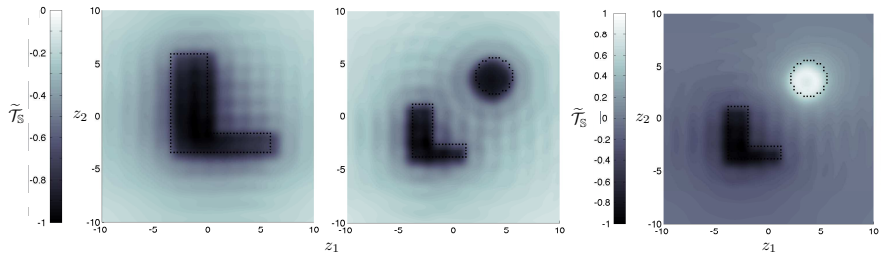

Fig. 1 Identification of two scatterers using topological derivatives.

Fourth order energy-preserving locally implicit discretization for linear wave equations

Juliette Chabassier and Sébastien Imperiale

Abstract Time domain simulation of realistic highly heterogeneous media or strongly refined geometries can be a computational challenge when using explicit schemes because they impose a time step restriction that can be extremely penalizing. In this work, we present fourth order locally implicit schemes. The domain of interest is decomposed into several regions where different (explicit or implicit) fourth order time discretization are used. Whilst implicit schemes tolerate the use of larger time steps, they can induce greater numerical dispersion. Fourth order accuracy reduces this lack of precision, and makes this family of schemes attractive compared to other approaches as local time stepping.

1 Continuous system

We want to solve for time $t > 0$, the system (closed with Neumann homogeneous boundary conditions):

$$\begin{cases} \partial_t^2 u_0 - \nabla \cdot c^2(\mathbf{x}) \nabla u_0 = s_0 \text{ in } \Omega_0, & c^2(\mathbf{x}) \nabla u_0 \cdot \mathbf{n}_0 = \lambda \quad \text{on } \Gamma, & \text{(1a)} \\ \partial_t^2 u_1 - \nabla \cdot c^2(\mathbf{x}) \nabla u_1 = s_1 \text{ in } \Omega_1, & c^2(\mathbf{x}) \nabla u_1 \cdot \mathbf{n}_1 = -\lambda \quad \text{on } \Gamma, & \text{(1b)} \\ u_0 = u_1 \quad \text{on } \Gamma & & \text{(1c)} \end{cases}$$

in a domain Ω composed by disjoint sets $\Omega = \Omega_0 \cup \Omega_1$ separated by $\Gamma = \overline{\Omega_0} \cap \overline{\Omega_1}$. s_0 and s_1 are given source terms, and $c(\mathbf{x}) > c_0 > 0$ is the inhomogeneous velocity of the waves. Any solution to (1) satisfies the energy identity $\frac{d\mathscr{E}_{01}}{dt} = \int_{\Omega_0} s_0 \, \partial_t u_0 + \int_{\Omega_1} s_1 \, \partial_t u_1$, where :

Juliette Chabassier
Magique 3D team, Inria Bordeaux Sud Ouest, e-mail: juliette.chabassier@inria.fr

Sébastien Imperiale
Inria, University Paris Saclay, e-mail: sebastien.imperiale@inria.fr

$$\mathscr{E}_{01} = \frac{1}{2}\|\partial_t u_0\|^2_{L^2(\Omega_0)} + \frac{1}{2}\|\partial_t u_1\|^2_{L^2(\Omega_1)} + \frac{1}{2}\|c\nabla u_0\|^2_{L^2(\Omega_0)} + \frac{1}{2}\|c\nabla u_1\|^2_{L^2(\Omega_1)} \quad (2)$$

2 Semi discrete system

We consider spatial meshes of Ω_0 and Ω_1 upon which are based finite dimensional finite element spaces: $\mathscr{V}_{h,0} \subset H^1(\Omega_0)$, $\mathscr{V}_{h,1} \subset H^1(\Omega_1)$ and $\Gamma_h \subset H^{-1/2}(\Gamma)$. One have leeway in the choice of $(\mathscr{V}_{h,0}, \mathscr{V}_{h,1})$ after which Γ_h must be chosen so that an inf-sup type condition is satisfied, see [4, 3, 1]. $(\widetilde{U}_{h,0}, \widetilde{U}_{h,1}, \widetilde{\Lambda}_h)$ is the solution of:

$$\begin{cases} d_t^2 M_{h,0}\widetilde{U}_{h,0} + K_{h,0}\widetilde{U}_{h,0} - {}^tC_{h,0}\widetilde{\Lambda}_h = M_{h,0}\widetilde{S}_{h,0} & (3a)\\ d_t^2 M_{h,1}\widetilde{U}_{h,1} + K_{h,1}\widetilde{U}_{h,1} + {}^tC_{h,1}\widetilde{\Lambda}_h = M_{h,1}\widetilde{S}_{h,1} & (3b)\\ C_{h,0}\,\widetilde{U}_{h,0} = C_{h,1}\,\widetilde{U}_{h,1} & (3c) \end{cases}$$

A semi discrete energy identity can be obtained, which satisfies

$$\frac{d\mathscr{E}_{01,h}}{dt} = M_{h,0}\widetilde{S}_{h,0}\cdot d_t\widetilde{U}_{h,0} + M_{h,1}\widetilde{S}_{h,1}\cdot d_t\widetilde{U}_{h,1}, \quad \text{where}$$

$$\mathscr{E}_{01,h} = \frac{1}{2}\|d_t\widetilde{U}_{h,0}\|^2_{M_{h,0}} + \frac{1}{2}\|d_t\widetilde{U}_{h,1}\|^2_{M_{h,1}} + \frac{1}{2}\|\widetilde{U}_{h,0}\|^2_{K_{h,0}} + \frac{1}{2}\|\widetilde{U}_{h,1}\|^2_{K_{h,1}} \quad (4)$$

where $\|X\|^2_M = MX\cdot X$ for any nonnegative matrix M. In the following, I_h will denote the identity matrix.

3 Discrete system

The proposed numerical discretization is based on the following definitions:

$$D^2_{\Delta t}U^n_h := \left(U^{n+1}_h - 2U^n_h + U^{n-1}_h\right)/\Delta t^2, \qquad \{U_h\}^n_\theta := \theta\, U^{n+1}_h + (1-2\theta)U^n_h + \theta\, U^{n-1}_h$$

The consistency analysis of the fourth order family of schemes [2] applied to each equation of system (3) instigates the following scheme:

$$\begin{cases} M_{h,0}D^2_{\Delta t}U^n_{h,0} + K_{h,0}\{U_{h,0}\}^n_{\theta_0} - {}^tC_{h,0}\Pi^n_h = M_{h,0}\,S^n_{h,0} + \Delta t^2\alpha_0 K_{h,0}M^{-1}_{h,0}\left[-K_{h,0}\{U_{h,0}\}^n_{\varphi_0} + {}^tC_{h,0}\Pi^n_h\right]\\ M_{h,1}D^2_{\Delta t}U^n_{h,1} + K_{h,1}\{U_{h,1}\}^n_{\theta_1} + {}^tC_{h,1}\Pi^n_h = M_{h,1}\,S^n_{h,1} + \Delta t^2\alpha_1 K_{h,1}M^{-1}_{h,1}\left[-K_{h,1}\{U_{h,1}\}^n_{\varphi_1} - {}^tC_{h,1}\Pi^n_h\right]\\ C_{h,0}\,\frac{U^{n+1}_{h,0}-U^{n-1}_{h,0}}{2\Delta t} - C_{h,1}\,\frac{U^{n+1}_{h,1}-U^{n-1}_{h,1}}{2\Delta t} = 0 \end{cases} \quad (5)$$

where $\alpha_i = \theta_i - 1/12$. Any solution to (5) satisfies the energy identity:

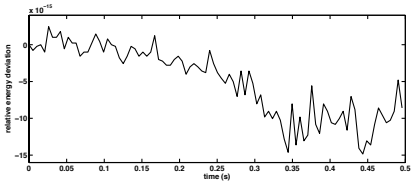

(a) Relative energy deviation for a 1D case: the energy is preserved up to machine precision.

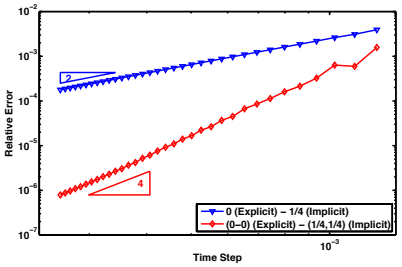

(b) Relative L2 error with the analytical solution as the time step tends to zero.

Fig. 1 Numerical illustrations in 1D.

$$\frac{\mathscr{E}^{n+1/2}_{01,4,h}-\mathscr{E}^{n-1/2}_{01,4,h}}{\Delta t}=\widetilde{I}^{-1}_{h,0}M_{h,0}S^n_{h,0}\cdot\frac{U^{n+1}_{h,0}-U^{n-1}_{h,0}}{2\Delta t}+\widetilde{I}^{-1}_{h,1}M_{h,1}S^n_{h,1}\cdot\frac{U^{n+1}_{h,1}-U^{n-1}_{h,1}}{2\Delta t},$$

where the discrete energy reads

$$\mathscr{E}^{n+1/2}_{01,4,h}=\frac{1}{2}\left\|\frac{U^{n+1}_{h,0}-U^{n}_{h,0}}{\Delta t}\right\|^2_{\widehat{M}_{h,0}}+\frac{1}{2}\left\|\frac{U^{n+1}_{h,1}-U^{n}_{h,1}}{\Delta t}\right\|^2_{\widehat{M}_{h,1}}+\frac{1}{2}\left\|\frac{U^{n+1}_{h,0}+U^{n}_{h,0}}{2}\right\|^2_{K_{h,0}}+\frac{1}{2}\left\|\frac{U^{n+1}_{h,1}+U^{n}_{h,1}}{2}\right\|^2_{K_{h,1}}$$

where the modified mass matrices $\widehat{M}_{h,i}$ are defined by $\widehat{M}_{h,i}=\widetilde{I}^{-1}_{h,i}\,\widetilde{M}_{h,i}$ where $\widetilde{I}_{h,i}=I_{h,i}+\Delta t^2\left(\theta_i-\frac{1}{12}\right)K_{h,i}M^{-1}_{h,i}$ and $\widetilde{M}_{h,i}=M_{h,i}+\Delta t^2\left(\theta_i-\frac{1}{4}\right)K_{h,i}+\Delta t^4\left(\theta_i-\frac{1}{12}\right)\left(\varphi_i-\frac{1}{4}\right)K_{h,i}M^{-1}_{h,i}K_{h,i}$. The positivity of the energy can be proven under standard CFL condition that depend on the parameters (θ_i,φ_i). Despite the non standard form of this energy, stability in $L2$-norm can be proved vie non standard estimates. Fig 1(b) shows that the coupling of second order implicit and explicit schemes only provides second order accuracy (as expected), while our scheme provides fourth order accuracy. Numerical illustrations in 2D as well as details about stability and consistency of scheme (5) will be presented.

References

1. E. Becache, P. Joly, J. Rodríguez, Space-time mesh refinement for elastodynamics. Numerical results, *CMAME,* vol. 194 (2-5), pp 355–366, 2005.
2. J. Chabassier, S. Imperiale. *JCAM*, vol. 245, pp 194–212, 2012.
3. G. Derveaux, P. Joly, J. Rodriguez Effective computational methods for wave propagation. Chap 13 : Space time mesh refinement methods, *Chapman and Hall/CRC*, 2008.
4. Y. Maday, C. Mavriplis, A. T. Patera, Nonconforming mortar element methods - Application to spectral discretizations in Domain decomposition methods, *SIAM Philadelphia*, pp 392–418, 1989.

Prestressed Nonlinear modes of a N degree-of-freedom system undergoing a purely elastic impact law

Stephane JUNCA, Mathias LEGRAND

Abstract Prestressed nonsmooth analysis is investigated for a linear system with perfect elastic impact. Comparisons and differences with the non stressed case are explored.

1 Equations and results

Nonlinear modes are used to find invariant manifold in the framework of nonsmooth analysis. Nonlinear modes appear to be considered as periodic solutions in the pre-stressed case and not simply continuation of linear modes. We consider a discrete N degree-of-freedom (dof) system:

$$\begin{cases} \mathbf{M}\ddot{\mathbf{u}} + \mathbf{K}\mathbf{u} = \begin{bmatrix} 0 \\ \vdots \\ 0 \\ R(t) \end{bmatrix}, \\ u_N(t) \leq \mathbf{g}, \\ R(t) \leq 0, \\ (u_2(t) - \mathbf{g})\, R(t) = 0. \end{cases} \tag{1}$$

where $\mathbf{M}, \mathbf{K}, \mathbf{u}, \dot{\mathbf{u}}$ and $\ddot{\mathbf{u}}$ represent the mass matrix, stiffness matrix, displacement, velocity and acceleration. The quantity $\mathbf{g}$ is the distance between the equilibrium position of mass N and the rigid wall. $R(t)$ is the reaction force of the wall on mass

Stéphane JUNCA
Laboratoire de Mathématiques J.A. Dieudonné and Team COFFEE INRIA, Université de Nice Sophia Antipolis Nice, France e-mail: junca@unice.fr

Mathias LEGRAND
Department of Mechanical Engineering McGill University
Montréal, Québec, Canada

N at the wall when impact (or grazing) occurs. The non stressed case $\mathbf{g} > 0$ was studied in [5] and presented at the last GDR conference in Gregynog (Wales). We present the prestressed case $\mathbf{g} \leq 0$. Two very different cases appears

1. $\mathbf{g} < 0$,
2. $\mathbf{g} = 0$.

In the first case, all solutions of the system are nonlinear (with impacts). The nonlinear spectrum is continuous but not issued from the linear invariant manifolds. In the second case, grazing stressed case $\mathbf{g} = 0$, the spectrum becomes discrete but not associated with the linear spectrum (of the system without impact). Structures of these invarint manifolds are presented.

References

1. Vincent ACARY, Bernard BROGLIATO: Numerical methods for nonsmooth dynamical systems. Applications in mechanics and electronics. it Lecture Notes in Applied and Computational Mechanics 35. Berlin: Springer. xxi, 525 p., 2008.
2. Patrick BALLARD: The Dynamics of Discrete Mechanical Systems with Perfect Unilateral Constraints, *Arch. Rational Mech. Anal.* 154 199274,2000.
3. Jrme BASTIEN, Frdric BERNARDIN, Claude-Henri LAMARQUE: Systmes dynamiques discrets non rguliers dterministes ou stochastiques, Applications aux modles avec frottement ou impact,*Collection Mcanique, Hermes Science Publications/Lavoisier, Paris,* 532 pp. (2012).
4. Sokly HENG: Nonlinear normal modes, private report with supervisors Stéphane JUNCA and Mathias LEGRAND, McGill University, November, 2013.
5. Denis LAXALDE, Mathias LEGRAND: Nonlinear modal analysis of mechanical systems with frictionless contact interfaces. *Comput. Mech.* 47, No. 4, 469-478, 2011.
6. Stéphane JUNCA, Mathias LEGRAND: Prestressed Nonlinear modes of a N degree-of-freedom system undergoing a purely elastic impact law, preprint, 2016.
7. Mathias LEGRAND, Stéphane JUNCA, Sokly HENG: Nonsmooth modal analysis of a N degree-of-freedom system with a purely elastic impact law, preprint, hal-01185980, 2015.
8. Madeleine PASCAL: Dynamics and stability of a 2 dof oscillator with an elastic stop, *Journal of Computational and Nonlinear Dynamics*, 2006.
9. Michelle SCHATZMAN: *A class of nonlinear differential equations of second order in time*, *Nonlinear Anal.* 2 , no. 3, 355373, 1978.
10. Anders THORIN, Mathias LEGRAND, Stéphane JUNCA: Nonsmooth modal analysis: investigation of a 2-dof spring-mass system subject to an elastic impact law, Proceedings of IDETC/CIE 2015, August 2-5, Boston, Massachusetts, USA, 2015.

Wave propagation in nonlinear elastic solids with slow dynamics

B. Lombard, N. Favrie, C. Payan

Abstract Various solid media exhibit time-dependent physical properties. For instance, the elastic modulus of damaged media (such as concrete) decreases when an increasing excitation is applied, and then recovers gradually its original value when the sollicitation is stopped. These relaxation phenomena are investigated here, both theoretically and numerically.

1 Introduction

Vibrational experiments in rocks or concrete reveal that two different dynamics coexist [2, 3]. First, a fast elastic dynamics occurs with a time scale ruled by the frequency of the excitation. Second, a slow dynamics governs the relaxation of the elastic modulus. Here, a "soft-ratchet" model [4] is preferred to the phenomenological Preisach-Mayergoyz model commonly used. The softening/recovering is related to the concentration of defects that evolves dynamically with the stress. This relaxation mechanisms is coupled to nonlinear elasticity and viscoelasticity. The reader is refered to [1] for technical details.

In section 2, we introduce the physical model and its basic features: evolution of defects, nonlinear elasticity, and attenuation. The evolution equations are written as a first-order system of partial differential equations. In section 3, the numerical method is introduced, based on a splitting strategy. In section 4, numerical experiments show that the experimental observations performed by Dynamic Acousto-Elastic Testing (DAET) are qualitatively recovered.

Bruno Lombard
Laboratoire de Mécanique et d'Acoustique, UPR 7051 CNRS, 4 impasse Nicolas Tesla, 13453 Marseille, France, e-mail: lombard@lma.cnrs-mrs.fr

Nicolas Favrie
IUSTI, Aix-Marseille Université, UMR CNRS 7343, 5 rue E. Fermi, 13453 Marseille, France e-mail: nicolas.favrie@univ-amu.fr

Cédric Payan
Laboratoire de Mécanique et d'Acoustique, UPR 7051 CNRS, 4 impasse Nicolas Tesla, 13453 Marseille, France, e-mail: cedric.payan@univ-amu.fr

2 Physical modeling

In 1D, the constitutive law relating the stress σ and the strain ε is the nonlinear Landau's model:

$$\sigma = E\,\varepsilon\left(1-\beta\,\varepsilon-\delta\,\varepsilon^2\right), \tag{1}$$

where E is the Young's modulus, β and δ are the quadratic and cubic coefficients. To reproduce the slow dynamics, E is assumed to evolve with a time-dependent concentration of defects g

$$E = \left(1-\frac{g}{g_{cr}}\right)E^+, \qquad 0 \leq g \leq g_{cr} \leq 1. \tag{2}$$

At rest the concentration of defects g_σ increases monotonically with the applied stress σ. For this purpose, a possible law is

$$g_\sigma = \frac{g_{cr}}{2}\left(1+\tanh\left(\frac{\sigma-\sigma_c}{\overline{\sigma}}\right)\right). \tag{3}$$

Out of equilibrium, the real concentration of defects relax towards the static value, with different time scales:

$$\frac{dg}{dt} = \begin{cases} -f_r\,(g-g_\sigma) & \text{if } g > g_\sigma, \\ -f_d\,(g-g_\sigma) & \text{if } g < g_\sigma \end{cases}, \tag{4}$$

where the restoration frequency f_r and the destruction frequency f_d satisfy $f_r \ll f_d$.

Based on the hypothesis of small perturbations, the conservation of momentum and the relaxation equation (4), the evolution equations write as a non-homogeneous first-order system of evolution equations:

$$\frac{\partial}{\partial t}\mathbf{U}+\frac{\partial}{\partial x}\mathbf{f}(\mathbf{U}) = \mathbf{R}(\mathbf{U})+\mathbf{S}. \tag{5}$$

3 Numerical modeling

For computational efficiency, the full system (5) is split into two parts: a hyperbolic step and a relaxation step

$$\begin{cases} \dfrac{\partial}{\partial t}\mathbf{U}+\dfrac{\partial}{\partial x}\mathbf{f}(\mathbf{U}) = \mathbf{0}, \\ \dfrac{\partial}{\partial t}\mathbf{U} = \mathbf{R}(\mathbf{U})+\mathbf{S}, \end{cases} \tag{6}$$

which are solved alternatively with adequate time steps. The hyperbolic step is solved by a conservative scheme (TVD)

$$\mathbf{U}_i^{n+1} = \mathbf{U}_i^n - \frac{\Delta t}{\Delta x}\left(\mathbf{F}_{i+1/2} - \mathbf{F}_{i-1/2}\right), \tag{7}$$

where Δx is the fixed space mesh, Δt is the variable time step, and $\mathbf{F}_{i\pm1/2}$ is the numerical flux function. The relaxation step is solved by a implicit trapezoidal method. The global algorithm is second-order accurate and is stable under the CFL condition $\Delta t = \frac{\alpha \Delta x}{c_{\max}}$, with $\alpha \leq 1$ and $c_{\max}$ is the greatest eigenvalue of the Jacobian matrix $\frac{\partial \mathbf{f}}{\partial \mathbf{U}}$.

4 Numerical experiments

Wave propagation is simulated on a 0.5 m long bar with physical properties of concrete. A punctual source on one edge generates waves up to $t = 0.1$ s. The elastic modulus $M(t) = \rho\, c^2$ is recorded at the middle of the bar. As shown in the left part of figure 4, it decreases, reaches a plateau, and then recovers gradually its original value. The evolution of $M - \varepsilon$ for increasing forcing amplitudes shows hysteretic and softening behaviors (right part of figure 4). It reproduces qualitatively the main features observed experimentally.

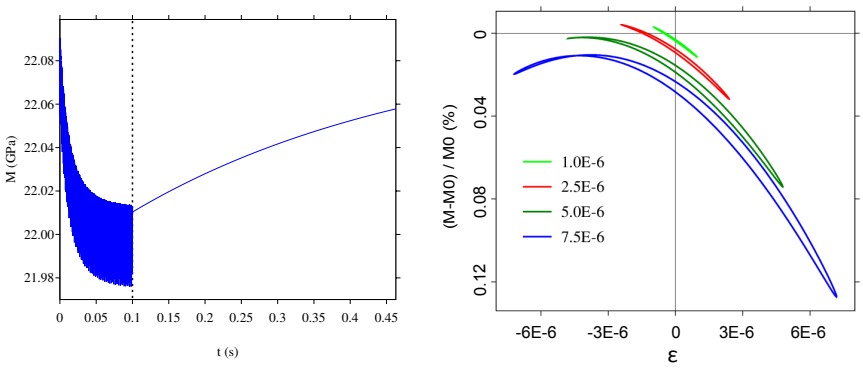

Fig. 1 Left: time evolution of the elastic modulus $M(t)$; the vertical dotted line refers to the extinction of the source. Right: relative evolution of M in terms of ε, for various forcing amplitudes.

References

1. N. Favrie, B. Lombard, C. Payan: Fast and slow dynamics in a nonlinear elastic bar excited by longitudinal vibrations, *W*ave Motion, 56, 221-238, 2015.
2. R. A. Guyer, P. A. Johnson: Nonlinear mesoscopic elasticity, evidence for a new class of materials, *P*hysics Today, 52, 30-35, 1999.
3. J. A. Ten Cate, T. J. Shankland: Slow dynamics in the nonlinear elastic response of Berea sandstone, *G*eophys. Res. Lett., 23, 3019-3022, 1996.
4. O. O. Vakhnenko, V. O. Vakhnenko, T. J. Shankland: Soft-ratchet modeling of end-point memory in the nonlinear resonant response of sedimentary rocks, *P*hysical Review B71, 174103, 2005.

Asymmetric Acoustic Propagation of Wave Packets Via the Self-Demodulation Effect

Thibaut Devaux, Vincent Tournat, Olivier Richoux and Vincent Pagneux

Abstract This article presents the experimental characterization of nonreciprocal elastic wave transmission in a single-mode elastic waveguide. This asymmetric system is obtained by coupling a selection layer with a conversion layer: the selection component is provided by a phononic crystal, while the conversion is achieved by a nonlinear self-demodulation effect in a 3D unconsolidated granular medium. A quantitative experimental study indicates asymmetric nature of this rectifier for wave-packet and extends the future applications of asymmetric systems.

1 Introduction

Over the past decade, the development of asymmetric systems operating on acoustic waves has proven to be a real challenge given the numerous applications both in optics and for radio-waves [1]. Research on unidirectional transmission devices for acoustic and elastic waves, i.e. permitting the wave energy to pass through in one direction but not the other, has led to applications, such as energy control, energy harvesting or accumulation, the transistor effect, logic gates and the memory effect for thermal devices [2],as well as to operations on signals and data, e.g. the optical device proposed in [3].

In this article, we are proposing the design and operations of an elastic wave rectifier based on the nonlinear self-demodulation effect. The rectifier is to operate with elastic waves in solids without requiring any external energy.

LUNAM Universite, Universite du Maine, CNRS, LAUM UMR 6613, avenue O. Messiaen, 72085 Le Mans, France, e-mail: thibaut.devaux@univ-lemans.fr

2 Architecture principle and experimental results

The schematic principle and a picture of the rectifier are shown in Fig. 1. The selection layer is a periodic medium, i.e. a phononic crystal (PC), composed of 9 alternating layers of aluminum and lucite. The conversion is performed by a strongly nonlinear granular medium (NLM) through a nonlinear self-demodulation effect.

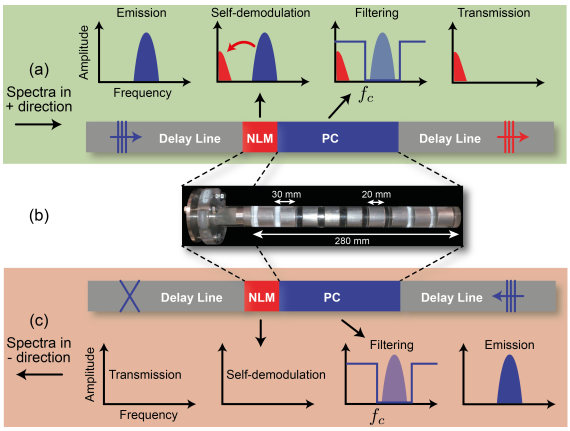

Fig. 1 (a) Schematics of the rectifier for the "+" direction; (b) Picture of the rectifier core, composed of a multilayer PC connected to a granular layer; and (c) Schematics for the "−" direction.

Let us specify the "−" direction for the case where the emitted wave, launched from the right side, first meets the PC, as shown in Fig. 1 (c). In this direction, an amplitude-modulated wave first excites the PC, which has been designed to exhibit a passband below a cutoff frequency of $f_c \simeq 35kHz$ and a band gap above. If the excitation signal frequencies exceed f_c, then: the PC does not transmit the signal, no acoustic energy is conveyed to the granular medium, and no signal passes through the system.

In contrast, in the "+" direction, see Fig. 1(a), the wave, launched from the left side, first excites the nonlinear granular medium, which converts part of the initial acoustic energy to lower frequencies through the self-demodulation effect.At the interface between the granular medium and the multilayer PC, the initial signal and the nonlinearly self-demodulated signal are both present. The PC then filters out frequencies above f_c while still transmitting the frequency components below f_c: the signal initially emitted is reflected, but the self-demodulated signal located in a passband is transmitted.

To operate this acoustic rectifier, a wave packet with a carrier frequency $f_0 = 45$ kHz and characteristic Gaussian envelope duration $t_g = 1/f_g = 0.1$ ms is excited in the emission delay line.

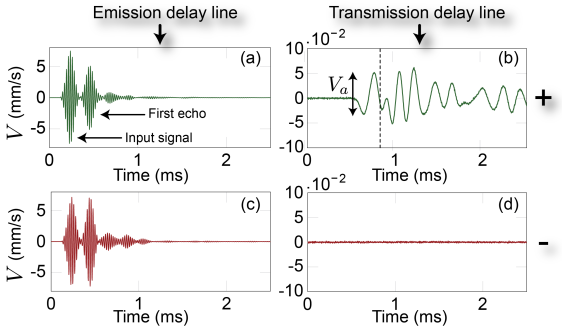

Fig. 2 Particle velocity V measured by the laser vibrometer in the middle of the delay lines. (a) and (b) "+" direction configuration. (c) and (d) "-" direction configuration.

In the "+" direction, i.e. Fig. 2(a,b), the excited wave packet first meets the nonlinear medium and is partially demodulated; its initial spectrum components are then reflected by the PC, Fig. 2(a). The self-demodulated part is transmitted through the PC and reaches the transmission delay line, as observed in Fig. 2(b). In the "-" direction, Fig. 2(c,d), the excited wave packet first meets the PC and is totally reflected (see the incident and reflected signals in Fig. 2(c)). In the transmission delay line, Fig. 2(d), no detectable signal is visible. The asymmetric nature of the rectifier has thus been demonstrated here in the time domain for pulsed signals.

3 Conclusion

In conclusion, a new asymmetric wave transmitter architecture has been proposed by utilizing physical conversion and selection mechanisms. The nonlinear self-demodulation effect induced by unconsolidated granular media has been introduced for the conversion process, while the selection procedure has been completed with a phononic crystal. Experimental results indicate asymmetric nature of the rectifier for pulsed signals.

Acknowledgements This work has been financed by "DGA" and the "PROPASYM" project funded by the Région Pays-de-la-Loire.

References

1. D. Jalas *et al*, Nat. Photonics **7**, 579 (2013).
2. B. Li *et al.*, Phys. Rev. Lett. **95**, 104302 (2005).
3. J. Hwang *et al.*, Nat. Mater. **4**, 383 (2005).
4. V. Tournat *et al.*, Phys. Rev. Lett. **92**, 085502 (2004).

Ultrasound propagation through Kelvin-Helmholtz instabilities

Nicolas MASSACRET, Joseph MOYSAN, Marie-Aude PLOIX, Jean-Philippe JEANNOT

Abstract In the frame of research on Sodium cooled Fast nuclear Reactor (SFR), CEA aims to develop an innovative instrumentation, specific to these reactors. The present work is related to the acoustic measurement in the liquid sodium near the outlet of the reactor's core assemblies. This instrumentation involves the propagation of ultrasonic waves in liquid sodium, thermally inhomogeneous and turbulent. Environment may cause deviations of the acoustic beam that must be understood to be predicted and quantified to consider ultrasound as a reliable measure means in a core of SFR reactor.

The works presented here are intended to observe the influence of a turbulent and thermally homogeneous fluid on the propagation of ultrasound for comparison with numerical computation. For this study, an experiment named IKHAR has been established. This experiment allows us to study the propagation of ultrasound through a flow of water containing Kelvin-Helmholtz instabilities.

These instabilities are a delicate hydraulic phenomenon to develop, but allows us to obtain an inhomogeneous and reproducible velocity field. Acoustic measurements, performed with phased array transducer, allow the observation of very thin time of flight variations on localized portions of the flow.

Nicolas MASSACRET
Aix-Marseille Université, LMA UPR 7051 CNRS, site LCND, 13625 Aix-en-Provence, France : massacret@lma.cnrs-mrs.fr
Joseph MOYSAN
Aix-Marseille Université, LMA UPR 7051 CNRS, site LCND, 13625 Aix-en-Provence, France : joseph.moysan@univ-amu.fr
Marie-Aude PLOIX
PROTISVALOR / LMA UPR 7051 CNRS, site LCND, 13625 Aix-en-Provence, France : marie-aude.ploix@univ-amu.fr
Jean-Philippe JEANNOT, CEA Cadarache, DEN/DTN/STCP/LIET, 13108 Saint-Paul-Lez-Durance, France : jean-phillipe.jeannot@cea.fr

1 Acoustic instrumentation in liquid sodium

Sodium-cooled fast reactors have been chosen by France as the reference option in the framework of the Generation IV international forum. For this kind of reactor, it is necessary to develop a specific instrumentation, compatible with sodium used as coolant, and to achieve the objectives of the Generation IV forum, particularly in terms of reliability.

In the reactor zone situated between the outlet of the fuel assemblies and the upper core structure, some of instrumental needs include thermometry and telemetry. Thermometry is used to determine the temperature of sodium at the assemblies' outlet. Telemetry is used to detect movements of these assemblies. Ultrasounds are well adapted to these measures because they propagate themselves rapidly in the liquid sodium, being weakly attenuated. Furthermore, these measurements can be performed far from the measurement area, without interaction between the ultrasonic transducer and the sodium flow.

However, in this area, the sodium flow is turbulent and present significant temperature variations. Depending on the orientation of the acoustic beam, these inhomogeneities may cause deviations and changes in the ultrasonic time of flight which could interfere with measurements.

Some numerical code, as AcRaliS [2] or CIVA [1], have been developed to compute the deviation and the delay of ultrasound propagation in such environments. Some experiments in static thermal inhomogeneous medium have been already done to verify a part of the model used in AcRaliS simulation code [3]. However in a turbulent medium, the chaotic nature of the flow makes complex the experimental verification of the model.

To deal with this issue, Kelvin-Helmholtz instabilities are a solution because this kind of instabilities, composed of eddies, are monitorable.

2 Kelvin-Helmholtz instabilities

Kelvin-Helmholtz instabilities are a kind of turbulence that develops in the mixing layer of two fluid flows moving in the same direction but at different speeds. The mixing layer is a very unstable area, and small perturbations in the flow are sufficient to cause the creation of eddies. These eddies are of small size at the beginning of the mixing layer, and then pairing themselves and grow gradually. Depending on fluid velocity and the observed area of the mixing layer, it is possible to generate varying intensities instabilities.

The disturbances that create these eddies can be intrinsic to the experimental design (geometry of the fluid pipe, random fluctuations in water speed), or periodically caused by the experimenter (creating pressures or flow speed controlled variations).

3 IKHAR experimental device

The experimental bench named IKHAR (Instabilities of Kelvin-Helmholtz for Acoustics Research) is a device that generates Kelvin-Helmholtz instabilities in water flows that can reach speeds of 3m.s^{-1}. On both sides of the test section pipe, are arranged two phased array probes of 64 elements that perform the time of flight and deviations measurements. This use of a pair of phased array allows us to acquire acoustic signals on very small surfaces, with a width inferior to the millimeter, and thus explore thin portions of the flow.
Then these results will be compared with numerical simulations where ultrasounds are propagated through a similar thermo-hydraulic medium. The thermo-hydraulic medium used for these calculations is also derived from numerical simulations (computational fluid dynamics simulations) run with Comsol.

4 First results

Even if the generation of instabilities created by IKHAR bench is not yet periodic, it is possible to measure the ultrasound time of flight variation through some well-formed eddies. These results show the evolution of flight time during the passage of one of these eddies. Evolutions are related to the size and vorticity of the eddy. The following figure show the result for one instability moving between the two transducer, and created with two flows of 0.4 m.s^{-1} and 2 m.s^{-1} composing the mixing layer.

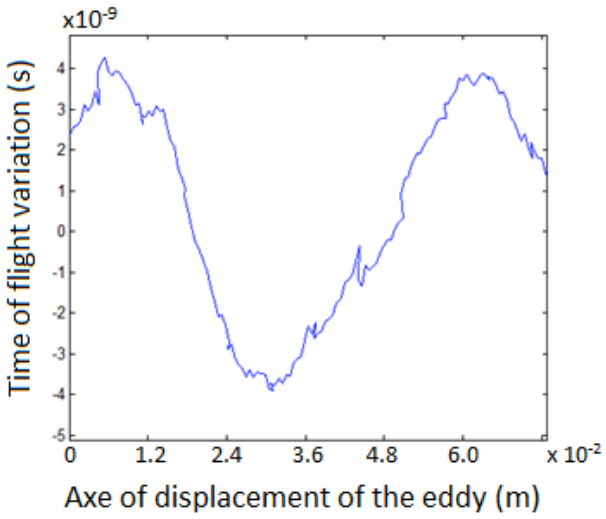

Figure 1. Acoustic time of flight variation for eddies moving between the two transducers at 1.2 m.s^{-1}.

Then computational fluid dynamics simulations have been realized with Comsol to generate a flow with instabilities of Kelvin-Helmholtz, and acoustics rays have been propagated through these thermo-hydraulics medium with AcRaLiS code.

These instabilities and one of the acoustics rays appear on the following figure.

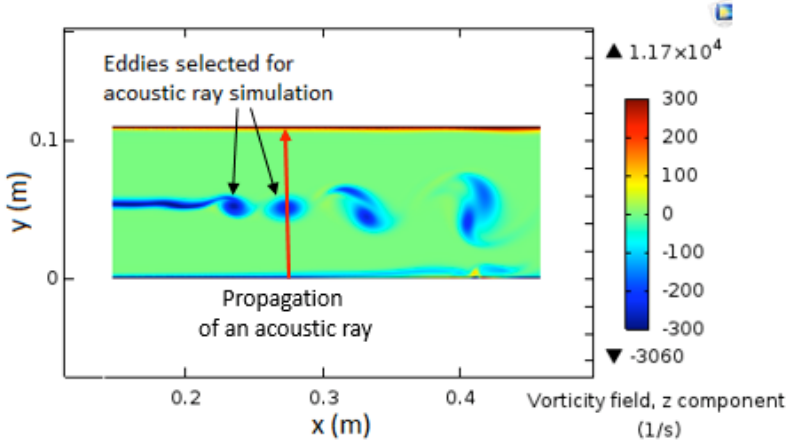

Figure 2. Computational Fluid Dynamic simulation of instabilities of Kelvin-Helmholtz (Run with Comsol).

The first results are encouraging, with time of flight variations of an order of 10 ns, as in the experiment. The following figure present the time of flight

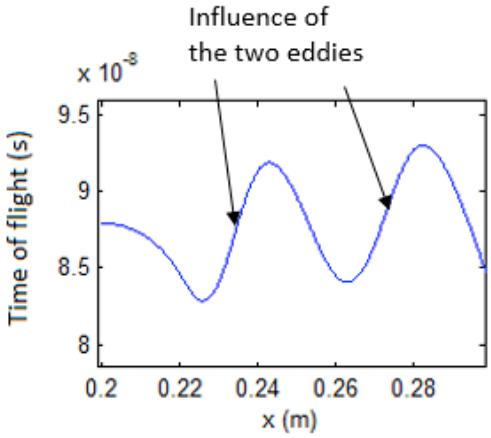

Figure 3. Simulation of the acoustic time of flight evolution through two instabilities (Run with AcRaLiS).

5 Conclusion

The use of phased array transducers allows us to measure small time of flight variations of ultrasounds through eddies, with a good spatial resolution thanks to the small width of each element. It is thus possible to characterize the size and the vorticity of each eddy. Moreover the first comparison with numerical simulations give us encouraging results.
The next step of this work is now to make periodic the generation of the Kelvin-Helmholtz eddies, introducing periodic disturbances in the flow or modifying some parts of the IKHAR geometry. This will improve the representativeness of CFD simulations and so improve the quality of the comparison between acoustic simulation and acoustic measurement.

References

1. Lu B., 'Modélisation de la propagation et de l'interaction d'une onde acoustique pour la télémétrie de structures complexes', PhD, Université du Maine, 2011.
2. Massacret N., 'Etude d'une méthode ultrasonore d'estimation des temperatures locales du sodium liquid en sortie coeur RNR-Na', PhD, Aix-Marseille Université, January 2014.
3. Massacret, N; Moysan, J; Ploix, MA; Jeannot, JP; Corneloup, G, 'Modelling of ultrasonic propagation in turbulent liquid sodium with temperature gradient', JOURNAL OF APPLIED PHYSICS, Volume: 115, Issue: 20, Article Number: 204905, DOI: 10.1063/1.4875876. May 2014.

2D and 3D Dispersion Loci of Guided Waves in Viscoelastic Composites of General Anisotropy

F. Hernando Quintanilla; Z. Fan; M.J.S. Lowe; R. V. Craster

Abstract Guided Waves are an important tool in many Non-destructive Evaluation (NDE) applications. The most realistic setting for many applications is achieved when one considers viscoelastic solids with material damping rather than their perfectly elastic idealizations.
In this conference, a Pseudospectral Collocation Method (PSCM) will be presented for tackling this more general family of problems involving viscoelastic materials. It will be shown that the PSCM also provides the full spectrum in three dimensions for elastic as well as viscoelastic problems.
Once the solution points using any method have been found, the challenge is to identify the modes to which they belong. Parity and Coupling properties of guided wave solutions will be discussed and how they can be used to identify with certainty the modes belonging to the point solutions.

1 Introduction

Non-destructive evaluation applications often use guided waves in order to inspect structures and the dispersion curves of these waves are crucial for understanding their physical properties and select the appropriate mode best suited to the goal of the investigation. The usage of dispersion curves for NDE is well established as the abundant literature and studies on the subject reflect, [1–10].

F. Hernando Quintanilla and M.J.S. Lowe
Department of Mechanical Engineering Imperial College, London SW7 2AZ, UK

Z. Fan
Aerospace Engineering, Nanyang Technological University, 50 Nanyang Avenue, Singapore 639798

R. V. Craster
Department of Mechanical Engineering Imperial College, London SW7 2AZ, UK

The majority of the references above assume the materials to be perfectly elastic but a more realistic approach to guided waves is to consider viscoelastic materials where attenuation due to material damping is present. Attenuation is accounted for by the imaginary part of the wavenumber and hence complex wavenumbers must be found when viscoelastic materials are considered.

2 Pseudospectral Collocation Method for Viscoelastic Materials and Companion Matrix

The main idea behind the PSCM is that one converts a set of Partial Differential Equations (PDEs) into a matrix eigenvalue problem. The solution to the PDE are the eigenvalues and eigenvectors. The reader is referred to the papers by Adamou *et al.* [9] and Hernando *et al.* [10] for a detailed account of this method and its implementation for elastic guided wave problems. After the appropriate manipulations, one can rewrite the equations of motion for elastic waves in anisotropic materials in the following form in order to make the wavenumber dependence explicit:

$$\left(\mathbf{Q}_2 k^2 + \mathbf{Q}_1 k + \mathbf{Q}_0(\omega^2)\right) \mathbf{U} = 0 \tag{1}$$

For viscoelastic materials, the modes for a given frequency are given by the complex wavenumber whose imaginary part accounts for the attenuation of the mode. However, as can be seen in Eq. (1), the equation is not linear in the wavenumber and hence one needs to linearize it in order to obtain a general eigenvalue form.
The linearization scheme chosen is known as the *Companion Matrix Method*, there are other options but this scheme has proved to be good for our purposes, see Bridges and Morris for further details [11]. After some manipulations one arrives at the following desired form for the problem in Eq. (1):

$$\mathbf{M}_1 \begin{pmatrix} \hat{\mathbf{U}} \\ \mathbf{U} \end{pmatrix} = k\, \mathbf{M}_2 \begin{pmatrix} \hat{\mathbf{U}} \\ \mathbf{U} \end{pmatrix} \tag{2}$$

where the wavenumber k now appears as the eigenvalue and the two matrices $\mathbf{M}_1$ and $\mathbf{M}_2$ are defined in terms of the $\mathbf{Q}_i$. This equation is readily solved for a given real frequency ω by any of the standard libraries available for eigenvalue problems. Further details can be found in Hernando *et al.* [12].
This is illustrated in the example below, figures 1 and 2 show the dispersion curves and attenuation respectively for a multilayer flat system composed of three Triclinic and Orthorhombic viscoelastic plates. Results given by the PSCM are shown in blue circles and the results obtained with a (Semi-Analytical Finite Element) SAFE [13] simulation are given in red asterisks. As can be seen, the agreement is excellent.
The reader is referred to the paper by Hernando *et al.* [12] for further details and examples.

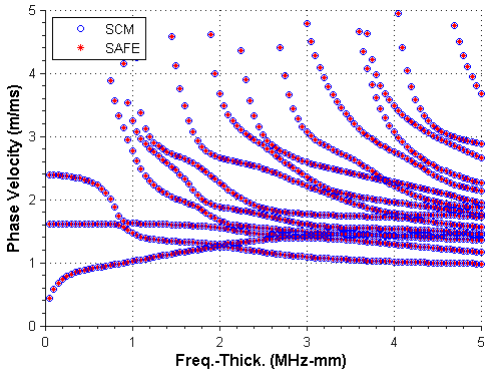

Fig. 1 Phase velocity for the 3-layered system with hysteretic-type damping: viscoelastic 8 mm thick triclinic layer (top), viscoelastic 5 mm thick orthorhombic layer (middle) and elastic 3 mm thick triclinic layer (bottom). Note that the total thickness has been used for the x axis in the figure. Solutions are plotted as follows: PSCM (blue circles) *vs.* SAFE (red asterisks).

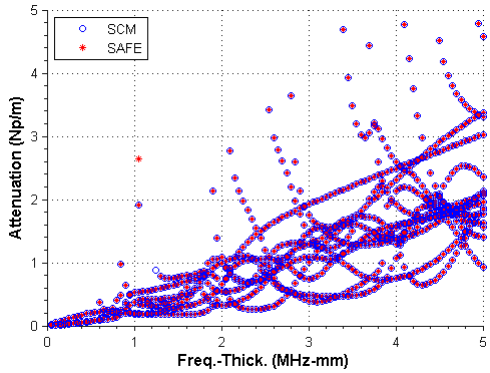

Fig. 2 Attenuation curves for the 3-layered system of Figure 1.

3 Dispersion Loci in 3D

The scheme just described provides much more information than the graphs just shown and by appropriately sorting the solution three-dimensional dispersion curves can be easily obtained for elastic as well as viscoelastic materials. Examples of this will be presented in the conference.

4 Parity and Coupling Properties of guided wave solutions

A discussion about the parity and coupling properties of guided wave solutions will be presented and how these can be exploited in order to avoid the problem of mode crossings and attain a robust approach to tracing dispersion curves. This will also be illustrated with several examples.

References

[1] R. D. Mindlin, Structural Mechanics. (Eds. J.N. Goodier and N. Hoff) 199–323 (1960).
[2] D. C. Gazis, J. Acoust. Soc. Am. **30**, 786–794 (1958).
[3] L. P. Solie and B. A. Auld, Journal of the Acoustical Society of America **54 (1)**, 50–65 (1973).
[4] A. H. Nayfeh and D. E. Chimenti, "Free wave propagation in plates of general anisotropic media," in *Review of Progress in Quantitative Non-destructive Evaluation*, edited by D. Thompson and D. Chimenti (Plenum Press, New York, 1989) p. 181.
[5] Y. Li and R. B. Thompson, Journal of the Acoustical Society of America **87 (5)**, 1911–1931 (1990).
[6] M. Lowe, IEEE Trans. Ultrason. Ferroelectr. Freq. Control **42**, 525–542 (1995).
[7] A. H. Nayfeh, Journal of the Acoustical Society of America **86 (5)**, 2007–2012 (1989).
[8] A. H. Nayfeh, Journal of the Acoustical Society of America **89 (4)**, 1521–1531 (1990).
[9] A. Adamou and R. Craster, Journal of the Acoustical Society of America **116 (3)**, 1524–1535 (2004).
[10] F. Hernando Quintanilla, M. Lowe, and R. Craster, Journal of the Acoustical Society of America **137 (3)**, 1180–1194 (2015).
[11] T. Bridges and P. Morris, Journal of Computational Physics **55**, 437–460 (1984).
[12] F. Hernando Quintanilla, Z. Fan, M. Lowe, and R. Craster, Proceedings of the Royal Society A **In press.** (2015).
[13] A. Marzani, E. Viola, I. Bartoli, F. Lanza di Scalea, and P. Rizzo, Journal of Sound and Vibration **318**, 488–505 (2008).

Guided Wave Vibration Techniques Applied to Hidden Tamper Detection

Robert Davey, David Abrahams, Raphael Assier and Rich Hewitt

Abstract We consider the use of guided waves in the testing of plates with delibrately hidden tampering. We briefly cover the use and applicability of thin plate theory in this context and discuss its limitation when modelling the tamper itself. We go on to study Rayleigh-Lamb waves and how they reflect at a boundary, discussing a variety of methods to solve this problem.

1 Introduction

We have been motivated by the problem of leaving important items with untrustworthy people. We wish to be sure that our important item has not been tampered with and in order to do this we wish to build a container which we can verify has not been accessed. Our work has been looking at the use of guided waves in order to perform this verification. This type of testing has been identified as possibly being useful in testing that the large areas of plates have not been breached and resealed.

2 Experimental Work

Some experimental work has been done on the use of guided waves in this area. The first work that was performed was simply exciting waves and seeing the response on a laser vibrometer. The laser vibrometer picks up the speed of the plate in the x,y,z directions seperately. This method proved very effective at detecting a tamper by eye due to mode conversion. Mode conversion is easy to detect as in-plane waves travel faster than out-of-plane waves. In fact when an out-of-plane mode is generated a

Robert Davey
University of Manchester, e-mail: robert.davey@postgrad.manchester.ac.uk

response in the out-of-plane direction is present where there should only be small vibrations from in-plane waves.

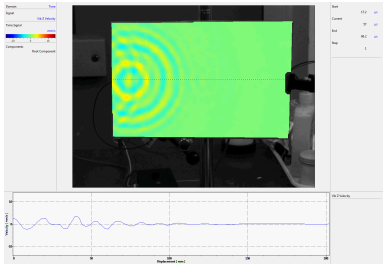

Fig. 1 A sample output from the laser virbrometer. This output shows the out-of-plane response soon after a wave has been excited in the plate. The in-plane response can be similarly isolated.

3 Kirchhoff Theory

We know that containers of interest are composed of thin metal plates, therefore we can use a thin plate theory to approximately describe their behaviour. We have studied the use of Kirchhoff theory in this context and found that the predictions in the bulk of the plate are accurate. However the mode conversion from in-plane to out-of-plane waves at tampered boundaries is not predicted.

We wish to find some appropriate boundary conditions for the Kirchhoff formulation. In order to do this we seek to solve the problem of Lamb waves scattering from a tamper boundary. We will then look at depth averaging this behaviour to find a sensible boundary condition in the Kirchhoff theory.

4 Reflection at the Boundaries

To solve the more complicated 3D elastic problem we will be looking at the reflection of Lamb waves. These are waves that exist in plates with zero stress on the top and bottom. There always exists a symmetric Lamb wave corresponding to longitudinal in-plane wave and an antisymmetric Lamb wave corresponding to out-of-plane wave. In the case of interest these will be the only propagating Lamb waves, although there will always exist infinitely many evanescent modes.

We wish to solve the problem of Lamb waves scattering from a boundary. We have started by looking at the configuration shown in figure 2 in the hope that this will aid us in more complicated examples. An important thing to note about this example is that we have a fully symmetric problem and hence we expect symmetric lamb waves to generate only a symmetric response, therefore we do not expect this example to provide us with mode conversion.

The non-depth-averaged problem of reflection of a Lamb wave is not trivial to solve. From Williams work [2] we know that the corners generate irregular terms that cause problems in simplistic mode matching methods. We have tried to solve this problem in two different ways in order to try and resolve these difficulties.

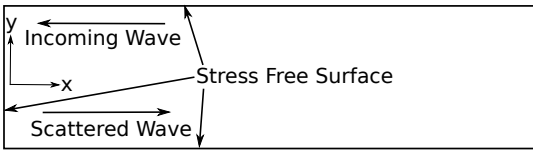

Fig. 2 The physical configuration of the problem we wish to solve. The main difficulty in this problem is the irregular form of the terms orginating from the corners as discussed in Williams [2].

We have looked at the method of projection to solve this problem, as described in Gregory and Gladwell [1]. This method attempts to deal with the irregular terms caused by the corner singularity from the outset and mode match only on the regular terms in order to improve convergence.

This method generates a series approximation of the displacements on the boundary as

$$\mathbf{U}^N \approx \mathbf{h} - \sum_{\substack{n=1 \\ n \neq a}}^{N} C_n \mathbf{S}_n^*, \tag{1}$$

defined up to a constant multiple. The choice of $\mathbf{h}$ is an attempt at dealing with the corner singularities but, as presented the paper does not take into account its full form as given by Williams [2]. Further to this a second series approximation is needed to find an expansion in terms of Lamb waves. These problems have resulted in poor convergence in the stress at the free boundaries, although useful information about the reflected modes can be gathered.

5 Further Work

We wish to use our understanding of this problem to find solutions to asymmetric setups. Once we have understood how the mode conversion happens, we wish to then depth average the important properties to give us boundary conditions in Kirchhoff theory.

References

1. RD Gregory and I Gladwell. The reflection of a symmetric rayleigh-lamb wave at the fixed or free edge of a plate. *Journal of Elasticity*, 13(2):185–206, 1983.
2. ML Williams. Stress singularities resulting from various boundary conditions. *Journal of Applied Mechanics*, 19(4):526–528, 1952.

Georgios Theocharis, CR2 CNRS Scientist, LAUM

Title:

Energy transport in one-dimensional disordered granular solids

Abstract:

Granular materials are collections of macroscopic grains that interact via dissipative and nonlinear forces. These materials are of substantial importance in many industrial and natural processes while at the same time they offer a perfect test bed for new insights into problems in condensed-matter physics and materials science. Despite their seeming simplicity, granular matter behaves quite differently from the other familiar forms of matter and their rich and complex dynamic behavior still present a major challenge in physics.

In this talk, I will present some recent results about the energy transport in one-dimensional disordered granular solids [1]. First, I will review some results about the existence and stability of nonlinear defect modes [2] in granular chains with one or two defects and how these modes can be used for the design of nonreciprocal acoustic devices [3]. Then, we will turn our attention to a sufficiently strong disordered granular chain. By increasing the initial excitation amplitudes I will show you that we are able to identify three distinct dynamical regimes with different energy transport properties: a near linear, a weakly nonlinear and a highly nonlinear regime. In the weakly nonlinear regime, we find that energy, initially trapped in a localized region, can be eventually detrapped and this has a direct influence on the fluctuations of the energy spreading. In the strongly nonlinear regime, we demonstrate that the energy is almost ballistically transported through shock-like excitations.

[1] V. Achilleos, G. Theocharis, and Ch. Skokos, arXiv:1509.03551
[2] Y. Man, N. Boechler, G. Theocharis, C. Daraio, Defect modes in one-dimensional granular crystals, Phys. Rev. E 85, 037601 (2012).
[3] N. Boechler, G. Theocharis, C. Daraio, Bifurcation-based acoustic switching and rectification, Nature Mat. 10665-8 (2011).

Periodic solutions with one sticking phase per period

Huong LE THI, Stephane JUNCA, Mathias LEGRAND

Abstract Periodic motions with sticking phase of a two degree-of-freedom vibro-impact spring mass model with perfect elastic impact and without source term are motivated and presented.

1 Equations and results

Periodic solutions with sticking phase have been observed in some continuous models of vibro-impact systems ([5]). To study this complex phenomenon, we consider a discrete n degree-of-freedom (dof) system. Since the sticking phase does not occur for a one dof system with perfect elastic impact and without source term, we consider the two dof vibro-impact system and find that it is the simplest model in which sticking phase occurs. In particular, we study the existence of periodic solutions with sticking phase of a model consisting of two springs and two masses:

$$\begin{cases} \mathbf{M}\ddot{\mathbf{u}} + \mathbf{K}\mathbf{u} = \begin{bmatrix} 0 \\ R(t) \end{bmatrix}, \\ \mathbf{u}(0) = \mathbf{u}_0, \quad \dot{\mathbf{u}}(0) = \dot{\mathbf{u}}_0, \\ u_2(t) \leq \mathbf{g}, \\ R(t) \leq 0, \quad (u_2(t) - \mathbf{g})\, R(t) = 0 \quad \forall t, \end{cases} \tag{1}$$

Huong LE THI
Laboratoire de Mathématiques J.A. Dieudonné and Team COFFEE INRIA, Université de Nice Sophia Antipolis Nice, France e-mail: lethih@unice.fr

Stéphane JUNCA
Laboratoire de Mathématiques J.A. Dieudonné and Team COFFEE INRIA, Université de Nice Sophia Antipolis Nice, France e-mail: junca@unice.fr

Mathias LEGRAND
Department of Mechanical Engineering McGill University
Montréal, Québec, Canada

where

$$\mathbf{M} = \begin{bmatrix} m_1 & 0 \\ 0 & m_2 \end{bmatrix}, \qquad \mathbf{K} = \begin{bmatrix} k_1 + k_2 & -k_2 \\ -k_2 & k_2 \end{bmatrix}, \qquad \mathbf{u}(t) = \begin{bmatrix} u_1(t) \\ u_2(t) \end{bmatrix},$$

$m_j, k_j, u_j, \dot{u}_j$ and $\ddot{u}_j$ represent the mass, stiffness, displacement, velocity and acceleration of the mass j, $j = 1,2$, respectively. The quantity $\mathbf{g}$ is the distance between the equilibrium position of mass 2 and the rigid wall. $R(t)$ is the reaction force of the wall on mass 2 at the time of impact.

A necessary condition for a sticking phase to occur is the existence of grazing contact ($\dot{u}_2^-(t) = 0$), i.e. impact with zero velocity. Moreover, sticking phase appears when the displacement of mass 1 reaches $\mathbf{g}$ with the positive velocity and it happens as long as the position of the mass 1 still greater than $\mathbf{g}$ ([4]). All the periodic motions with one sticking phase per period are computed. The key unknown parameter is the duration s of free flight phase which appears as a root of a nonlinear equation. When s is known (numerical computation), the period, the sticking time and the associated solution are explicitly derived. A number of numerical experiments of 1 spp solutions are also explored and a relationship between periodic solution with 1spp and periodic solution with 1 impact per period [6] is established.

References

1. Vincent ACARY, Bernard BROGLIATO: Numerical methods for nonsmooth dynamical systems. Applications in mechanics and electronics. it Lecture Notes in Applied and Computational Mechanics 35. Berlin: Springer. xxi, 525 p., 2008.
2. Patrick BALLARD: The Dynamics of Discrete Mechanical Systems with Perfect Unilateral Constraints, *Arch. Rational Mech. Anal.* 154 199274,2000.
3. Jrme BASTIEN, Frdric BERNARDIN, Claude-Henri LAMARQUE: Systmes dynamiques discrets non rguliers dterministes ou stochastiques, Applications aux modles avec frottement ou impact,*Collection Mcanique, Hermes Science Publications/Lavoisier, Paris,* 532 pp. (2012).
4. Sokly HENG: Nonlinear normal modes, private report with supervisors Stéphane JUNCA and Mathias LEGRAND, McGill University, November, 2013.
5. Denis LAXALDE, Mathias LEGRAND: Nonlinear modal analysis of mechanical systems with frictionless contact interfaces. *Comput. Mech.* 47, No. 4, 469-478, 2011.
6. Mathias LEGRAND, Stéphane JUNCA, Sokly HENG: Nonsmooth modal analysis of a N degree-of-freedom system with a purely elastic impact law, preprint, hal-01185980, 2015.
7. Madeleine PASCAL: Dynamics and stability of a 2 dof oscillator with an elastic stop, *Journal of Computational and Nonlinear Dynamics*, 2006.
8. Michelle SCHATZMAN: *A class of nonlinear differential equations of second order in time*, *Nonlinear Anal.* 2 , no. 3, 355373, 1978.
9. Anders THORIN, Mathias LEGRAND, Stéphane JUNCA: Nonsmooth modal analysis: investigation of a 2-dof spring-mass system subject to an elastic impact law, Proceedings of IDETC/CIE 2015, August 2-5, Boston, Massachusetts, USA, 2015.

Ultrasonic Particle Separation

Georgia Lynott and Dr Rich Hewitt (MSc Supervisor)

Abstract We seek to provide an introduction to the nonlinear acoustics governing the manipulation of objects using ultrasound. Acoustic streaming is briefly discussed, before focusing on the acoustic radiation pressure exerted on a free, rigid sphere in a plane wave. The results of King (1934) for the free sphere are recovered via an alternate approach, which is more easily extended to different geometries. The implications for acoustic levitation are briefly discussed.

1 Introduction

The use of ultrasonic waves to manipulate small particles and fluid droplets has garnered much interest in scientific circles, with potential applications, for example, in blood filtration (Petersson et al. (2004)) and contactless handling of samples (Ochiai et al. (2014)). Understanding the mathematics behind these phenomena, however, requires us to take account of the nonlinear effects of the ultrasonic field; the acoustic streaming in the fluid itself, and the acoustic radiation pressure on a particle in the field.

2 Acoustic Streaming

An ultrasonic transducer placed in a fluid will create a steady, non-zero mean flow in the fluid, a phenomenon known as acoustic streaming (or 'quartz wind'). Similar steady flows may arise due to the presence of an oscillating boundary, even in an inviscid or incompressible fluid - a full review is given by Riley (2001). Such flows are governed by the streaming Reynolds number, which we will illustrate briefly with an example studied by Secomb (1978).

Consider a fluid-filled channel of width $2a_0$ with oscillating walls, as shown in Fig. 1. We assume the walls of the channel undergo small sinusoidal perturbations of amplitude Δ, and angular frequency ω, so that $a(t) = a_0 + \Delta\cos(\omega t)$.

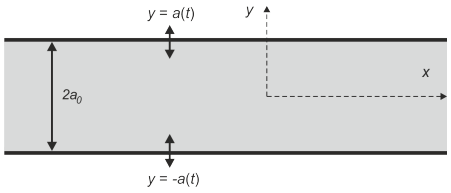

Fig. 1 Channel of half width a_0 with oscillating boundaries $y = \pm a(t)$.

School of Mathematics, The University of Manchester, Manchester M13 9PL, UK
e-mail: georgia.lynott@postgrad.manchester.ac.uk

Non-dimensionalisation of the Navier-Stokes equations gives rise to the Womersley constant $\alpha = a_0\sqrt{\omega/\nu}$, where ν is the kinematic viscosity of the fluid. This constant can be thought of as a measure for the unsteadiness in the system. We also define the ratio $\varepsilon = \Delta/a_0$, which then allows us to express the streaming Reynolds number as $R_s = \alpha^2\varepsilon^2$. As shown by Secomb, R_s is the ratio of the second order viscous term to the neglected fourth order convection term. To see the relation between the streaming Reynolds number R_s and the more usual Reynolds number, we note that

$$R_s = \varepsilon^2\alpha^2 = \frac{\Delta^2}{a_0^2}\cdot a_0^2\frac{\omega}{\nu} = \frac{\Delta\cdot(\Delta\omega)}{\nu},$$

so we have the familiar "$length \times speed/viscosity$" definition of the Reynolds number. For cases where $R_s < 1$, the streaming flow will be insignificant in size compared to the other forces at play. In the case of the applications mentioned in the introduction, a typical transducer has an amplitude of $\Delta \sim 1-10\,\mu$m, and a frequency less than 1 MHz, so we expect values of $R_s < 1$. For cases when $R_s > 1$, the acoustic streaming will play a non-negligible role in the motion of any particles in the field.

3 Acoustic Radiation Pressure

Expressions for the acoustic radiation force exerted on a rigid sphere by plane progressive and standing waves in a perfect fluid were first derived by King (1934). King's approach, which uses a moving origin embedded in the oscillating sphere, simplifies calculations in some respects, but causes difficulties when we wish to extend the problem to include, say, multiple spheres or a nearby boundary. We therefore attempt to recover the results of King via a more modern approach that fixes the origin, and is more amenable to such extensions.

Rigid free sphere in a plane wave

Consider a rigid, incompressible sphere of radius a and density ρ_s in a fluid of density ρ_0 insonified by a plane progressive wave of amplitude A and wavenumber k. Then the movement of sphere $\zeta(t)$ may be though of at first order as a displacement from some 'mean', i.e. leading order, location, by a small perturbation ε due to the oscillating first order pressure, so that

$$\zeta(t) = \varepsilon\zeta_1(t) + O(\varepsilon^2),$$

where the displacement at first order is of the form $\zeta_1 = De^{-i\omega t}$, where D is to be determined. The force on the sphere can then be expressed as:

$$\mathbf{F} = -\int_{S(t)}(\varepsilon p_1 + \varepsilon^2 p_2 + O(\varepsilon^3))\mathbf{n}\,\mathrm{d}S.$$

Considering the integral of the first order pressure p_1, we have at first order in ε the integral over the mean, stationary surface S_0. Since p_1 and the sphere both oscillate, the integral over the moving surface contributes, at second order in ε, a time inde-

pendent term $\mathbf{\Gamma}^{(0)}$ and a second harmonic term $\mathbf{\Gamma}^{(2)}$. The integral of the second order pressure p_2 over the mean surface also contributes to the second order steady terms. The force integral can then be expressed over the stationary surface, S_0, as

$$\mathbf{F} = -\varepsilon \int_{S_0} p_1 \mathbf{n}\, \mathrm{d}S - \varepsilon^2 \left(\mathbf{\Gamma}^{(0)} + \mathbf{\Gamma}^{(2)} e^{-2i\omega t} + \int_{S_0} p_2 \mathbf{n}\, \mathrm{d}S \right) + O(\varepsilon^3),$$

which after some rearranging reduces to the formula found in King for steady, second order force F_0^2, or acoustic radiation force

$$F_2^{(0)} = 2\pi\rho_0 A^2 \delta^6 \left(\frac{1 + \frac{2}{9}(1-P)^2}{(2+P)^2} \right),$$

where $\delta = ka$ is the usual ratio of wavelength to sphere radius and $P = \frac{\rho_0}{\rho_s}$ is the density ratio.

Free sphere in a standing wave

For a sphere at a distance h from the origin, i.e. the location of the source, the acoustic radiation force derived by King (p227, eq. 76) in the long wavelength limit $\delta \ll 1$ is

$$F_2^{(0)} = \pi\rho_0 A^2 \sin(2kh)\delta^3 \frac{\left(1 + \frac{2}{3}(1-P)\right)}{2+P}. \tag{1}$$

It is important to note that the force is much larger- $O(\delta^3)$- for a standing wave, than for a travelling of the same frequency and amplitude, where the force is only $O(\delta^6)$. We also note that the acceleration is *independent of radius of the sphere*, provided we remain in the limit $\delta = ka \ll 1$. The key parameter is the density ratio, $P = \frac{\rho_0}{\rho_s}$. If we consider acoustic levitation, where particles are suspended in a vertical standing wave between transducer and reflector, we can use (1) to find the maximum particle density which may be levitated and predict the location of the equilibrium points which the particles will move towards.

References

Louis V. King. On the acoustic radiation pressure on spheres. *Proceedings of the Royal Society of London A: Mathematical, Physical and Engineering Sciences*, 147(861):212–240, 1934.

Yoichi Ochiai, Takayuki Hoshi, and Jun Rekimoto. Three-dimensional mid-air acoustic manipulation by ultrasonic phased arrays. *PLoS ONE*, 9, 05 2014.

Filip Petersson, Andreas Nilsson, Cecilia Holm, Henrik Jonsson, and Thomas Laurell. Separation of lipids from blood utilizing ultrasonic standing waves in microfluidic channels. *Analyst*, 129:938–943, 2004.

N. Riley. Steady streaming. *Annu. Rev. Fluid Mech.*, 33:43–65, 2001.

T. W. Secomb. Flow in a channel with pulsating walls. *Journal of Fluid Mechanics*, 88:273–288, 9 1978.

Finite Element simulation of wave propagation in highly scattering materials.

Anton Van Pamel, Peter Huthwaite, Colin Brett, and Michael Lowe

Abstract Polycrystalline materials are challenging for ultrasonic Non-destructive Evaluation (NDE). Unlike acoustically transparent media, the microstructure of some metals which we wish to inspect is sufficiently coarse such that it causes scattering of the propagating waves. A consequent increase in attenuation and coherent noise both hinder flaw detection, making inspection difficult.

Until recently, the task of numerically modelling the wave scattering physics had been equally challenging. However, recent advances in computer technology and software have enabled step improvements, in particular the possibility of running realistically large Finite Element simulations[1-4]. The authors have adopted this approach to simulate elastic wave propagation in both 2D and 3D, for a typical polycrystalline material favoured by the power industry. The models use the Voronoi tesselations[5] representation to discretise granular material with defined statistics of grain size and orientations of the anisotropic stiffness properties within each grain. The implementation is on a GPU platform, using the POGO[6] time domain Finite Element code. The models have been used to predict scattering-induced attenuation, wave speed, and back-scatter noise[7, 8].

The presentation will show the implementation, validation and example uses of the model. The implementation includes an important focus on defining the spatial discretisation and achieving convergence. The validation includes comparison of the predictions of attenuation and wave speed by the 2D and 3D models with those of the Unified Theory[9] across a range of scattering regimes. Examples of use of the model have illustrated the difference between representations in three dimensions compared with those in two dimensions, and have provided useful insights into the ultrasonic array imaging of defects within these difficult materials.

Anton Van Pamel
Dept Mech Eng, Imperial College London, SW7 2AZ, UK, a.van-pamel11@imperial.ac.uk

Peter Huthwaite
Dept Mech Eng, Imperial College London, SW7 2AZ, UK, p.huthwaite@imperial.ac.uk

Colin Brett
E.ON Technologies (Ratcliffe) Ltd, Nottingham, UK, Colin.Brett@eon.com

Michael Lowe
Dept Mech Eng, Imperial College London, SW7 2AZ, UK, m.lowe@imperial.ac.uk

References

1. G. Ghoshal and J. A. Turner, "Numerical model of longitudinal wave scattering in polycrystals, IEEE Trans. Ultrason. Ferroelectr. Freq, Control, 648, pp1419-1428, 2009.
2. B. Chassignole, V. Duwig, M.-A. Ploix, P. Guy and R. El Geurjouma, "Modelling the attenuation in the ATHENA finite elements code for the ultrasonic testing of austenitic stainless steel welds, Ultrasonics, 49, pp653-658, 2009.
3. S. Shahjahan, F. Rupin, A. Aubry, B. Chassignole, T. Fouquet and A. Derode, "Comparison between experimental and 2-D numerical studies of multiple scattering in Inconel 600 by means of array probes", Ultrasonics, 54, pp358-367, 2014.
4. B. Lan, M. J. S. Lowe and F. P. E. Dunne, "Experimental and computational studies of ultrasonic wave propagation in hexagonal close-packed polycrystals for texture detection", Acta Mater., 63, pp107-122, 2014.
5. F. Aurenhammer, "Voronoi diagrams - a survey of a fundamental geometric data structure", ACM Comput. Surv., 23, pp 345-405, 1991.
6. P. Huthwaite, "Accelerated Finite Element elastodynamic simulations using the GPU", J. Comput. Phys., 257, pp687-707, 2014.
7. A. Van Pamel, P. Huthwaite, C. R. Brett and M. J. S. Lowe, "Finite Element modelling of elastic wave scattering in a polycrystalline material in 2D and 3D, J. Acoust. Soc. Am., in press, 2015.
8. A. Van Pamel, P. Huthwaite, C. R. Brett and M. J. S. Lowe, "Finite Element Modelling of Wave Propagation in Highly Scattering Materials", Review of Progress in Quantitative NDE, eds. D.E. Chimenti and L.J. Bond, AIP Conference series, in press, 2016.
9. F. E. Stanke and G. S. Kino, "A unified theory for elastic wave propagation in polycrystalline materials", J. Acoust. Soc. Am., 75, pp 665–681, 1984.

LIST OF ATTENDEES

Liste of Attendees

Al-Lashi Raied S.	R.Al-lashi@leeds.ac.uk
Barnwell Ellis	ellis.barnwell@gmail.com
Baronian Vahan	vahanbaronian@cea.fr
Bellis Cédric	bellis@lma.cnrs-mrs.fr
Berjamin Harold	berjamin@lma.cnrs-mrs.fr
Bonnet-Ben Dhia Anne-Sophie	anne-sophie.bonnet-bendhia@ensta.fr
Bourgeois Laurent	laurent.bourgeois@ensta.fr
Calmon Pierre	pierre.calmon@cea.fr
Castaings Michel	m.castaings@i2m.u-bordeaux1.fr
Chabassier Juliette	juliette.chabassier@inria.fr
Chapman John	c.j.chapman@keele.ac.uk
Chouiyakh Hajar	hajar.chouiyakh@gmail.com
Clark Matt	matt.clark@nottingham.ac.uk
Colombi Andrea	andree.colombi@gmail.com
Colquitt Daniel	d.colquitt@imperial.ac.uk
Darmon Michel	michel.darmon@cea.fr
Davey Robert	robert.davey@postgrad.manchester.ac.uk
Deschamps Marc	m.deschamps@i2m.u-bordeaux1.fr
Desoudin Béatrice	b.desoudin@i2m.u-bordeaux1.fr
Desoudin Philippe	b.desoudin@free.fr
Destuynder Philippe	philippe.destuynder@cnam.fr
Devaux Thibaut	thibaut.devaux@univ-lemans.fr
Er-Raoudi Mina	erraoudi.mina@gmail.com
Gallezot Matthieu	matthieu.gallezot@ifsttar.fr
Hafidi Alaoui Hamza	hamzaalaouihafidi@gmail.com
Haslinger Stewart	Stewart.Haslinger@liverpool.ac.uk
Hernando Quintanilla Francisco	francisco.hernando-quintanilla11@imperial.ac.uk
Joyce Duncan	duncan.joyce@postgrad.manchester.ac.uk
Junca Stéphane	junca@unice.fr
Kergomard Jean	kergomard@lma.cnrs-mrs.fr
Lan Bo	BO.LAN@IMPERIAL.AC.UK
Le Thi Huong	lethih@unice.fr

Leger Alain	leger@lma.cnrs-mrs.fr
Lombard Bruno	lombard@lma.cnrs-mrs.fr
Lopez Villaverde Eduardo	eduardo.lopezvillaverde@cea.fr
Lowe Mike	m.lowe@imperial.ac.uk
Lynott Georgia	georgia.lynott@postgrad.manchester.ac.uk
Massacret Nicolas	massacret@lma.cnrs-mrs.fr
Mercier Jean-François	jean-francois.mercier@ensta.fr
Mulholland Anthony	Anthony.mulholland@strath.ac.uk
Pagneux Vincent	vincent.pagneux@univ-lemans.fr
Recoquillay Arnaud	arnaud.recoquillay@ensta-paristech.fr
Rodat Damien	damien.rodat@airbus.com
Rowley William	william.rowley-3@postgrad.manchester.ac.uk
Saidoun Abdelkrim	abdelkrim.saidoun@u-bordeaux.fr
Serey Valentin	valentin.serey@u-bordeaux.fr
Shi Fan	f.shi12@imperial.ac.uk
Siryabe Emmanuel	emmanuel.siryabe@u-bordeaux.fr
Tant Katherine	katy.tant@strath.ac.uk
Theocharis Georgios	georgiostheocharis@gmail.com
Treyssède Fabien	fabien.treyssede@ifsttar.fr
Van Pamel Anton	a.van-pamel11@imperial.ac.uk

Commissariat à l'Energie Atomique

Centre National de la Recherche Scientifique

UK Research Centre in NonDestructive Evaluation

Institut Français des Sciences et Technologies des Transports, de l'Aménagement et des Réseaux